UCLA
UCLA Electronic Theses and Dissertations

Title

The Effects of Neoadjuvant anti-Programmed Cell Death Protein 1 (PD-1) Therapy on the Tumor Infiltrating T cell compartment and Tumor Microenvironment Immune Composition in Recurrent Glioblastoma Patients

Permalink

https://escholarship.org/uc/item/3fw26397

Author

Lee, Alexander Hao

Publication Date

2023

Peer reviewed|Thesis/dissertation

eScholarship.org Powered by the California Digital Library
University of California

UNIVERSITY OF CALIFORNIA

Los Angeles

The Effects of Neoadjuvant anti-Programmed Cell Death Protein 1 (PD-1) Therapy on the Tumor Infiltrating T cell compartment and Tumor Microenvironment Immune Composition in Recurrent Glioblastoma Patients

A dissertation submitted in partial satisfaction of the

requirements for the degree Doctor of Philosophy

in Molecular and Medical Pharmacology

by

Alexander Hao Lee

2023

© Copyright by

Alexander Hao Lee

2023

ABSTRACT OF THE DISSERTATION

The Effects of Neoadjuvant anti-Programmed Cell Death Protein 1 (PD-1) Therapy on the Tumor Infiltrating T cell compartment and Tumor Microenvironment Immune Composition in Recurrent Glioblastoma Patients

by

Alexander Hao Lee

Doctor of Philosophy in Molecular and Medical Pharmacology

University of California, Los Angeles, 2023

Professor Robert M. Prins, Chair

Glioblastoma (GBM) is the most common malignant tumor in the central nervous system and has poor patient survival rates. Unlike other cancers, immune checkpoint therapies, such as PD-1 checkpoint blockade, have been largely ineffective in GBMs for several reasons: an immunosuppressive tumor microenvironment, a lack of suitable neoantigens, and poor intratumoral T cell infiltration and activity. However, there is evidence that using anti-PD-1 therapy in the neoadjuvant setting may generate a more robust anti-tumor immune response, though characterizing how the GBM tumor microenvironment changes with such therapy is incomplete. As such, we performed high dimensional analysis using CyTOF mass cytometry and single-cell RNAsequencing to study the intratumoral immune populations in GBM patients treated with or without neoadjuvant anti-PD-1 therapy. Characterizing PD-1 expressing tumor infiltrating T cell populations showed that PD-1 was associated with markers of T cell activation and dysfunction regardless of treatment and that this association existed less strongly in peripheral PD-1 expressing T cells. We studied the effects of neoadjuvant anti-PD-1 therapy on

a large patient cohort of tumor infiltrating immune cells and found that neoadjuvant anti-PD-1 therapy significantly increased the proportion of several intratumoral T cell sub-populations, including a *TCF7*-expressing progenitor exhausted population. Downstream effects of neoadjuvant anti-PD-1 therapy on T cells, namely increased production of IFN-γ, included transcriptionally altering the myeloid and dendritic cell populations to be more immune suppressive but also potentially more vulnerable to other immune checkpoint therapies, specifically anti-TIGIT and anti-CTLA-4 therapies. Due to the impact of neoadjuvant anti-PD-1 therapy on intratumoral T cell populations, we examined whether we could detect tumor-reactive T cells by cloning TCRs from transcriptionally defined populations in a patient treated with neoadjuvant anti-PD-1 and testing reactivity to the patient-derived gliomasphereline. Among TCRs cloned, we discovered that T cells arising from the activated and exhausted population showed tumor reactivity, suggesting that utilizing transcriptional phenotypes can guide selection of potential tumor-reactive TCRs in GBM patients treated with neoadjuvant anti-PD-1 therapy. In conclusion, neoadjuvant anti-PD-1 therapies alters the immune landscape in these tumors and can be potentially used in combination with other immunotherapies to more effectively treat this malignancy.

The dissertation of Alexander Hao Lee is approved.

David A. Nathanson

Anna Wu Work

Yi Xing

Robert M. Prins, Committee Chair

University of California, Los Angeles

2023

DEDICATION

This work is dedicated to the following:

To my mom and dad whose love and hard work to provide for me growing up often went unnoticed and underappreciated yet has undeniably paved the way to every accomplishment that I have ever achieved.

To my wife Christine whose support and love for me never wavered during the challenges of life and school and who daily fills my life with laughter and joy.

Finally, to God to whom I owe my existence, love, and worship and to my church family at Gracepoint Church that God graciously allowed me to be a part of. I resonate with the words of C.S. Lewis who once wrote, “I believe in Christianity as I believe that the sun has risen: not only because I see it, but because by it I see everything else.”

TABLE OF CONTENTS

Abstract of Dissertation ……. ii - iii

Committee Page ……. iv

Dedication ……. v

Table of Contents ……... vi - ix

Acknowledgments …….. x - xii

Vita ……... xiii - xiv

INTRODUCTION ……..... 1 - 2

CHAPTER 1: Expression of PD-1 by T cells in malignant glioma patients reflects exhaustion and activation ……. 3 - 29

Figure 1: CD3+ T cells from malignant glioma patients demonstrate significantly elevated expression of PD-1 compared to healthy donor PBMCs and glioma patient PBMCs ……. 7

Table 1: Patient Characteristics …….....8

Figure 2: High dimensional analysis of mass cytometry data shows elevated expression of markers of activation and exhaustion on CD3+ PD-1+ TILs and markers of activation and antigen experience on CD3+ PD-1+ PBMCs from malignant glioma patients ……11 - 12

Figure 3: PD-1+ T cells have decreased TCR diversity compared to PD-1- cells …….. 14

Figure 4: CD3+ PD-1+ T cells from pooled glioma patient PBMCs produce higher levels of IFN-γ compared to the CD3+ PD-1- T cell population after T cell activation ……. 16

Figure 5: A schematic indicating what PD-1 expression means in the context of malignant glioma …… 17

Supp. Figure 1: T cells from GBM patient TILs show highest expression of PD-1 compared to healthy donor PBMC and GBM patient PBMCs …… 26

Supp. Figure 2: Additional CyTOF data …… 27

Supp. Figure 3: Gene expression analysis show increased transcription of activation and exhaustion genes in the PD-1+ population in glioma TILs and of antigen experienced genes in the PD-1+ population in glioma PBMCs …….. 28

Supp Table 1: Antibodies used in Mass Cytometry Analysis …… 29

CHAPTER 2 - Neoadjuvant PD-1 blockade induces T cell and cDC1 activation but fails to overcome the immunosuppressive tumor associated macrophages in recurrent glioblastoma ……... 30 - 85

Figure 1: Neo-aPD1 increases the proportion and number of CD3+ T cells among tumor infiltrating immune cells in recurrent glioblastoma patients ……... 36-37

Figure 2: Single-cell RNAseq analysis of intratumoral T cells shows transcriptional changes with neo-aPD1 therapy …….. 41 -42

Figure 3: The phenotype and clonal distribution of intratumoral vs. peripheral T cells in recurrent glioblastoma patients …….. 45 - 46

Figure 4: Neo-aPD1 induces multiple immunosuppressive TAMs and monocyte populations …… 50 - 51

Figure 5: Neo-aPD1 therapy increases the proportion of intratumoral migratory DCs …….. 54 - 55

Figure 6: Increased engagement of additional immune checkpoints may limit neoadjuvant anti-PD1-driven T cell activation …….. 59 - 60

Suppl. Figure 1: Clustering of GBM-derived CD45+ cells based on the CyTOF and single cell RNAseq profiles …….. 72 - 73

Suppl. Figure 2: Identification of different lymphoid subpopulations from scRNAseq ……... 74 - 75

Suppl. Figure 3: Expression of various marker genes across the different immune subsets in the PBMC ……. 76

Suppl. Figure 4: CyTOF based clustering of the myeloid cells …….. 78 - 79

Suppl. Figure 5: Differential gene expressions in the monocytic myeloid populations ……. 80

Suppl. Figure 6: scRNAseq analysis of the DC cluster from the myeloid subclustering analysis …….. 81 - 86

Suppl. Figure 7: Significantly enriched receptor ligand interactions after neoadjuvant anti-PD1 ……... 83 - 84

Suppl. Figure 8: A schematic proposing how neoadjuvant anti-PD1 changes the immune landscape in the GBM tumor mircroenvironment …….. 85

CHAPTER 3 - Identification and Isolation of tumor-reactive TCR clonotypes based on in silico single-cell transcriptomic and TCR profiling in recurrent glioblastoma patients treated with neoadjuvant anti-PD-1 therapy …….. 86 - 117

Figure 1: Single-cell RNA and TCRseq show T cell expansion, enrichment, and potential tumor-reactivity in the late activated and exhausted T cell cluster ……..90 - 91

Figure 2: Identification of Tumor-reactive TCRs in a recurrent GBM patient treated with EGFRvIII Bispecific Antibody and neoadjuvant anti-PD-1 therapy using a triple-reported Jurkat line transduced with a TCR library primarily consisting of TCRs from the late activated / exhausted T cell population …..……. 96 - 97

Figure 3: Schematic of a workflow for how tumor antigen specific TCRs may be detected using single-cell RNAseq and TCRseq in recurrent GBM patients treated with neoadjuvant anti-PD-1 therapy ……..... 100

Suppl. Figure 1: Single-cell Gene Expression analysis on all tumor infiltrating CD45+ cells in the cohort of 32 recurrent glioblastoma patients …….....109

Suppl. Figure 2: Single-cell RNAseq on CD3+ lymphoid cells ……..……110 - 111

Suppl. Figure 3: Characteristics of a recurrent glioblastoma patient (LB3914) treated with EGFRvIII Bispecific T cell Engager (BiTE) and neoadjuvant anti-PD-1 therapies …...……112 - 113

Suppl. Figure 4: The overlap of detected TCRs from tumor infiltrating T cells using scTCRseq and detected peripheral TCRs from PBMC collected at various time points using Adaptive Technologies ImmunoSeq platform ……. 114 - 115

Suppl. Figure 5: ProgExh-TCR library primarily consisting of TCRs detected in the progenitor exhausted T cell clusters ……116 - 117

CONCLUSION …… 118 - 120

Bibliography ……... 121 - 137

ACKNOWLDEGEMENTS

Chapter 1: Expression of PD-1 by T cells in malignant glioma patients reflects exhaustion and activation

Chapter 1 is a reprint of: *Tom B. Davidson, Alexander Lee, Melody Hsu, Shaina Sedighim, Joey Orpilla, Janet Treger, Max Mastall, Saskia Roesch, Carmen Rapp, Mildred Galvez, Aaron Mochizuki, Joseph Antonios, Alejandro Garcia, Nikesh Kotecha, Nicholas Bayless, David Nathanson, Anthony Wang, Richard Everson, William H. Yong, Timothy F. Cloughesy, Linda M. Liau, Christel Herold-Mende, and Robert M. Prins. (2019). "Expression of PD-1 by T Cells in Malignant Glioma Patients Reflects Exhaustion and Activation."* Clin Cancer Res ***25****(6): 1913-1922 DOI: 10.1158/1078-0432.CCR-18-1176*

Dr. Tom B. Davidson, Dr. Christel Herold-Mende, and Dr. Robert M. Prins designed the study. Alexander Lee, Dr. Melody Hsu, Joey Orpilla, Dr. Janet Treger, Max Mastall, Saskia Roesch, Carmen Rapp, Mildred Galvez, and Shaina Sedighim conducted experiments. Dr. Tom B. Davidson, Alexander Lee, Dr. Aaron Mochizuki, Dr. Joe Antonios, Dr. Richard Everson, Joey Orpilla, and Shaina Sedighim analyzed the data. Dr. Alejandro Garcia, Dr. William Yong, Nikesh Kotecha, Nicholas Bayless, Dr. David Nathanson, and Dr. Timothy Cloughesy contributed technical and scientific advice. Dr. William Yong, Dr. Anthony Wang, Dr. Richard Everson, and Dr. Linda Liau provided patients' samples.

This project was supported by the UCLA Tumor Immunology Training Grant (USHHS Ruth L. Kirschstein Institutional National Research Service Award # T32 CA009120)

Permission for reprint was granted by the American Association for Cancer Research

Chapter 2: Neoadjuvant PD-1 blockade induces T cell and cDC1 activation but fails to overcome the immunosuppressive tumor associated macrophages in recurrent glioblastoma

Chapter 2 is a reprint of: *Alexander H. Lee, Lu Sun, Aaron Y. Mochizuki, Jeremy G. Reynoso, Joey Orpilla, Frances Chow, Jenny C. Kienzler, Richard G. Everson, David Nathanson, Steven Bensinger, Linda M. Liau, Timothy Cloughesy, Willy Hugo, and Robert M. Prins. (2021). "Neoadjuvant PD-1 blockade induces T cell and cDC1 activation but fails to overcome the immunosuppressive tumor associated macrophages in recurrent glioblastoma." Nat Communications* ***12****(1): 6938. DOI: 10.1038/s41467-021-26940-2*

Dr. Robert M. Prins, Alexander Lee, Dr. Lu Sun, Dr. Aaron Y. Mochizuki, Jeremy Reynoso, and Dr. Willy Hugo designed experiments. Alexander Lee, Dr. Lu Sun, Dr. Aaron Y. Mochizuki, Joey Orpilla, Dr. Frances Chow, and Jeremy Reynoso performed the experiments unless specified. Alexander Lee, Dr. Lu Sun, Dr. Aaron Y. Mochizuki, Dr. Jenny Kienzler, and Dr. Willy Hugo participated in the processing and analysis of CyTOF and scRNAseq data. Dr. Robert M. Prins, Dr. Frances Chow, Dr. Aaron Y. Mochizuki, Alexander Lee, Dr. Lu Sun, Dr. Willy Hugo, Dr. Steven Bensinger, Dr. David Nathanson, Dr. Timothy Cloughesy, Dr. Richard Everson. and Dr. Linda Liau participated in the design, preparation, and analysis of experiments and acquired and analyzed data related to human samples.

This project was supported by the UCLA Tumor Immunology Training Grant (USHHS Ruth L. Kirschstein Institutional National Research Service Award # T32 CA009120)

Permission for reprint was granted by the Nature Publishing Group

Chapter 3: Identification and Isolation of tumor-reactive TCR clonotypes based on in silico single-cell transcriptomic and TCR profiling in patients with recurrent glioblastoma

Chapter 3 is a version of a manuscript being prepared for publication: *Alexander H. Lee, Lu Sun, Frances Chow, Janet Treger, Danielle Cook, Ely Porter, Xi Chen, Gilbert Herrera, Richard G. Everson, Linda M. Liau, Timothy Cloughesy, Willy Hugo, David Nathanson, and Robert M. Prins. "Identification and Isolation of tumor-reactive TCR clonotypes based on in silico single-cell transcriptomic and TCR profiling in patients with recurrent glioblastoma."*
Dr. Robert Prins, Alexander Lee, Lu Sun, Dr. Frances Chow, Danielle Cook, Ely Porter, and Xi Chen designed the experiments. Alexander Lee and Janet Treger performed the experiments. Alexander Lee, Lu Sun, and Gilbert Herrera participated in the processing and analysis of the single-cell sequencing data. Dr. Robert M. Prins, Dr. Frances Chow, Alexander Lee, Lu Sun, Willy Hugo, David Nathanson, Dr. Timothy Cloughesy, Dr. Richard Everson. and Dr. Linda Liau participated in the design, preparation, and analysis of experiments and acquired and analyzed data related to human samples.

VITA

EDUCATION

University of California, Los Angeles **Mar 2023**
PhD Candidate, Molecular and Medical Pharmacology
Faculty Mentor: Robert M. Prins, PhD

University of California, Berkeley **2011**
Bachelor of Arts, Molecular and Cell Biology

RESEARCH EXPERIENCE

University of California, Los Angeles
Dept. of Molecular and Medical Pharmacology
PhD Candidate working in Dr. Robert Prins' Laboratory **August 2015 - Present**

Stanford University – School of Medicine
Research Assistant for Dr. Jean Tang **June 2011 – July 2015**

PUBLICATIONS

(ORCHID ID: 0000-0002-4583-0740)

1. **Lee, A.***, Sun, L.*, et al. (2021). "Neoadjuvant PD-1 blockade induces T cell and cDC1 activation but fails to overcome the immunosuppressive tumor associated macrophages in recurrent glioblastoma." *Nat Commun* 12(1): 6938.

2. Davidson, T.*, **Lee, A.***, et al. (2019). "Expression of PD-1 by T Cells in Malignant Glioma Patients Reflects Exhaustion and Activation." *Clin Cancer Res* 25(6): 1913-1922.

3. Cloughesy, T., Mochizuki A., Orpilla J., Hugo W, **Lee A.**, et al. (2019). "Neoadjuvant anti-PD-1 immunotherapy promotes a survival benefit with intratumoral and systemic immune responses in recurrent glioblastoma." *Nat Med* 25(3): 477-486.

4. Whitson, R., **Lee A.**, et al. (2018). "Noncanonical hedgehog pathway activation through SRF-MKL1 promotes drug resistance in basal cell carcinomas." *Nat Med* 24(3): 271-281.

5. Mirza, A., Fry M., Urman N., Atwood S., Roffey J, Ott G., Chen B., **Lee A.**, et al. (2017). "Combined inhibition of atypical PKC and histone deacetylase 1 is cooperative in basal cell carcinoma treatment." *JCI Insight* 2(21).

6. Chen, B., Trang, V., **Lee, A.,** et al. (2016). "Posaconazole, a Second-Generation Triazole Antifungal Drug, Inhibits the Hedgehog Signaling Pathway and Progression of Basal Cell Carcinoma." *Mol Cancer Ther* 15(5): 866-876.

7. Ra, H., Gonzalez-Gonzalez, E., Uddin, J., King, B., **Lee, A.**, et al. (2015). "Detection of non-melanoma skin cancer by in vivo fluorescence imaging with fluorocoxib A." *Neoplasia* 17(2): 201-207.

8. Tang, Y., Gholamin, S., Willardson, M., **Lee, A**., et al. (2014). "Epigenetic targeting of Hedgehog pathway transcriptional output through BET bromodomain inhibition." *Nat Med* 20(7): 732-740.

9. Kim, J., Aftab, B., Tang, J., Kim, D., **Lee, A.**, et al. (2013). "Itraconazole and arsenic trioxide inhibit Hedgehog pathway activation and tumor growth associated with acquired resistance to smoothened antagonists." *Cancer Cell* 23(1): 23-34.

10. Atwood, S. X., Li, M., **Lee, A.**, et al. (2013). "GLI activation by atypical protein kinase C iota/lambda regulates the growth of basal cell carcinomas." *Nature* 494(7438): 484-488.

CONFERENECE PRESENTATIONS

1. **Lee, A.**, et al. (2021). “Neoadjuvant PD-1 blockade induces T cell and cDC1 activation but fails to overcome the immunosuppressive tumor associated macrophages in recurrent glioblastoma.” Oral Presentation at Society of Neuro-Oncology Annual Meeting 2021, Boston, MA.

2. **Lee, A.**, et al. (2020). “Single-cell RNAseq of tumor infiltrating immune cells in glioblastoma patients treated with neoadjuvant anti-PD1 therapy reveals global changes and immunosuppressive adaptive responses by the myelo-monocytic populations.” Oral Presentation at Society of Neuro-Oncology Annual Meeting 2020, Virtual Meeting

3. **Lee, A.**, et al. (2019). “Neoantigens arising from alternative splicing events may be targeted by tumor infiltrating lymphocytes in glioblastomas.” Oral Presentation at Society of Neuro-Oncology Annual Meeting 2019, Phoenix, AZ.

4. **Lee, A.**, et al. (2018). “Multidimensional characterization of immune cell populations in the glioma tumor microenviroment reveals a dominant proportion of cells derived from the myelo-monocytic lineage.” Oral Presentation at Society of Neuro-Oncology Annual Meeting 2018, New Orleans, LA

5. **Lee, A.**, et al. (2018). “The immune landscape of PD-1 expression in human glioblastoma characterization of PD-1.” Oral Presentation at AACR: Immunobiology of Primary and Metastatic CNS Cancer: Multidisciplinary Science to Advance Cancer Immunotherapy 2018, San Diego, CA

6. **Lee, A.**, et al. (2017). “Immune Landscape of PD-1/PD-L1 in Brain Tumor Immune Cell Population using CyTOF Mass Cytometry.” Oral Presentation at Society of Neuro-Oncology 2017, San Francisco, CA

AWARDS

T32 UCLA Tumor Immunology Training Grant
2018-2021
National Institutes of Health

Isabel & Harvey Kibel Fellowship
2017-2018
UCLA’s Graduate Programs in Biosciences

INTRODUCTION:

Glioblastomas (GBM) are the most common primary cancer found in the central nervous system (CNS) with a five year survival rate of less than 5% and with a high recurrence rate, due in part to its resistance to developed therapies, chemotherapy, and radiation[1]. Factors that contribute to this resistance include: the blood-brain barrier that limits drug entry, the stem-like properties of glioblastoma, and the intertumoral heterogeneity of glioblastomas[2]. Therefore, discovering additional ways of treating both primary and recurrent glioblastomas remains an important area of study.

In the past several decades, remarkable advances in harnessing the immune system to treat human cancers in the clinical setting have been made. One effective strategy has been the use of checkpoint blockade to target checkpoint proteins such as Programmed Cell Death 1/Programmed Cell Death 1 Ligand 1 (PD-1/PD-L1)[3]. In normal settings, checkpoint proteins and their associated ligands are an important immune regulator to prevent ongoing immune activity, but in the cancer setting, they become a mechanism in which cancers may exploit to evade the immune system. By utilizing therapies that block the interaction between these various checkpoint proteins on immune cells, such as T cells, and their ligands on tumor or other immune cells, checkpoint inhibitors work to reinvigorate the anti-tumor immune response to continue the attack on cancerous cells. In some cancer types, such as advanced melanoma and non-small cell lung cancer, the use of checkpoint blockade has led to significant improvement in patient survival and/or complete cures[4].

Unfortunately, with glioblastoma, the use of anti-PD-1 and other checkpoint blockade therapies have been largely ineffective in the clinical setting[5-7]. Reasons for resistance to checkpoint inhibition include: relative lack of targetable cancer-specific antigens (i.e. neoantigens or tumor-associated antigens), poor T cell priming by antigen presenting cells, a high concentration of

immunosuppressive immune cells in the tumor microenvironment, and mechanisms that exclude relevant anti-tumor immune cells from trafficking into the tumor site[8,9]. Therefore, there remains additional work to understand the how checkpoint blockade works or fails to work on the tumor infiltrating T cell and other immune cell populations in order to improve current therapies or to develop rational combinatorial strategies with checkpoint inhibition.

In this work we examined how neoadjuvant administration of anti-PD-1 therapy changes the glioblastoma microenvironment and impacts the glioblastoma infiltrating T cell population. Chapter 1 characterizes what the expression of PD-1 on patient tumor infiltrating and peripheral T cells indicates about the phenotype and function of T cells in glioblastoma patients[10]. Chapter 2 explores, using a high dimensional and multi-omics approach, how neoadjuvant anti-PD-1 therapy changes the tumor infiltrating immune cell composition in recurrent GBM patients[11]. Chapter 3 is a proof-of-concept study showing that considering the transcriptional profile of expanded intratumoral T cell subpopulations in patients treated with neoadjuvant anti-PD-1 can help guide the selection of relevant tumor-reactive T cells. In total, this work contributes to our growing understanding for how checkpoint inhibition in the neoadjuvant setting can be leveraged to better treat glioblastoma and improve patient outcomes.

CHAPTER 1: Expression of PD-1 by T cells in malignant glioma patients reflects exhaustion and activation

Abstract

Glioblastoma (GBM) is the most common primary malignant tumor in the central nervous system. Our recent pre-clinical work has suggested that PD-1/PD-L1 plays an important immunoregulatory role to limit effective anti-tumor T cell responses induced by active immunotherapy. However, little is known about the functional role that PD-1 plays on human T lymphocytes in malignant glioma patients. In this study, we examined the immune landscape and function of PD-1 expression by T cells from tumor and peripheral blood in malignant glioma patients. We found several differences between PD-1$^+$ tumor-infiltrating lymphocytes (TILs) and patient-matched PD-1$^+$ peripheral blood T lymphocytes. Phenotypically, PD-1$^+$ TILs exhibited higher expression of markers of activation and exhaustion than peripheral blood PD-1$^+$ T cells, which instead had increased markers of memory. A comparison of the T cell receptor variable chain populations revealed decreased diversity in T cells that expressed PD-1, regardless of the location obtained. Functionally, peripheral blood PD-1$^+$ T cells had a significantly increased proliferative capacity upon activation compared with PD-1$^-$ T cells. Our evidence suggests that PD-1 expression in glioma patients reflects chronically-activated effector T cells that display hallmarks of memory and exhaustion depending on its anatomical location. The decreased diversity in PD-1$^+$ T cells suggests that the PD-1 expressing population has a narrower range of cognate antigen targets compared to the PD-1 non-expression population. This information can be used to inform how we interpret immune responses to PD-1 blocking therapies or other immunotherapies.

Introduction

Glioblastoma (GBM) is the most common primary brain tumor in adults and remains one of the most lethal of all human cancers[12]. Current standard of care includes surgical resection, chemotherapy, and radiation therapy and is associated with a median survival of 12-18 months [13-15]. The dismal outcome of this disease clearly highlights the need for new approaches in therapy. Novel treatment strategies, such as GBM-targeted immunotherapy and vaccination therapy, have shown promise in both pre-clinical and clinical trials[16-20]. However, the survival benefit has been indeterminate. Antitumor immune responses induced by immunotherapy and, more specifically active vaccination in GBM, may in turn induce an adaptive immune resistance mechanism mediated by immune checkpoints such as signaling of programmed death 1 and its ligand (PD-1/PD-L1) [21-23].

PD-1 is a cell surface co-inhibitory receptor that is expressed on T cells after activation and limits the immune response, resulting in what is traditionally considered functionally “exhausted” T cells [24,25]. In normal physiologic states, the function of this immune checkpoint protein is to inhibit or reduce autoimmunity and to maintain homeostasis during chronic infections [26,27]. In the setting of cancer, the PD-1/PD-L1 pathway may be an adaptive mechanism by the tumor to evade anti-tumor immune attack. Although PD-1 has previously been considered to be a marker of terminally differentiated exhausted T cells, PD-1 expression may in fact be a marker of continued effector or memory function needed to maintain pathogen or tumor control while minimizing tissue damage in a chronic state [28]. In fact, a number of recent studies have shown that PD-1 expression of $CD8^+$ T cells early after activation may temporally coincide with rapid proliferation and production of signature effector cytokines and be an important signaling pathway in programming of memory $CD8^+$ T cells [29-31].

In this study, we set out to define and characterize PD-1 expression in tumor-infiltrating lymphocytes (TILs) and peripheral blood from patients diagnosed with malignant glioma.

Numerous studies have shown PD-L1 expression in GBM as well as PD-1 expression in a subset of GBM TIL [21,23,24]. PD-1 expression on malignant glioma TILs in comparison to peripheral blood has not been investigated, nor has the function of these malignant glioma PD-1$^+$ TILs been examined in this detail. We found that the proportion of TILs expressing PD-1 was significantly elevated when compared to T cells in patient peripheral blood and T cells from healthy controls. Furthermore, we found increased levels of activation and exhaustion markers on PD-1$^+$ TILs when compared to PD-1$^+$ peripheral blood T cells, while we found increased markers of memory/antigen experience on the peripheral blood PD-1$^+$ T cells. Our results highlight the complex relationship between PD-1 expression on T cells and its relation to exhaustion and chronic activation within human malignant brain tumors.

Glioma-infiltrating T cells have elevated expression of PD-1 and other markers of T cell exhaustion and activation compared to peripheral T cells.

We recently demonstrated a critical role for PD-L1 on T cells infiltrating murine gliomas, as well as analogous human tumors [21,23]. To examine the role of PD-1 in human glioma, we first analyzed the PD-1 expression profile using traditional flow cytometric approaches in TILs and matched peripheral blood from 14 malignant glioma patients undergoing surgical resection at UCLA Medical Center (**Fig. 1A**). The clinical and pathologic characteristics of our patient population are outlined in **Table 1**. Similarly, we simultaneously analyzed the expression of PD-1 in the peripheral blood T cells of 14 healthy donors (**Suppl Fig. 1A**).

PD-1 was significantly elevated in the CD3$^+$ TIL population (mean ± SE: 51.7% ± 7.2% compared to the CD3$^+$ glioma patient PBMC population (19.7% ± 1.8%, p=0.0005) and healthy donor PBMCs (17.0% ± 2.4%, p=0.02) (**Fig. 1A**). The proportion of TILs expressing PD-1 was significantly elevated in the CD3$^+$CD4$^+$ T cell population (mean ± SE: 53.2% ± 6.8%) as compared to patient peripheral blood (17.6% ± 2.6%, p<0.0004) or donor peripheral blood

(17.3% ± 1.9%, p<0.0001; **Suppl Fig. 1B**). Similarly, the percentage of $CD3^+CD8^+$ cells expressing PD-1 was also significantly higher in TILs (51.9% ± 7.39%) than on patient peripheral blood T cells (22.5% ± 3.13%; p<0.0023) or donor peripheral blood T cells (15.9% ± 2.24%; p<0.0005; **Suppl Fig. 1C**). In order to validate these findings independently, PD-1 expression was analyzed on GBM TILs, matched patient peripheral blood T cells, and normal controls from a separate cohort of six GBM patients and six healthy controls at the University of Heidelberg (Germany). Similarly, PD-1 expression was significantly increased in the GBM TIL population when compared to matched patient peripheral blood T cells and healthy patient's T cells (**Fig. 1B**).

Because PD-1 has typically been associated with an exhausted phenotype, in addition to PD-1, the expression of three other exhaustion markers (CTLA-4, TIM-3, and LAG-3) was measured in the patients from our German validation cohort (**Fig. 1C**). The GBM TIL population showed greater expression of TIM-3 and LAG-3 and marginal increase in expression of CTLA-4 compared to both healthy donor PBMC and patient PBMCs. To examine this further, we noted the percentage of cells in each population that showed one more of the exhaustion markers (**Fig. 1D**). The GBM TIL population showed the largest subpopulation of cells that expressed at least one of the exhaustion markers and the only population that contained cells that expressed more than two of the exhaustion markers. In contrast, peripheral blood T cells from matched patients rarely had up to two markers of exhaustion and T cells from healthy controls almost uniformly had no markers of exhaustion except for a small percentage with only one marker. Additionally, we examined the proportion of $CD3^+$ cells within each combination of exhaustion markers. There was a greater percentage of $CD3^+$ TILs expressing two or more exhaustion markers across all the different combinations of exhaustion markers than PBMCs from the patients or controls (**Fig. 1E**). Our results suggest that malignant glioma patients possess elevated frequencies of PD-1 and other exhaustion markers on T cells from the tumor and in the peripheral blood compared with normal healthy volunteers.

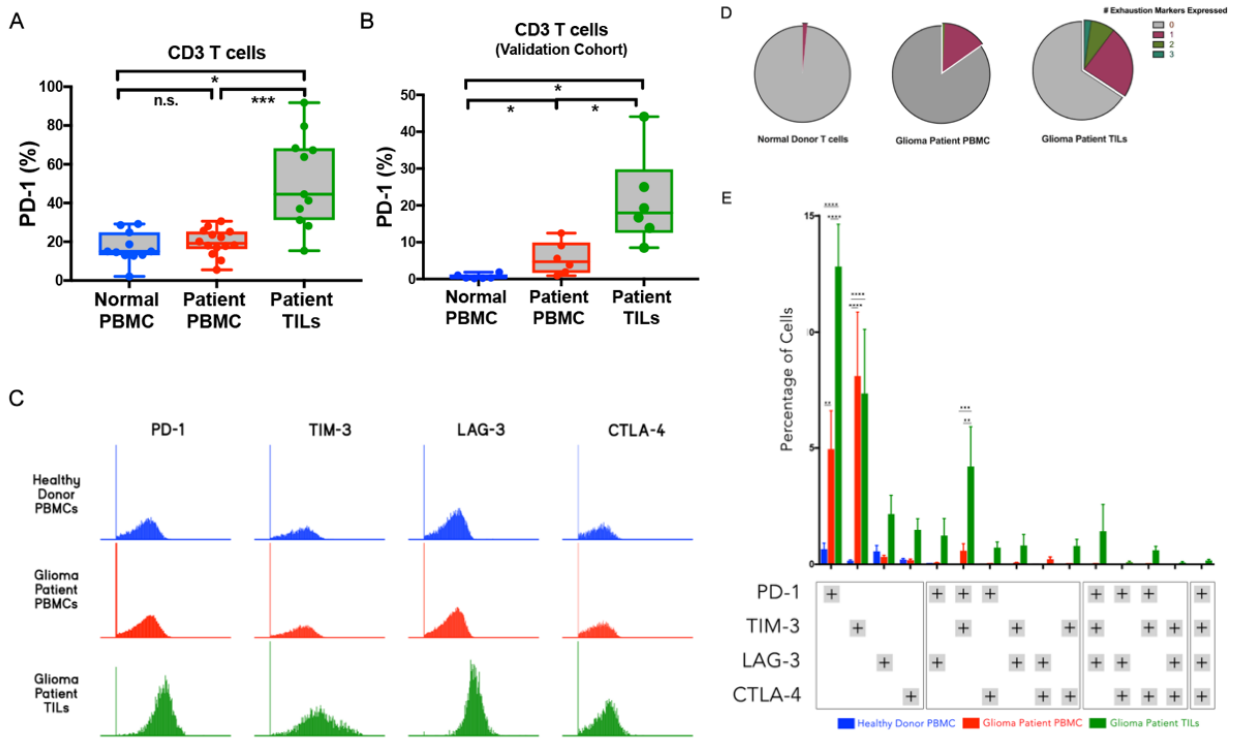

Figure 1: CD3⁺ T cells from malignant glioma patients demonstrate significantly elevated expression of PD-1 compared to healthy donor PBMCs and glioma patient PBMCs.

*A) Percent of PD-1 expression on CD3⁺ T cell from all the patient samples as measured by flow cytometry (*P<0.05, **P≤0.005, ***P≤0.0005).*

*B) The percentage of PD-1 expressing CD3⁺ T cells from a validation cohort of malignant glioma patients from the University of Heidelberg (*P≤0.05).*

C) Histogram of the expression levels of the different exhaustion markers (PD-1, TIM3, LAG3, CTLA-4).

D) Percentage of CD3⁺ T cells that express one or more markers of exhaustion (PD-1, TIM3, LAG3, CTLA-4).

E) *The percentage of cells expressing different combinations of the various exhaustion markers (**P≤0.005, ***P≤0.0005). Blue bars represent healthy donor PBMC samples, red bars represent glioma patient PBMC samples, and green bars represent glioma patient TIL samples.*

	Flow Cytometry/Gene Expression/TCR sequencing	CyTOF	Activation IFN-γ Studies	All Studies
Total Number	20	28	4	52
Mean age at diagnosis	51.3 years	51.4 years	43.1 years	50.7 years
Diagnosis	Number (percent)	Number (percent)	Number (percent)	Number (percent)
Glioblastoma	18 (90.0%)	20 (71.4%)	3 (75.0%)	41 (78.8%)
Gliosarcoma	0 (0%)	1 (3.6%)	0 (0%)	1 (1.9%)
Anaplastic Oligodendroglioma	0 (0%)	3 (10.7%)	0 (0%)	3 (5.8%)
Anaplastic Astrocytoma	2 (10.0%)	4 (14.3%)	1 (25.0%)	7 (13.5%)
Sex				
Male	13(65.0%)	17 (60.7%)	4 (100%)	34 (65.4%)
Female	7 (35.0%)	11 (39.3%)	9(0%)	27 (51.9%)
IDH				
Mutated	4 (20.0%)	7 (25.0%)	2 (50.0%)	13 (25.0%)
Wildtype	15 (75.0%)	21 (75.0%)	2 (50.0%)	38 (73.1%)
Unknown	1(5.0%)			1 (1.9%)
MGMT				
Methylated	10 (50.0%)	11 (39.3%)	0 (0%)	21 (40.4%)
Non-methylated	10 (50.0%)	16 (57.1%)	3 (75.0%)	29 (55.8%)
Unknown		1 (3.6%)	1 (25.0%)	2 (3.8%)
Presentation				
New diagnosis	14 (70.0%)	16 (57.1%)	0 (0%)	30 (57.7%)
Recurrent	6(40.0%)	12 (42.9%)	4(100%)	22 (42.3%)

Table 1: Patient Characteristics

To explore further the findings from our standard fluorescent antibody-based flow cytometry, we conducted CyTOF mass cytometry [32-34] on an additional 28 matching high-grade glioma patient TILs and PBMCs. A panel of immune lineage, memory, trafficking, activation, and exhaustion markers were used to stain these paired immune cell populations simultaneously (**Suppl Table. 1**). To analyze the $CD3^+$ $PD\text{-}1^+$ population from this set of patients, we employed FlowSom [35], an R package that uses machine learning algorithms to analyze mass cytometry data in an unbiased manner. Using this package, we ran a principal component analysis using the median expression levels of all the T cell markers from each individual patient as variables. An unsupervised clustering algorithm was used to generate a tSNE map of phenotypically defined population clusters. The principal component analysis showed a clear separation between the $CD3^+$ $PD\text{-}1^+$ PBMCs and the $CD3^+$ $PD\text{-}1^+$ TILs (**Fig 2A**). The unsupervised clustering algorithm grouped a majority of the $CD3^+$ $PD\text{-}1^+$ TILs in distinct clusters from the $CD3^+$ $PD\text{-}1^+$ PBMCs (**Fig. 2B, Suppl. Fig. 2a**).

We next looked at each individual marker and its median expression levels in all the PBMCs and TILs. For each individual marker, we highlighted the regions on the generated tSNE map where the marker was most highly expressed. For the T cell exhaustion markers, there was significant increase in TIM-3, PD-L1, and CTLA-4 in the TIL population compared to the PBMC population (**Fig. 2C**). Among T cell activation markers, there was a significant increase in expression of CD38 and HLA-DR in the TIL population compared to the PBMC population (**Fig. 2D**). Meanwhile, among the antigen experience and T cell memory markers: CD45RA, CD27, and CD127, there was a significant decrease in the TIL population compared to the PBMC population (**Fig. 2E**). In 4 recent patients, two additional T cell exhaustion markers CD39 and TIGIT were incorporated into our panel and the expression levels were measured between the PBMC and TIL groups. We found a significant increase in CD39 in the TIL population (**Suppl. Fig. 2c**) but a non-significant difference in TIGIT expression between the two groups (**Suppl. Fig. 2d**). A heat map of each analyzed patient's marker expression level was also generated.

There was increased expression of various exhaustion and activation markers in the TIL population and increased expression of antigen experience markers in the PBMC population (**Fig. 2F**). The results generated from the CyTOF data strongly suggest phenotypic differences exist between $CD3^+$ $PD\text{-}1^+$ cells from malignant glioma patient TILs and PBMCs.

In order to further investigate the possible relationship of PD-1 expression with T cell exhaustion, activation, and memory phenotypes we sought to characterize the gene expression of the $PD\text{-}1^-$ and $PD\text{-}1^+$ cells by performing a tailored comparison panel on the PBMCs and TILs from three randomly selected patients and PBMCs from one healthy individual using RNA hybridization probe technology [36]. When the normalized RNA counts of $PD\text{-}1^+$ T cells and $PD\text{-}1^-$ T cells were divided to create a ratio, we found that the ratio of $PD\text{-}1^+/PD\text{-}1^-$ gene expression in malignant glioma TILs had an elevated fold change for markers of exhaustion (TIM-3, CTLA-4, TIGIT) when compared to the peripheral blood T cells (**Suppl. Fig 3A**). Gene expression analysis of the same samples uncovered an increase in several activation markers (OX-40, 4-1BB, CD25, BIM, ICOS) of TILs when compared to patient peripheral blood T cells (**Suppl. Fig. 3B**). We saw a reversal of this $PD1^+/ PD1^-$ fold change for markers of memory (**Suppl. Fig. 3C**). These data suggest that PD-1 expression reflects activation and exhaustion in TILs and may be a marker of antigen experience in peripheral blood T cells of malignant glioma patients, similar to our findings from our phenotypic analyses.

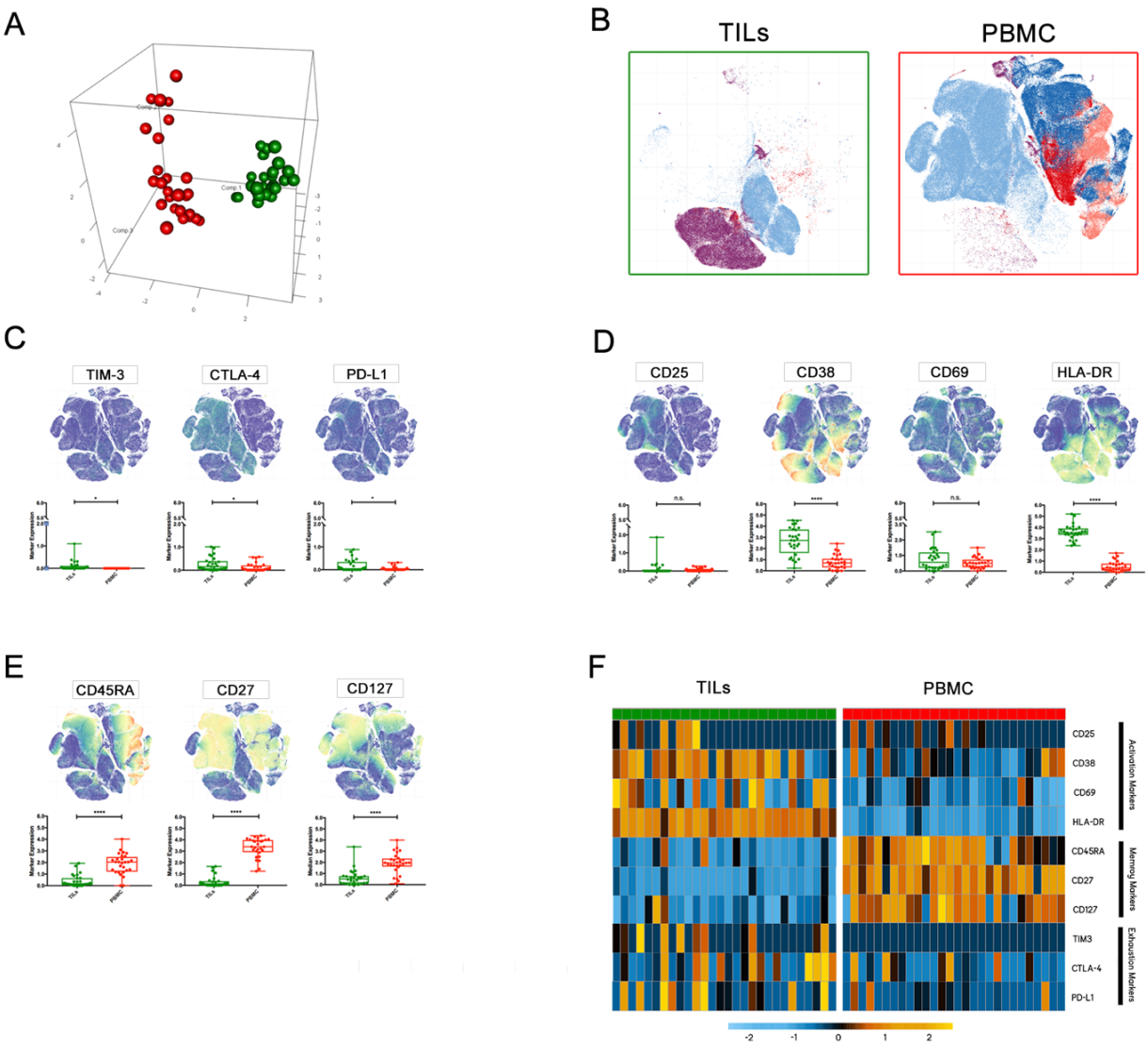

Figure 2: High dimensional analysis of mass cytometry data shows elevated expression of markers of activation and exhaustion on CD3⁺ PD-1⁺ TILs and markers of activation and antigen experience on CD3⁺ PD-1⁺ PBMCs from malignant glioma patients

A) A PCA plot showing CD3⁺ PD-1⁺ TILs (green dots) and PBMCs (red dots). Each dot represents an individual patient.

B) tSNE plots showing which clusters the CD3⁺ PD-1⁺ TILs were grouped in (green box) and which clusters the CD3⁺ PD-1⁺ PBMCs were grouped into (red box) by the clustering algorithm.

*C) The median expression levels of various activation markers in TILs (green dots) and PBMCs (red dots). The same tSNE plot as (B) was colored to show which cells expressed the particular marker (*P≤0.05, **P≤0.005, ***P≤0.0005).*

D) Antigen Experience/Memory markers.

E) Exhaustion markers.

F) A heat map of the median expression pattern for each of the exhaustion, activation, and memory/antigen experience markers for each individual patient.

PD-1$^+$ T cells demonstrate decreased T cell receptor diversity

We used high throughput DNA sequencing of the T cell receptor (TCR) V-β region to determine the TCR diversity of CD3$^+$ PD-1$^+$ and CD3$^+$ PD-1$^-$ T cells FACS-sorted from one matched patient tumor and PBMC samples, two additional distinct patient PBMC samples, and normal donor PBMCs. Since our data suggested that PD-1 reflects antigen experience, activation, and exhaustion in our malignant glioma patient samples, it was unclear what the TCR repertoire would reflect. In fact, we saw an increase in the diversity of PD-1$^-$ T cells from all populations of sorted T cells (**Fig. 3A**). As expected, we saw a trend toward the least amount of TCR diversity in the TIL population, but our limited number of sorted TIL precludes a clear assessment. Among the predicted productive TCR rearrangements, we also saw an expansion of clonal T cell populations in the PBMC and TIL populations in malignant glioma patients, possibly signifying expansion of tumor antigen-specific T cells not seen in healthy donors (**Fig. 3B)**. These findings suggest that PD-1$^+$ T cells are enriched for a restricted TCR population, regardless of where the cells were obtained.

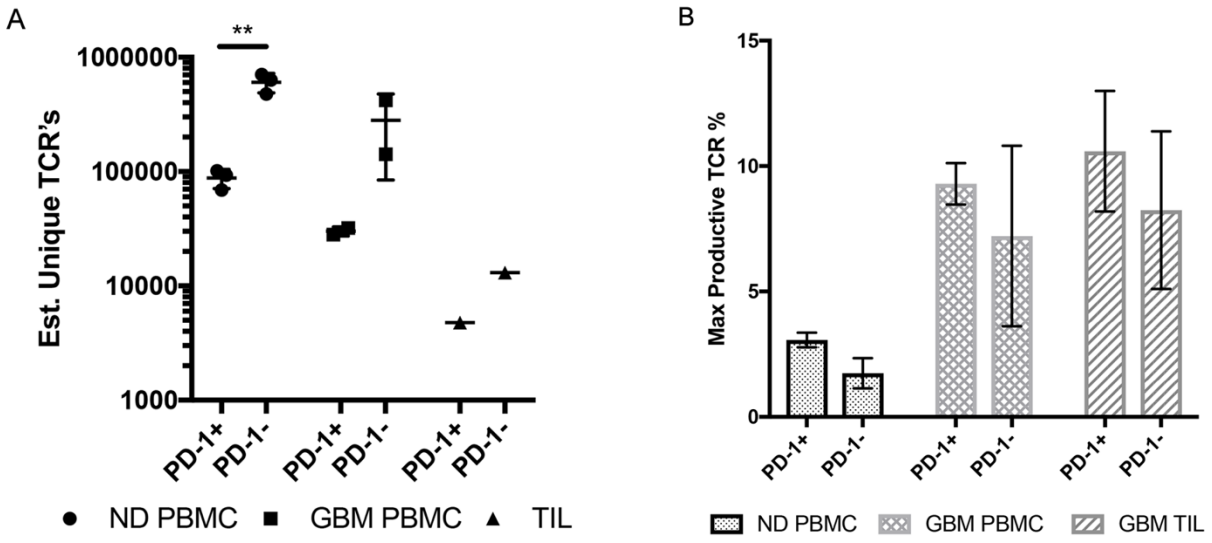

Figure 3: PD-1$^+$ T cells have decreased TCR diversity compared to PD-1$^-$ cells

*A) The number of estimated unique TCR sequences in PD-1$^-$ and PD-1$^+$ populations in healthy donor PBMC, glioma patient PBMC, and glioma patient TILs. Each point represents a single patient. Circle points represent healthy donor PBMCs. Square points represent glioma patient PBMCs. Triangle points represent glioma patient TILs. (**P≤0.005).*

B) The frequency of a specific TCR rearrangement in the populations. The populations shown are the CD3$^+$ PD-1$^-$ or CD3$^+$ PD-1$^+$ populations from healthy donor PBMCs (dotted bar), glioma patient PBMCs (the checkerboard bar), and glioma patient TILs (slanted stripes bar)

PD-1$^+$ peripheral T cells of GBM patients exhibit an increased rate of activation compared with PD-1$^-$ T cells.

To examine the functional differences between these T cell populations, we sorted PD-1$^+$ and PD-1$^-$ CD3$^+$ peripheral blood T cells from malignant glioma patients. Due to limited numbers of PD-1$^+$ T cells in non-expanded PBMC, we pooled together PBMCs from multiple patients. The sorted T cells were placed in culture and activated using agonistic CD3/28 antibodies. At 24 and 48 hours post activation, supernatants were collected and the interferon gamma (IFN-γ) levels measured. At 24 hours, the amount of IFN-γ produced by the CD3$^+$ PD-1$^+$ cells was 2.4x higher than the IFN-γ produced by the CD3$^+$ PD-1$^-$ cells (**Fig. 4a**). By 48 hours post stimulation, the amount of IFN-γ produced by the CD3$^+$ PD-1$^+$ cells was 8.8x higher than the IFN-γ produced by the CD3$^+$ PD-1$^-$ cells (**Fig. 4b**).

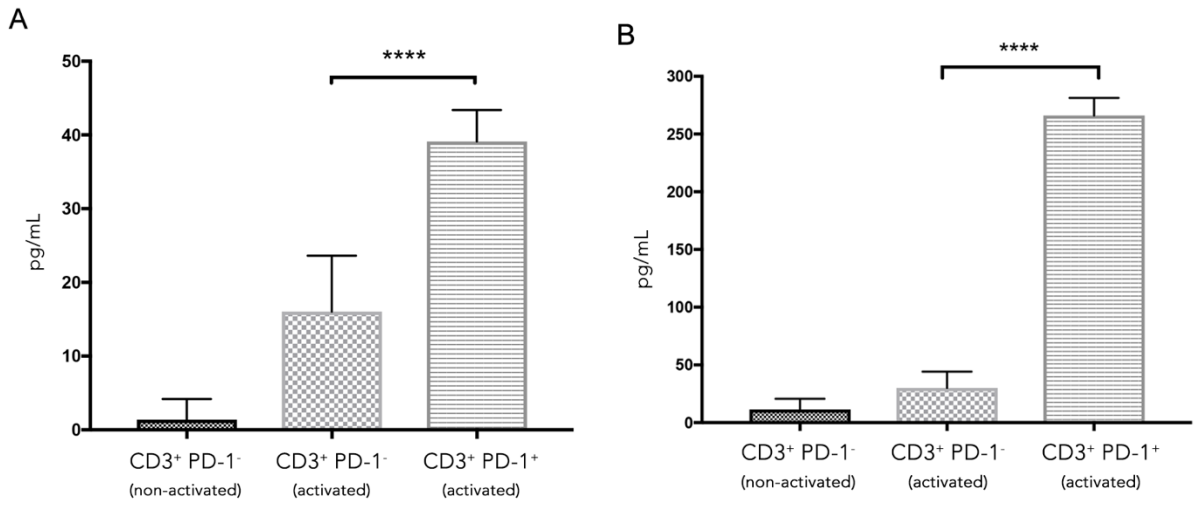

Figure 4: CD3$^+$ PD-1$^+$ T cells from pooled glioma patient PBMCs produce higher levels of IFN-γ compared to the CD3$^+$ PD-1$^-$ T cell population after T cell activation.

A) The amount of IFN-γ produced in CD3$^+$ PD-1$^-$, and CD3$^+$ PD-1$^+$ T cells from four glioma patient PBMCs 24 hours after CD3/CD28 activation. The dotted bar represents CD3$^+$ PD-1$^-$ T cells that were not activated. The checkerboard bar represents CD3$^+$ PD-1$^-$ T cells that were activated. The horizontal stripes bar represents CD3$^+$ PD-1$^+$ T cells that were activated. The results presented are a representative experiment that has been repeated multiple times with similar findings.

B) IFN-γ produced at 48hrs from the same set of cells as (A).

Discussion

We previously demonstrated that the PD-1/PD-L1 axis plays an important immunoregulatory role in anti-tumor T cell function induced by DC vaccination [21,23]. Several other studies have described T cell exhaustion and dysfunction within the tumor microenvironment and in relation to PD-1 expression. Thommen et al. showed in non-small cell lung cancer patients that PD-1 expressing T cells from the tumor had higher expression of various exhaustion markers, had higher upregulation of genes related to proliferation and activation, and were more clonal [37]. Analyzing TILS from both human GBM and murine tumor models, Woroniecka et al. showed that TILs had a more prominent exhaustion signature compared to the peripheral blood from GBM patients and from healthy donor PBMCs [38]. However, a comprehensive, high-dimensional analysis of PD-1 expression by human T lymphocytes in malignant glioma patients has not been described. In our study, we found several differences in both phenotypic characteristics and function between PD-1$^+$ TILs and matched PD-1$^+$ peripheral blood T lymphocytes extracted from malignant glioma patients. Notably, we found that PD-1 expression in the glioma TIL context may reflect T cell activation in addition to T cell exhaustion, but in the periphery, PD-1 expression on T cells may indicate activation and antigen experience **(Fig. 5)**.

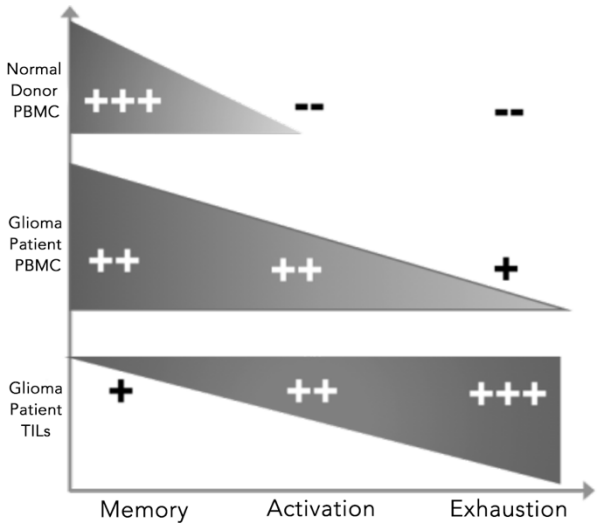

Figure 5: A schematic indicating what PD-1 expression means in the context of malignant glioma.

Expression of PD-1 on peripheral blood T cells of patients with malignant tumors, including malignant glioma, has previously been reported [39-44]. In most of these previous studies, PD-1 was described as a marker of exhaustion by terminally differentiated effector T cells. But these reports failed to describe the phenotypic and functional differences between PD-1$^+$ T cells in the peripheral blood and PD-1$^+$ TILs. In our study, we performed a comprehensive analysis of PD-1 expression on T lymphocytes isolated from the tumors and peripheral blood of malignant glioma patients. We found that PD-1 was significantly elevated in glioma patient TILs when compared to T cells in glioma patient peripheral blood and T cells from healthy controls. PD-1$^+$ TILs are enriched for markers of activation and exhaustion (CTLA-4, TIM-3, HLA-DR, and CD38) when compared to PD-1$^+$ peripheral blood T cells. In contrast, peripheral blood PD-1$^+$ T cells express a complete array of central memory, effector memory, and even the CD45RA$^+$ effector memory T cell subsets (CD45RO, CD45RA, CD27, and CD127), suggesting diverging functionality between PD-1$^+$ T cells obtained from distinct anatomical locale.

In the setting of chronic viral infections, similar trends have been observed. PD-1 expression has been associated with T cell exhaustion in both mouse LCMV models and humans infected with HIV [45,46]. In studies examining the transcriptional profile of the exhausted T cell population from a chronic LCMV mouse model, the exhausted population remained distinct from the memory T cell population and had increased transcription of various exhaustion markers such as PD-1, TIM-3 and CTLA-4 and activation markers such as ICOS and OX40 [47,48]. In contrast, previous reports have shown that in healthy controls, PD-1$^+$ peripheral CD8$^+$ T cells do not show exhausted characteristics, but instead exhibit hallmarks of effector memory T cells [49]. In a subset of the patients, CD45RO was included in the CyTOF analysis, which allowed a more thorough exploration of the T cell memory subsets. We found that the expression CD45RO is uniformly expressed on all CD3$^+$ PD1$^+$ T cells from the tumor but variably expressed by the peripheral blood population. In the peripheral blood, there are multiple populations of PD-1$^+$ T

cells that do not express CD45RO and are likely long-lived stem memory T_{SCM} or effector memory T_{EMRA} cells. Thus, our data support the conclusion that the phenotype of PD-1$^+$ T cells obtained from tumor tissue represents a chronically activated, exhausted effector T cell population (CD45RO$^+$ CD27$^-$ IL-7R$^-$ HLA-DR$^+$ CD38$^+$ TIM-3$^+$ LAG-3$^+$ CTLA-4$^+$), while the PD-1$^+$ T cell population obtained from peripheral blood represents the full complement of memory T cell populations (T_{CM}, CD45RO$^+$ CD27$^+$ CD45RA$^-$ IL-7R$^+$; T_{EM}, CD45RO$^+$ CD45RA$^-$ CD27$^-$ IL-7R$^-$; and T_{EMRA}, CD45RO$^-$ CD27$^-$ CD45RA$^+$ IL-7R$^-$). Therefore, our data would suggest that PD-1 expression by peripheral blood T cells may not be a good surrogate or indicator for exhaustion or tumor immune evasion. Such information must be considered when applied as a biomarker in clinical immunotherapy trials.

Interestingly, we found that PD-1 expression was associated with increased T cell receptor clonality and decreased diversity in both the TIL population and peripheral blood T cells of malignant glioma patients. As such, increased clonal expansion of the PD-1$^+$ T cell population may reflect the activation and expansion of specific anti-tumor antigen T cells when compared to PD-1- T cells, though future studies are needed to confirm this. Additionally, our CyTOF data revealed a significant increase in expression of CD39 in the CD3$^+$ PD-1$^+$ TIL population compared to the CD3$^+$ PD-1$^+$ PBMC population. CD39, an extracellular ATPase commonly associated with regulatory T cells, has been shown to be co-expressed with PD-1 on antigen-specific but exhausted CD8$^+$ T cells in a chronic viral setting [50]. More recently, CD39 has been proposed to be expressed by tumor specific T cells [51,52]. The increase of clonality and CD39 expression in the PD-1$^+$ TILs further supports their dual function phenotype of anti-tumor specific activation and exhaustion. Increased TCR clonality has been correlated with better outcomes after anti-PD-1 therapy in melanoma and has been associated with higher PD-1 expression in soft tissue sarcomas [22,53]. Further investigation is needed to study the association

between TCR clonality and PD-1 expression in the context of tumor antigen-specific T lymphocytes.

Finally, to characterize PD-1$^+$ peripheral blood T cells in malignant glioma patients, we investigated the functional activation differences between PD-1$^+$ and PD-1$^-$ peripheral blood T cells from GBM patients. Traditionally, it has been held that effector, memory, and naïve T cells have different response rates, as measured by amount of IFN-γ produced, after activation. We found that PD-1$^+$ GBM patient PBMC T cells exhibited an increased rate of IFN-γ production when compared to PD-1$^-$ PBMC T cells from the same patients. Increased IFN-γ is consistent with an activated memory T cell phenotype further highlighting that PD-1 expression in peripheral T cells is not a marker of exhaustion as we would expect in the PD-1$^+$ population in the tumor microenvironment.

In conclusion, we demonstrate that PD-1 expression in malignant glioma patients reflects chronically-activated effector T cells that display both hallmarks of memory and exhaustion depending on its location. The use of anti-PD-1/PD-L1 antibody blockade is currently being studied in malignant glioma clinical trials. Further exploration of the effect of these check point inhibitors on PD-1 expressing T cells in different anatomical environments is warranted both to understand the use of PD-1 expression as a therapeutic biomarker as well as its importance for clinical efficacy.

Methods

Patients

We collected 52 patient tumor and blood specimen samples and an additional 14 peripheral blood samples from healthy donors at University of California, Los Angeles (Los Angeles, CA). In parallel, matched TILs and peripheral blood were obtained from 6 consenting patients with glioblastoma who presented to the University of Heidelberg (Heidelberg, Germany) neurosurgery service for surgical removal of their tumors. All patients provided written informed consent, and this study was conducted in accordance with recognized ethical guidelines and under Institutional Review Board–approved protocols from both institutions.

Collection of PBMCs for immune monitoring

Peripheral blood was drawn from patients prior to surgical resection of their gliomas. Once drawn, we diluted peripheral blood at 1:1 dilution of RPMI media (Thermo Fisher Scientific catalog no. MT10041CV); peripheral blood mononuclear cells (PBMC) were harvested through subsequent extraction with Ficoll (Thermo Fisher Scientific catalog no. 45-001-750) gradient. After a series of two washes in RPMI media, we placed cells in freezing media made of 90% Human AB serum (Thermo Fisher Scientific catalog no. MT35060CI) and 10% DMSO (Sigma catalog no. C6295-50ML) and stored in liquid nitrogen.

Collection of TILs

TILs were collected in two ways. In the first method, we collected tumor and digested the tissue via incubation with collagenase (1 mg/mL; Advance Biofactures Corporation) and DNAse (0.02 mg/mL; Sigma catalog no. D4263-5VL) in RPMI media overnight on the day of resection. TILs were isolated using Percoll (Sigma catalog no. P4937) gradient and washed in RPMI twice. In the second method, patient-resected tumors were first digested using Miltenyi's Brain Tumor

Dissociation Kit (Miltenyi Biotec catalog no. 130-095-42) and gentleMACS Dissociator (catalog no. 130-093-235) and labeled with CD45þ microbeads (catalog no. 130-045-801). CD45þ cells were positively selected for using Miltenyi LS columns (catalog no. 130-042-401) and MidiMACS Separator. TILs were frozen in the same freezing media as the PBMCs.

Flow cytometric analysis of PBMCs and TILs

We thawed donor PBMCs and patient PBMCs and TILs at 37°C for 3 minutes in a water bath and immediately washed with RPMI media to remove DMSO. We resuspended cells at $1x10^6$ cells/ 100 mL PBS.

In the characterization of PD-1 expression of TILs and PBMCs, we first stained cells with live-dead Zombie Yellow stain (BioLegend, catalog no. 423104). In two separate experimental reactions, we stained cells with a 7-antibody and an 8-antibody panel. Two antibody panels were necessary to investigate all of the surface markers of interest due to the spectral limitations of the flow cytometer. The first antibody cocktail included seven anti- bodies: CD3 Pe-Cy7 (eBioscience, catalog no. 25-0038-42), CD4 Alexa Fluor 700 (BD Biosciences, catalog no. 557922), CD8 Pacific Blue (BD Biosystems, catalog no. 558207), CD16 FITC (BD Biosystems, catalog no. 555406), CTLA-4 PE (BD Biosystems, catalog no. 555853), PD-1 AF647 (eBioscience, catalog no. 51-9969-73), and CD69 PerCP-CY5.5 (BD Biosystems, catalog no. 560738) antibodies where each antibody was diluted to a 1:40 antibody to buffer ratio. The second 8-antibody cocktail contained CD3 Pe-Cy7 (eBioscience, catalog no. 25-0038-42), CD4 Alexa Fluor 700 (BD Biosystems, catalog no. 557922), CD8 Pacific Blue (BD Biosystems, catalog no. 558207), CD16 FITC (BD Biosystems, catalog no. 555406), CD19 PE (BD Biosystems, catalog no. 555413), CD25 APC-Cy7 (BD Biosystems, catalog no. 557753), CD127 AF647 (BD Biosystems, catalog no. 558598), and CD69 PE-Cy5 (BD Biosystems, catalog no. 555532) antibodies at the same dilution as above.

We used a BD LSRII flow cytometer and the BD FACS diva software to analyze all cell samples. Cytometer settings were restricted to the nine colors used. We used unstained controls to adjust FSC and SSC voltages such that the lymphocyte population became visible and then acquired single-color compensation controls, adjusting voltages such that the stained cells did not exceed 105. We set gates on stained controls in comparison with the negative control and recorded data from all samples, while subsequently applying compensation controls. We recorded staining expression at 80,000 to 100,000 events per sample, as the quantity of T cells was variable from specimen to specimen. Thus, we analyzed the data acquired from the flow cytometer by using frequency measurements rather than absolute numbers to compare sample expression profiles using FlowJo.

Mass cytometry

Patient PBMCs and TILs were collected as described above. Between 1 to 2 million patient PBMCs and TILs were labeled with Cell-ID Cisplatin (Fluidigm, catalog no. 201064) to assess for live/dead and then labeled with a variety of metal-conjugated antibodies. From the patient PBMCs, $1x10^6$ cells were set aside and labeled with a smaller panel containing only cell lineage markers to aid in setting the proper gates of other markers. After labeling, cells were fixed using MaxPar Fix and Perm buffer (Fluidigm, catalog no. 201067) and labeled for single-cell discrimination with Cell-ID Intercalator-Ir (Fluidigm, CA 201192A) and run on the Helios CyTOF system.

The collected mass cytometry data were analyzed as described previously[54]. Briefly, samples were normalized utilizing a bead standard, then manually gated to remove debris and dead cells. Raw marker intensities were transformed using hyperbolic inverse sine with cofactor of 5. Cell population identification was carried out utilizing the FlowSOM[35] and ConsensusClusterPlus packages in R using 11 lineage markers, with the number of clusters determined by elbow criterion. For differential analysis of cell population abundance and functional marker

expression, we fit fixed and mixed linear models to our data and performed testing using the general linear hypothesis function glht in R. To account for multiple testing, we applied the Benjamini–Hochberg adjustment with a false discovery rate of 5%.

FACS of $CD3^+$ $PD\text{-}1^+$ and $CD3^+$ $PD\text{-}1^-$ T-cell populations

As described above, we thawed frozen donor PBMCs and patient PBMCs and TILs, stained samples with CD3 Pe-Cy7 (eBioscience, catalog no. 25-0038-42) and PD-1 AF647 (BD Biosystems, catalog no. 558598) and sorted samples with the Aria II cell sorter (Becton Dickinson) into $PD\text{-}1^+$ and $PD\text{-}1^-$ T-cell populations. We defined $PD\text{-}1^+$ T cells as CD3þ and $PD1^+$ and $PD\text{-}1^-$ T cells as $CD3^+$ and $PD1^-$.

RNA gene expression

We used the NanoString nCounter Dx Analysis System, which measures the expression of 511 human immune function genes through digital readouts of the abundance of mRNA transcripts to analyze cell lysates of PD-1–expressing and PD-1 void cells [36]. The nCounter Dx Analysis System uses gene-specific probe pairs that hybridize directly to mRNA samples. A Reporter Probe carries the fluorescent signal; a Capture Probe allows the complex to be immobilized for data collection. We included, in each assay, six positive quality controls comprised of a linear titration of in vitro transcribed RNA transcripts and corresponding probes, and eight negative quality controls consisting of probes with no sequence homology to human RNA sequences. Each Human Immunology assay run includes a reference sample consisting of in vitro transcribed RNAs of the 13 targets that are used for normalization purposes.

TCR V-β sequencing

We extracted genomic DNA from sorted $CD3^+$ $PD\text{-}1^+$ and $CD3^+$ $PD\text{-}1^-$ T cells from malignant glioma patient TILs and PBMCs and from healthy donor PBMCs using DNeasy Blood & Tissue

Kit (Qiagen catalog no. 69504) and sequenced DNA at the T-cell receptor (TCR) V-β CDR3 region using high-throughput sequencing in collaboration with Adaptive Biotechnologies, as we have recently published[55].

IFN-γ activation assay

$CD3^+$ $PD\text{-}1^-$ and $CD3^+$ $PD\text{-}1^+$ cells were sorted in a similar manner described above. In a 96-well plate, we added $2x10^5$ cells into each well at a concentration of $1x10^6$ cells/mL. For the cells that were to be activated, we added 50 ng/mL anti-CD3 Ab (BioLegend, catalog no. 317304) and 1 mg/mL anti-CD28 Ab (BD Biosciences, catalog no. 555725). In all wells, we added 50 IU/mL IL2. After 24 hours, the supernatant was collected and fresh media with 50 IU/mL IL2 were added in each well, and the supernatant was collected 24 hours later (total of 48 hours after activation). To measure IFN-γ levels, we used the Human IFN-γ Uncoated ELISA Kit (Thermo Fisher Scientific, catalog no. 88-7613-86).

Statistical analysis

The percentage of T lymphocytes expressing the various T-cell markers studied were compared between patient PBMCs, TILs, and donor PBMCs. Unpaired Welch t test was applied to compare the means of the frequencies of expression with two-sided P values (*, $P < 0.05$; **, $P < 0.005$; ***, $P < 0.0005$).

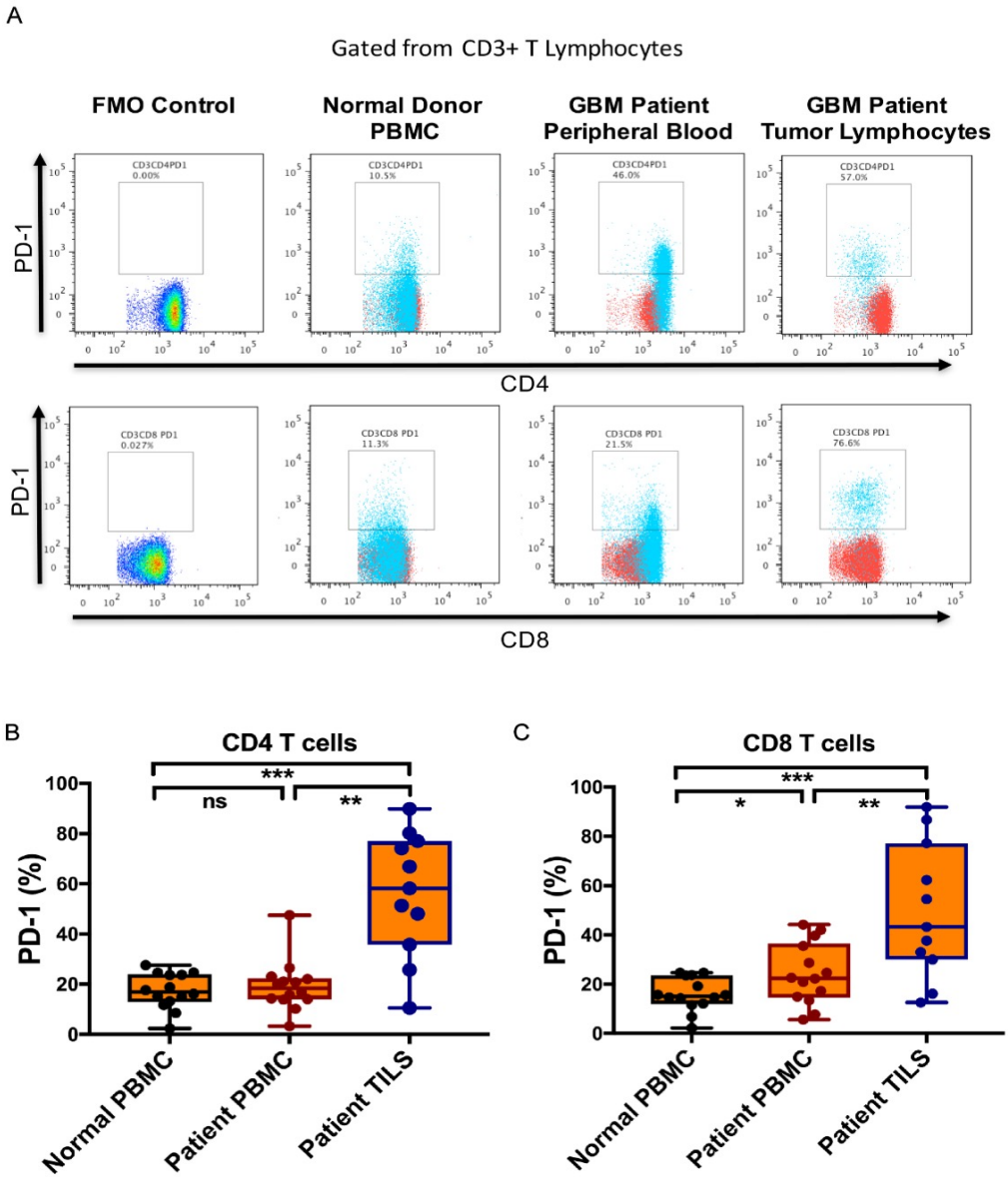

Supplementary Figure 1: T cells from GBM patient TILs show highest expression of PD-1 compared to healthy donor PBMC and GBM patient PBMCs

A) A representative flow cytometry plot measuring PD-1^{+} expression on CD4^{+} and CD8^{+} T cells from Healthy Donor PBMC, glioma Patient PBMC, and glioma patient TILs.

B) Percent of PD-1 expression on CD4^{+} T cells from all the patient samples as measured by flow cytometry.

C) Percent of PD-1 expression on CD8^{+} T cell from all the patient samples as measured by flow cytometry.

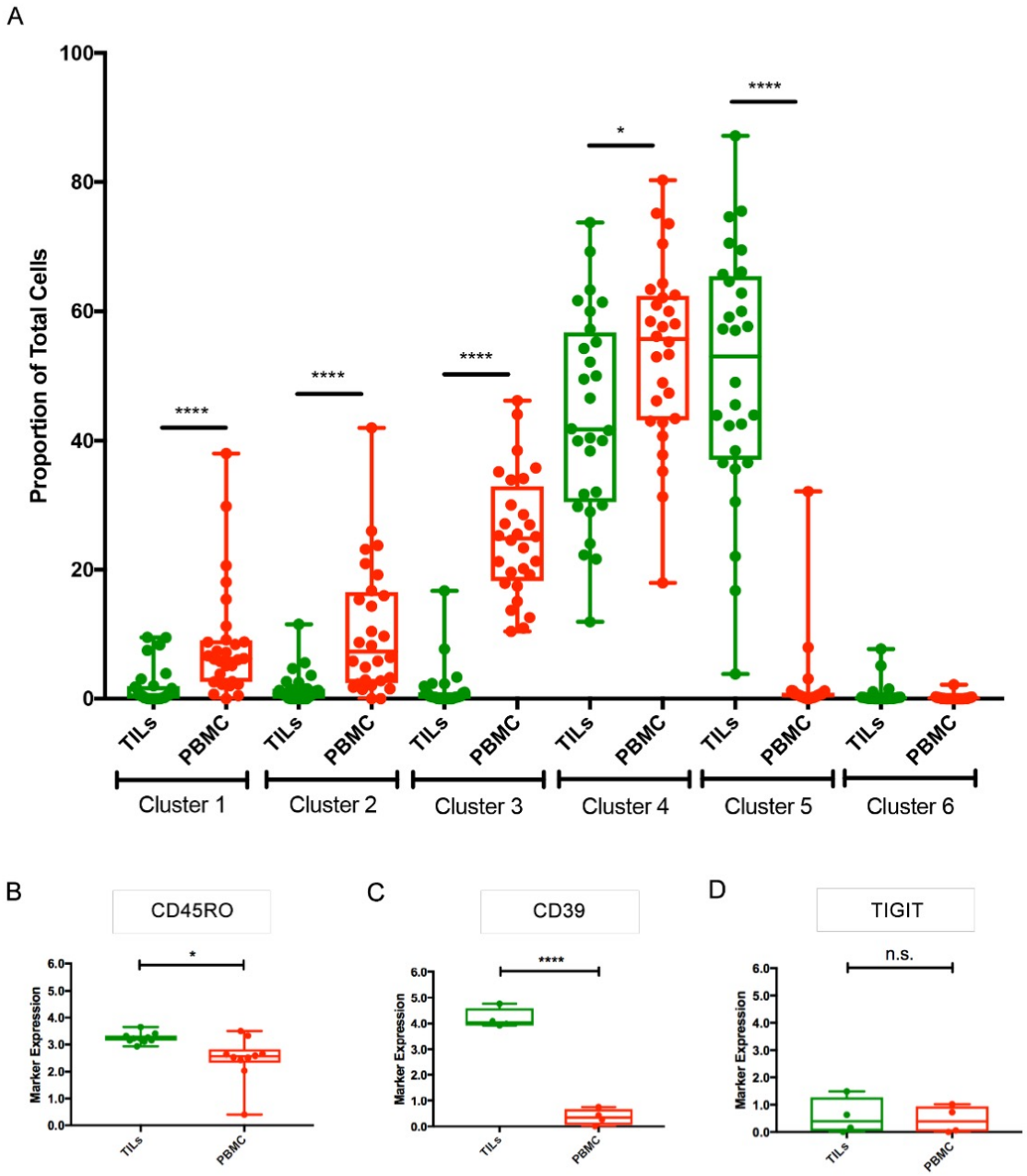

Supplementary Figure 2: Additional CyTOF data

*A) The percentage of the CD3⁺ PD-1⁺ cells from the TIL (green dots) and PBMCs (red dots) in each cluster (*P<0.05, ***P≤0.0005). Each dot represents a single patient.*

*B) The median expression level of CD45RO in a subset of 10 patients (*P<0.05).*

*C) The median expression level of CD39 in a subset of 4 patients (***P≤0.0005).*

***D)** The median expression level of TIGIT in a subset of 4 patients.*

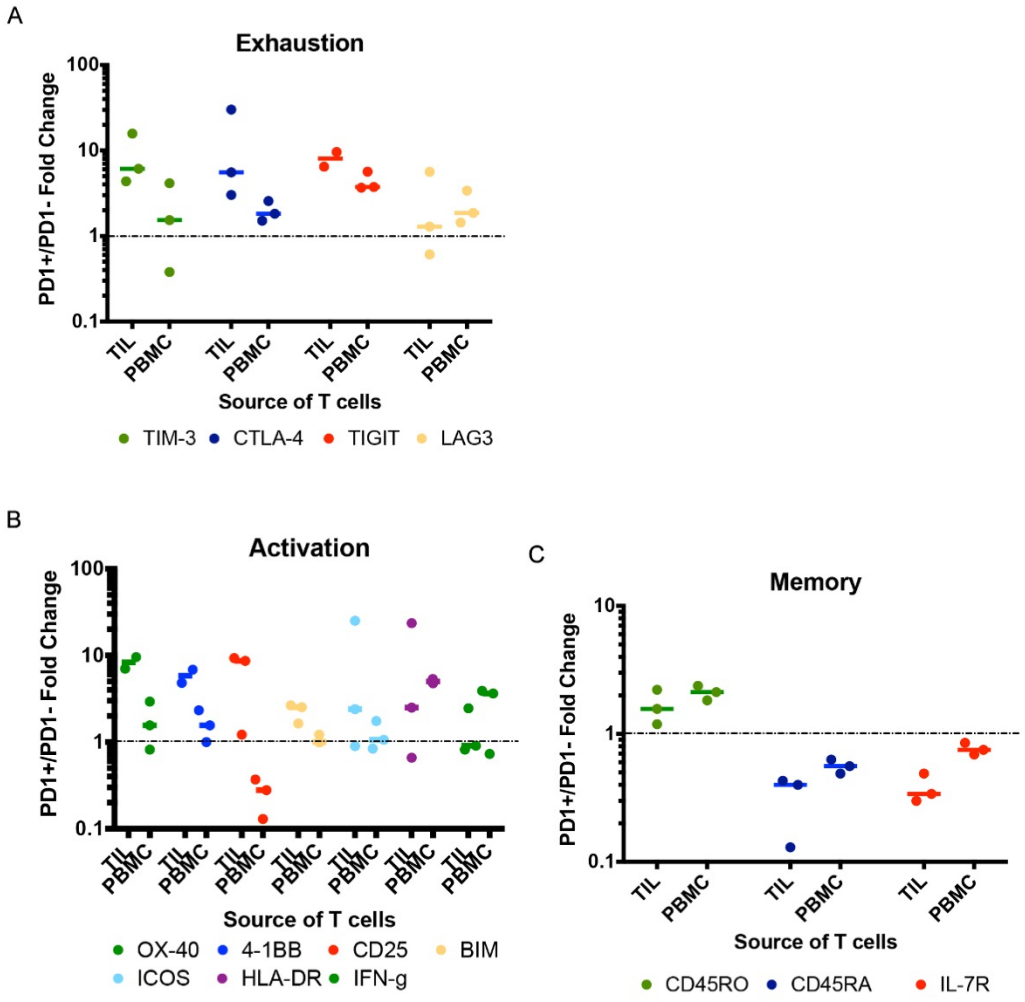

Supplementary Figure 3: Gene expression analysis shows increased transcription of activation and exhaustion genes in the PD-1$^+$ population in glioma TILs and of antigen experienced genes in the PD-1$^+$ population in glioma PBMCs (each dot represents a distinct patient).

A) Fold change of various exhaustion markers between PD-1$^+$ and PD-1$^-$ cells in glioma TILs and PBMCs.

B) Fold change of various activation markers between the PD-1$^+$ and PD-1$^-$ cells in glioma TILs and PBMCs.

C) Fold change of various memory markers between the PD-1$^+$ and PD-1$^-$ cells in glioma TILs and PBMCs.

Lineage Markers		
Metal Label	Specificity	Clone
142Nd	CD19	HIB19
145Nd	CD4	RPA-T4
146Nd	CD8	RPA-T8
151Eu	CD14	M5E2
158Gd	CD33	WM53
159Tb	CD11c	Bu15
163Dy	CD56	NCAM16.2
164Dy	CD15/SSEA-1	W6D3
165Ho	CD16	3G8
168ER	CD206	MMR
170ER	CD3	UCHT1
209Bi	CD11b	ICRF44

Exhaustion Markers		
Metal Label	**Specificity**	**Clone**
148Nd	CD274 /PD-L1	29E.2A3
150Nd	CD223 (LAG-3)	11C3C65
153Eu	TIM-3	F38-2E2
155Gd	CD279(PD-1)	EH12.2H
161Dy	CD152 (CTLA-4)	14D3
160Gd	CD39	A1
141Pr	TIGIT	MBSA43

Activation Markers		
Metal Label	Specificity	Clone
143Nd	CD25	M-A251
144Nd	CD69	FN50
172Yb	CD38	HIT2
174Yb	HLA-DR	L243

Antigen Experience Markers		
Metal Label	Specificity	Clone
167ER	CD27	O323
169Tm	CD45RA	HI100
176Yb	CD127 (IL-7Ra)	A0195D5
154Sm	CD45RO	UCHL1

Supplementary Table 1: Antibodies used in Mass Cytometry Analysis

CHAPTER 2: Neoadjuvant PD-1 blockade induces T cell and cDC1 activation but fails to overcome the immunosuppressive tumor associated macrophages in recurrent glioblastoma

Abstract:

Primary brain tumors, such as glioblastoma (GBM), are remarkably resistant to immunotherapy, even though pre-clinical models suggest effectiveness. To understand this better in patients, here we take advantage of our recent neoadjuvant treatment paradigm to map the infiltrating immune cell landscape of GBM and how this is altered following PD-1 checkpoint blockade using high dimensional proteomics, single cell transcriptomics, and quantitative multiplex immunofluorescence. Neoadjuvant PD-1 blockade increases T cell infiltration and the proportion of a progenitor exhausted population of T cells found within the tumor. We identify an early activated and clonally expanded CD8+ T cell cluster whose TCR overlaps with a CD8+ PBMC population. Distinct changes are also observed in conventional type 1 dendritic cells that may facilitate T cell recruitment. Macrophages and monocytes still constitute the majority of infiltrating immune cells, even after anti-PD-1 therapy. Interferon-mediated changes in the myeloid population are consistently observed following PD-1 blockade; these also mediate an increase in chemotactic factors that recruit T cells. However, sustained high expression of T-cell-suppressive checkpoints in these myeloid cells continue to prevent the optimal activation of the tumor infiltrating T cells. Therefore, future immunotherapeutic strategies may need to incorporate the targeting of these cells for clinical benefit.

Introduction:

Recurrent glioblastoma is associated with a median overall survival of 24-44 weeks[56-58]. Although immunotherapy such as checkpoint blockade has revolutionized the treatment of

several cancers, its benefit in glioblastoma (GBM) has been limited to small randomized trials in the neoadjuvant setting[59], with no FDA approval thus far.

In other cancer types, characterization of the immune composition of the tumor microenvironment has revealed significant heterogeneity across tumor subtypes and patients, with high diversity in the intratumoral compartments[60-65]. In certain cases, unique novel lymphoid or myeloid subsets emerge within the tumor that are absent from adjacent normal tissue or peripheral blood, and such specific immune compositions may affect survival. In the GBM tumor microenvironment, myeloid cells are known to comprise a significant proportion of immune cells[60,66-72].

We previously demonstrated that neoadjuvant anti-PD-1 therapy (neo-aPD1) was associated with improved overall and progression-free survival in a small randomized phase 1 clinical trial[59]. Treatment with PD-1 blockade prior to surgical debulking induced a significant increase in interferon-γ-related gene expression and an associated decrease in cell cycle-related gene expression. However, this approach was performed on bulk tissue and did not capture the perturbations in specific cell types within the tumor microenvironment, and although neo-aPD1 was associated with a significant survival benefit, it was not curative, suggesting that there are other interactions within the microenvironment that prevent neo-aPD1 from being completely effective.

The effect of neo-aPD1 is believed to be predominantly driven by re-activation of exhausted T cells. However, PD-1 blockade may also shape the tumor microenvironment and influence non-T cell populations[73,74]. One publication performed high dimensional analysis of the effect of checkpoint blockade in altering the immune landscape of GBM[75]; however, this study was limited to a small number of patients. Another recent publication examined the tumor myeloid

and dendritic cell populations of patients with newly diagnosed GBM or recurrent GBM; three of the latter were treated with neo-aPD1 24 hours prior to surgery[76]. The authors noted that this would be too short of a timeframe for the neo-aPD1 treatment to meaningfully affect the immune composition of the tumor microenvironment. Therefore, the abundance and differentiation of T cell and myeloid cell subsets after the administration of neo-aPD1 in the GBM setting is not well characterized and additional work is needed to provide a more comprehensive understanding of the effects of immunotherapy in GBM. To address this question, we used time-of-flight mass cytometry (CyTOF) and/or single-cell RNA sequencing (scRNAseq) to analyze the tumor infiltrating CD45+ immune cell population at the single cell level of 69 GBM patients who underwent surgical resection at the University of California, Los Angeles.

Neo-aPD1 significantly increases the proportion and number of T cells in the tumor microenvironment but the immune microenvironment remains largely dominated by myeloid cells. Single-cell RNA and TCR sequencing analysis shows that neo-aPD1 expands an early activated, cytotoxic CD8 T cell population in the peripheral blood that trafficks into the tumor microenvironment and produces a population of progenitor exhausted CD8 T cells that has been previously identified in the chronic viral setting[77-79] and in melanoma[80].

Our scRNAseq analysis also shows that the T cell populations activated by neo-aPD1 produces chemotactic factors that recruit DCs (*XCL1*, *XCL2*) and additional T cells (*CCL5*) into the tumor microenvironment. Newly trafficked T cells from the periphery expand but eventually transition into a progenitor exhausted state, potentially through the engagement of the TIGIT and CTLA-4 immune checkpoints on these cells. In the myeloid population, neo-aPD1 is associated with IFN-driven transcriptional changes, leading to some myeloid populations that secrete T cell chemotactic factors such as CXCL9/10/11. However, the overall myeloid population is still dominated by multiple tumor associated macrophage (TAM) populations which highly express

NECTIN2 and *CD86*, the genes encoding the interaction partner of TIGIT and CTLA-4. Indeed, the interactome analysis based on the single cell gene expression indicates that neoadjuvant anti-PD-1 is associated with increased interactions between the T cell checkpoints TIGIT and CTLA4 on myeloid populations and their respective receptors in the activated T cell populations. Moreover, neo-aPD1 induces a CXCR4+ TAM population and does not reduce multiple myeloid populations that are often associated immune suppression.

Collectively, in this work, we show that treatment with neo-aPD1 remodels the cellular immune composition of the GBM tumor microenvironment across multiple immunologic nodes. Despite the alterations in the tumor-infiltrating lymphocyte (TIL) and cDC populations following neoadjuvant checkpoint blockade, T-cell-suppressive myeloid cells still dominate the immune landscape of these tumors. Additional strategies targeting TIGIT and/or CTLA-4 may be needed to improve the strength and durability of antitumor T cell response in neo-aPD1 treated GBM patients.

Patient Characteristics, Data Acquisition, and Initial Data Analysis of all immune populations

To understand how neo-aPD1 changes the immune landscape of the tumor microenvironment, we used CyTOF mass cytometry (CyTOF), single-cell RNA sequencing (scRNAseq), and/or multiplex immunofluorescence (mIF) to analyze the tumor infiltrating CD45+ immune cells from a total of 69 unique GBM patients (**Fig 1a, b**). At surgery, 27 of these patients had newly diagnosed GBMs (GBM.new), 22 of these patients had recurrent GBM without prior immunotherapy (GBM.rec), and 20 of these patients had recurrent GBM with neo-aPD1 therapy (GBM.pembro). 34 of the patients had tumor infiltrating immune cells that were analyzed with both CyTOF and scRNAseq, 29 patients with CyTOF alone, and 6 patients with scRNAseq alone. We also analyzed PBMCs from 5 GBM.rec, 8 GBM.pembro; and 2 healthy donor patients using scRNAseq. The GBM patients whose PBMCs were analyzed also had their tumor-infiltrating immune cells analyzed with scRNAseq. We collected tumor sections for 20 patients (8 GBM.rec and 12 GBM.pembro) to stain with multiplex immunofluorescence, 5 of whom were also analyzed with either CyTOF and/or scRNAseq.

For the initial CyTOF analysis, we sampled up to 20,000 of the live cells per patient (n=1,056,057 total cells) and performed unbiased clustering using ClusterX[81] based on the expression of 22 cell surface markers (**Supp. Data 1**) across our 63 patient cohort. The tumor infiltrating immune cell clusters were grouped into six populations (**Fig 1c, d, Supp. Figure 1a-c**): T cells (CD3+), myelo-monocytic cells (CD14/CD33+), granulocyte (CD15+), natural killer cells (CD56+ and CD16+), and two uncharacterized populations (CD56+ and no markers). We also analyzed tumor-infiltrating immune cells from 40 GBM patients (n=156,766 cells) using scRNAseq. We selected the clustering resolution that separated the cells into six clusters (**Fig 1e**): one cluster of lymphoid cells based off expression of *CD3D*, two clusters of myeloid cells

based off expression of *CD14* and *FCGR3A/CD16*, one cluster of stressed/dying cells (dominated by long non-coding RNAs like *MALAT1, NEAT1* and heat shock proteins (HSPs)), one cluster of tumor or normal brain cells based off expression of *GFAP* and *SOX2*, and one cluster of cells that had too few reads to accurately classify (**Supp. Figure 1d, Supp. Data 2**). It is possible that the CyTOF clusters that had little marker expression or only CD56 expression corresponds to the tumor cluster from our scRNAseq analysis.

Neo-aPD1 therapy increases the overall T cell infiltrate in the GBM microenvironment

We began our analysis looking at the overall changes to the tumor-infiltrating T cell and myeloid cell compartments after neo-aPD1. Our CyTOF analysis showed a significant increase in the proportion of CD3+ T cells in the tumor infiltrating immune populations in the GBM.pembro group and a corresponding decrease in the myelo-monocytic populations compared to the GBM.rec groups (**Fig 1f, g**). Our scRNAseq analysis showed a similar trend towards decreased proportion of the myeloid population (**Supp. Figure 1e, Supp. Data 2**).

To evaluate whether the increased proportion of T cells was caused by increased T cell infiltration into the tumor and not by loss of myeloid cells in the tumor, we calculated the total number of the T cells and myelo-monocytic cells per mg of tumor dissociated. The absolute number of T cells per mg of tumor significantly increased in GBM.pembro compared to GBM.new and GBM.rec (**Fig 1h**), while the number of myeloid cells remained relatively constant (**Supp Figure 1f**). In parallel, our multiplex immunofluorescent staining also showed a concordant increase in the number of CD4+ and CD8+ cells per mm^2 of tumor section in GBM.pembro patients compared to GBM.rec patients (**Fig 1i, j**), while the number of CD14+ myelo-monocytic cells was similar (**Supp Figure 1g**). In summary, by using multiple

approaches, we showed that neo-aPD1 is associated with increased relative T cell proportion and absolute total number in the tumor microenvironment.

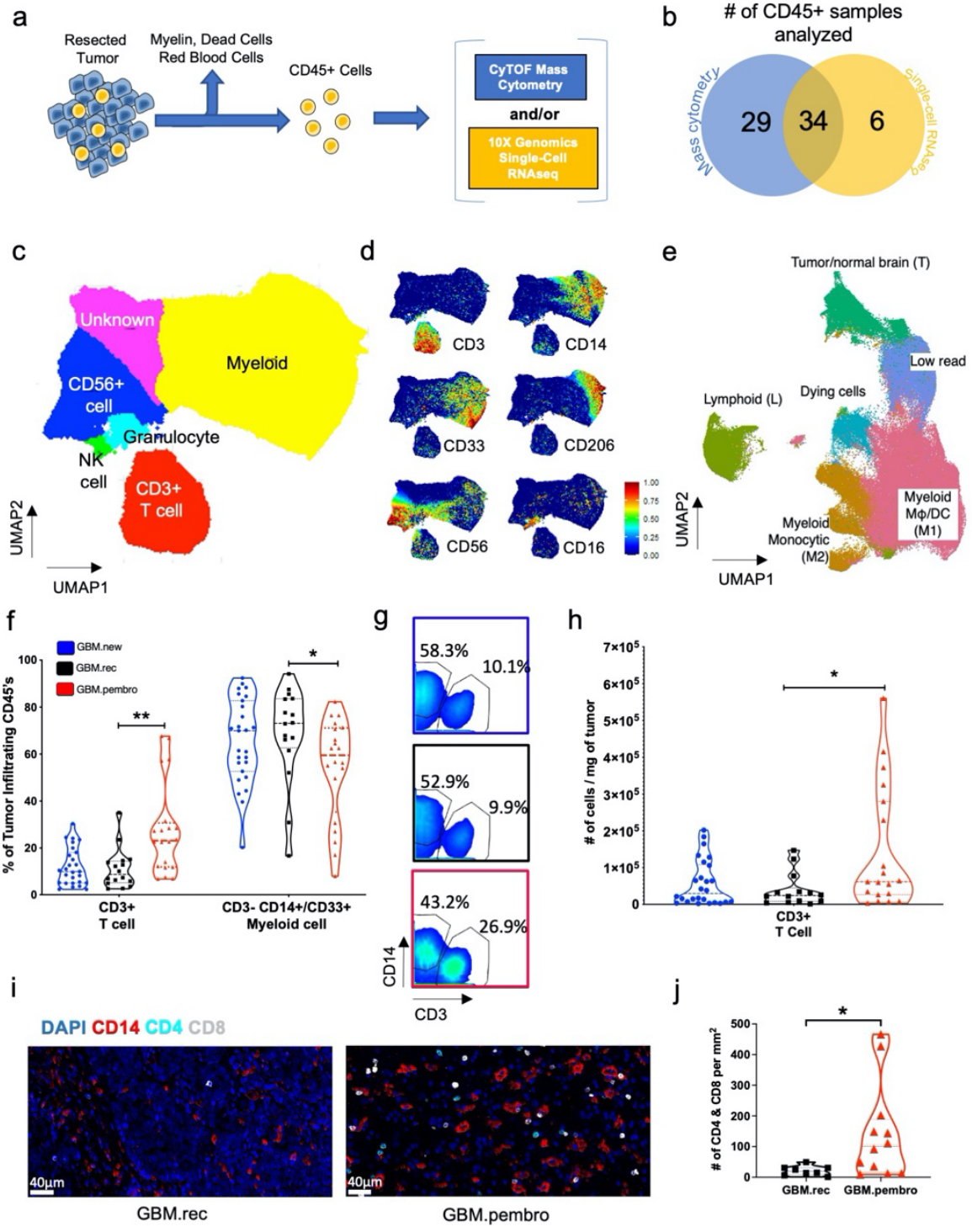

Figure 1: Neo-aPD1 increases the proportion and number of CD3+ T cells among tumor-infiltrating immune cells in recurrent glioblastoma patients.

A) Schematic of CD45+ cell isolation from tumor tissue.

B) The number of patients whose tumor-infiltrating CD45+ cells were analyzed using CyTOF and/or scRNAseq.

C) A UMAP projection of the s' CD45+ tumor-infiltrating cells analyzed with CyTOF on the common 22 marker panel (Supp. Data 1, n=1,067,057 cells from 63 total patients: 26 GBM.new, 17 GBM.rec, 20 GBM.pembro).

D) Select marker intensities on the UMAP projections of all CD45+ cells.

E) A UMAP projection of CD45+ tumor-infiltrating cells analyzed with scRNAseq (n=156,766 cells from 40 total patients: 14 GBM.new, 12 GBM.rec, and 14 GBM.pembro).

F) The percentage of tumor infiltrating CD45's within T and myeloid cell clusters from (c) across different tumor groups (blue circles: GBM.new, black squares: GBM.rec, red triangles: GBM.pembro; each dot represents a different patient).

G) CD3 and CD14 gating in the CyTOF data separated by different tumor groups. Colors are the same as (f).

H) The number of CD3+ T cells per mg of tumor across different tumor groups. The highest value for each condition was treated as outlier and removed. Colors are the same as (f).

I) Representative 20x images of multiplex immunofluorescence staining of a GBM.rec (left) and GBM.pembro (right) tumor samples (blue: DAPI, red: CD14, cyan: CD4, white: CD8). Images were collected and analyzed for 8 GBM.rec and 12 GBM.pembro patients.

J) The number of CD4+/CD8+ cells per mm^2 of tissue section for GBM.rec (black squares) and GBM.pembro (red triangles) samples.

P values were calculated using a two-sided Wilcoxon rank sum test.

Neo-aPD1 activates T cells that produce chemotactic and cytolytic factors and induced the generation of the progenitors of exhausted T cells.

Recent work in the chronic viral setting has shown that there are different stages of T cell activation and exhaustion[77-80]. To analyze the lymphoid compartment in finer detail than our CyTOF analysis and to see whether we could detect these differentially activated/exhausted T cell subsets, we increased the clustering resolution of the lymphoid cells from our initial scRNAseq clustering (n=14,322). There were 11 resulting clusters that included: four T cell clusters (effector CD8 L1: *CD8A, GZMK, CCL5*; early activated L2: *IL7R, CD40LG, CD69*; effector with progenitor phenotype L3: *TCF7, CCR7, IL7R, GZMK/B, PRF1, CTLA4, SLAMF6*; cytolytic T cluster L5: *XCL1/2*, *GZMA/B, KLRB1, PRF1)*, one T_{reg} cluster (L4: *FOXP3, CTLA4),* one cluster of proliferating lymphoid cells (L6: *MKI67*, *CDK1*), one pDC and B cell cluster (L7: *CD79A, LILRA4*), three clusters with both lymphoid and myeloid signatures (L+M1-3: *CD14, CD68, C1QA, TREM2, GPNMB*), and one cluster of dying/stressed lymphoid cells (D: *NEAT1*) (**Fig 2a, Supp. Figure 2a, Supp. Data 3**).

Among the T cells clusters (L1-5), there was an increased proportion of *GZMK*+ *CCL5*+ *CD8*+ T cell (L1), T_{reg} population (L4), and a smaller increase in the progenitor-like effector cells (L3) (**Supp. Figure 2b, Supp. Data 3**). Of note, genes and gene sets related to IFN-γ activation (*STAT1*, *IRF1*, *CXCL9* and *GBP4*) and T cell activation and exhaustion (*CXCL13, ICOS*, *CTLA4*, *PDCD1*, *TOX*, *BATF*, *LAG3*, *TIGIT*, *CD226, SLAMF6*) were significantly upregulated in response to neo-aPD1 (**Fig 2b, Supp. Figure 2c**), likely driven by the overall increase of *IFNG* expression in the GBM.pembro samples (**Fig 2c**). The overall increase in *IFNG* levels also correlated with the enrichment of the interferon downstream genes in the lymphoid cells, indicating an actual activation of the interferon pathway (**Supp. Figure 2d**). Protein levels of *ICOS*, *TIGIT*, and *TNFRSF9*, which were covered in our expanded 34 marker CyTOF panel

(applied on a subset of 35 patients from our previous CyTOF analysis; 14 GBM.new, 7 GBM.rec, 14 GBM.pembro; n=565,654 cells, **Supp. Data 1**), also showed a trend towards increased surface expression upon neo-aPD1 treatment (**Supp. Figure 2e, f, Supp. Data 1**).

Next, we performed a pseudotime trajectory analysis using Monocle 2[82] on CD4 and CD8 T cells from the four T cell clusters: L1, L2, L3, and L5 (cluster L6 of proliferating T cells was excluded because it was dominated by cell cycle genes). In the CD4 T cell compartment (**Fig 2d, e**), neo-aPD1 significantly increased the proportion of proliferating, intermediate-exhausted Th1 T cells (Th1 exh: *TCF7, CCR7, BACH2, TBX21, IFNG, STAT1, IRF1, MKI67, TOX, ENTPD1*) compared to GBM.rec. There was also a smaller increase (≥ 1.5 fold) in the early effector CD4 population (Th0 Ac: *CD69, CCL5*) and the IFNγ-activated, cytotoxic Th17-like population (Th17 m1: *RORC, GZMB, STAT1, IRF1, CXCL9*), also showing the expression of progenitor gene markers (*TCF7, CCR7, IL7R*).

In the CD8 T cell compartment (**Fig 2f, g, Supp. Data 3**), neo-aPD1 increased the proportion of IFNγ-activated, progenitor exhausted T cells. This population upregulated both cell cycle and cytolytic genes (Exh-prog: *TCF7, CCR7, IL7R, BACH2, GZMB, PRF1, CXCL9, STAT1, IRF1, MKI67, TBX21, SLAMF6*). Phenotypically, this proliferating and cytolytic *TCF7*+ population also expressed *SLAMF6*, closely matching the Tex^{prog2} and Tex^{int} populations of early progenitor of exhausted T cells recently described by Beltra et al[78]. Correlating the fates back to the Seurat's L1-L5 clusters, we noted that the CD8 T cells in this fate were dominated by those from the L3 cluster (**Supp. Figure 2g**), indicating that the majority of the L3 T cells are in this progenitor exhausted T cell state.

Interestingly, the three *GZMK*+ effector subsets (Eff 4, 5, and 6, dominated by L1 and L5 in the Seurat analysis) expressed *KLRB1* and *XCL1*. This is consistent with the recent findings on glioma-infiltrating T cells[83]. Among these three subsets, Eff 5 and 6 expressed high *PDCD1* and *CCL5*, compared to Eff 4. Eff 6, whose proportion was induced by neo-aPD1, specifically expressed high levels of *HAVCR2* and *IFNG*, implying activated, antigen-specific CD8+ T cells. Reassuringly, the levels of *CCL5* increased in the lymphoid cells and both *CCL5* and *XCL1* were higher after neo-aPD1 when we look across the total cells (**Fig 2h**). XCL1 and CCL5, in particular, are factors that have been reported to attract dendritic cells into the tumor microenvironment[84] or during viral infection[85].

In all, neo-aPD1 treatment induced the expansion and proliferation of a progenitor-like, exhausted T cell population upregulating IFN-γ, T-bet, and cytolytic markers, indicating that they may be the tumor antigen specific T cells. Additionally, neo-aPD1 also induced populations of effector T cells that upregulate the secretion of chemotactic factors associated with DC recruitment.

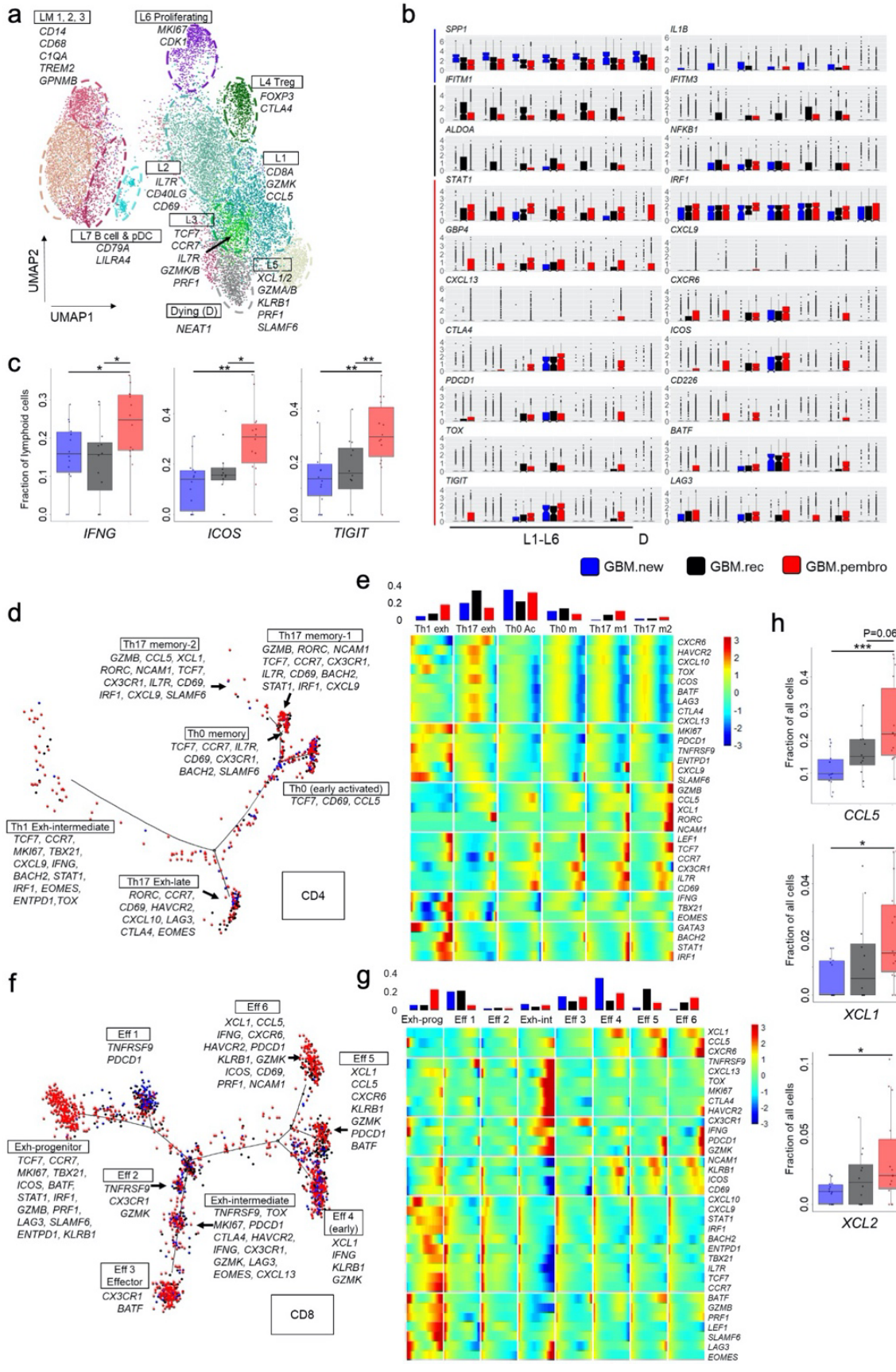
a
LM 1, 2, 3
CD14
CD68
C1QA
TREM2
GPNMB
L6 Proliferating
MKI67
CDK1
L4 Treg
FOXP3
CTLA4
L1
CD8A
GZMK
CCL5
L2
IL7R
CD40LG
CD69
L3
TCF7
CCR7
IL7R
GZMK/B
PRF1
L5
XCL1/2
GZMA/B
KLRB1
PRF1
SLAMF6
L7 B cell & pDC
CD79A
LILRA4
Dying (D)
NEAT1
UMAP2
UMAP1
b
SPP1
IL1B
IFITM1
IFITM3
ALDOA
NFKB1
STAT1
IRF1
GBP4
CXCL9
CXCL13
CXCR6
CTLA4
ICOS
PDCD1
CD226
TOX
BATF
TIGIT
LAG3
L1-L6
D
GBM.new
GBM.rec
GBM.pembro
c
Fraction of lymphoid cells
IFNG
ICOS
TIGIT
d
Th17 memory-2
GZMB, CCL5, XCL1, RORC, NCAM1, TCF7, CX3CR1, IL7R, CD69, IRF1, CXCL9, SLAMF6
Th17 memory-1
GZMB, RORC, NCAM1 TCF7, CCR7, CX3CR1, IL7R, CD69, BACH2, STAT1, IRF1, CXCL9
Th0 memory
TCF7, CCR7, IL7R, CD69, CX3CR1, BACH2, SLAMF6
Th0 (early activated)
TCF7, CD69, CCL5
Th1 Exh-intermediate
TCF7, CCR7, MKI67, TBX21, CXCL9, IFNG, BACH2, STAT1, IRF1, EOMES, ENTPD1,TOX
Th17 Exh-late
RORC, CCR7, CD69, HAVCR2, CXCL10, LAG3, CTLA4, EOMES
CD4
e
Th1 exh
Th17 exh
Th0 Ac
Th0 m
Th17 m1
Th17 m2
CXCR6
HAVCR2
CXCL10
TOX
ICOS
BATF
LAG3
CTLA4
CXCL13
MKI67
PDCD1
TNFRSF9
ENTPD1
CXCL9
SLAMF6
GZMB
CCL5
XCL1
RORC
NCAM1
LEF1
TCF7
CCR7
CX3CR1
IL7R
CD69
IFNG
TBX21
EOMES
GATA3
BACH2
STAT1
IRF1
f
Eff 1
TNFRSF9
PDCD1
Eff 6
XCL1, CCL5, IFNG, CXCR6, HAVCR2, PDCD1 KLRB1, GZMK ICOS, CD69, PRF1, NCAM1
Eff 5
XCL1
CCL5
CXCR6
KLRB1
GZMK
PDCD1
BATF
Exh-progenitor
TCF7, CCR7, MKI67, TBX21, ICOS, BATF, STAT1, IRF1, GZMB, PRF1, LAG3, SLAMF6, ENTPD1, KLRB1
Eff 2
TNFRSF9
CX3CR1
GZMK
Exh-intermediate
TNFRSF9, TOX MKI67, PDCD1 CTLA4, HAVCR2, IFNG, CX3CR1, GZMK, LAG3, EOMES, CXCL13
Eff 4 (early)
XCL1
IFNG
KLRB1
GZMK
Eff 3 Effector
CX3CR1
BATF
CD8
g
Exh-prog
Eff 1
Eff 2
Exh-int
Eff 3
Eff 4
Eff 5
Eff 6
XCL1
CCL5
CXCR6
TNFRSF9
CXCL13
TOX
MKI67
CTLA4
HAVCR2
CX3CR1
IFNG
PDCD1
GZMK
NCAM1
KLRB1
ICOS
CD69
CXCL10
CXCL9
STAT1
IRF1
BACH2
ENTPD1
TBX21
IL7R
TCF7
CCR7
BATF
GZMB
PRF1
LEF1
SLAMF6
LAG3
EOMES
h
P=0.06
Fraction of all cells
CCL5
XCL1
XCL2

Figure 2: Single-cell RNAseq analysis of intratumoral T cells shows transcriptional changes with neo-aPD1 therapy.

A) A UMAP projection of the lymphoid compartment of the tumor samples analyzed using scRNAseq (n=14,322 cells from 40 total patients: 14 GBM.new, 12 GBM.rec, and 14 GBM.pembro).

B) Differentially expressed genes in GBM.new (blue), GBM.rec (black), and GBM.pembro (red) patient samples as computed by Seurat.

C) The fraction of lymphoid cells with detected expression of the indicated genes.

D, F) Pseudotime projection of CD4 (d) and CD8 (f) T cells by Monocle 2.

E, G) The expression of CD4 (e) and CD8 (g) T cell marker genes across the different cell fates in (d) and (f), respectively. (top) Proportion of the cells from in each fate, separated by tumor groups, are shown.

H) The percentage of all lymphoid cells expressing at least one transcript for CCL5 and XCL1/2. P values were calculated using a two-sided Wilcoxon rank sum test. In all boxplots, the median is indicated by the line within the box and the 25th and 75th percentiles indicated by the lower and upper bounds of the box. The upper and lower lines above and below the boxes represent the whiskers.

TCR clone analyses demonstrates shared clones among the cytolytic T cells in the peripheral blood and intratumoral T cells.

To evaluate whether we could detect early changes in the systemic circulation with neo-aPD1, we analyzed the scRNAseq data of the PBMC samples from a subset of the GBM.rec and GBM.pembro patients. We clustered PBMC lymphoid cells (n=56,444 cells) into 15 different clusters of T cells, NK cells, and B cells (**Fig 3a, Supp. Figure 3, Supp. Data 4**). There was one cluster of lymphoid and myeloid doublets and one cluster enriched with blood platelet related mRNA. Neo-aPD1 induced an increase in the largest cluster of cytolytic T/NK cell population in the PBMC (P3) (**Fig 3b**) and significantly upregulated genes that are related to cell proliferation across all clusters (**Fig 3c, Supp. Data 4**). This indicated that neo-aPD1 induces a systemic activation and expansion of T cell clones in the periphery.

To detect the CDR3 regions of the T cells in our 3' scRNAseq data, we utilized an algorithm called TCR repertoire utilities for solid tissue (TRUST4)[86] to define distinct TCR clones by the resolved CDR3 sequences of the TCRβ chain of a T cell. We observed that the T cells with expanded clones (clone size > 1) tended to be within the early effector *GZMK*+ (L1 in the TIL and P2 in the PBMC) and cytolytic *GZMB*+ clusters (L5 in TIL and P1, P3 in PBMC) (**Fig 3d, Supp. Data 5**).

Next, we used STARTRAC analysis[87] to examine the pattern of overlaps of these major TCR clones in the different T cell clusters. In the PBMC compartment, the highest transition (normalized overlap) score was between the *GZMK*+ P2 cluster and the *GZMB/H*+ P1 cluster. Both P1 and P2 also showed a higher transition score with the cytolytic cluster P3, which suggests that both of these early effector populations in P1 and P2 may differentiate to the cytolytic, effector T cells in P3 (**Fig 3e**).

Comparing between PBMC and TIL, we observed that the TCRs of the cytotoxic TILs in L5 overlapped with PBMC's P1-4, with the strongest overlap between the cytotoxic clusters of the TIL (L5) and PBMC (P3) (**Fig 3f**). There was also an overlap between the *GZMK*+ clusters of both the TIL and PBMC (L1 and P1-2, respectively). This observation suggests that the intratumoral cytolytic T cells in L5 are populated by the PBMC's early effector CD8 T cells (P1, P2), the cytolytic T cells (P3), and the proliferating T cells (P4). Notably, a recent publication reported that peripheral expansion of certain T cell clonotypes correlates with the infiltration of those clonotypes into the tumor[88]. In the TIL compartment, the highest transition score was observed between the L3 and L5 clusters, suggesting a transition from a cytolytic, effector phenotype to a progenitor exhausted phenotype (**Fig 3g**), which was enriched after neo-aPD1.

The observation of higher clonal frequencies of the cytolytic T cells within the tumor (*GZMB+, PRF1*+ and *KLRB1*+) was reported recently by Matthewson et al[83], and our results highlight the systemic source of such cytolytic T cells and how neo-aPD1 enhances its clonal expansion. Most of the expanded cytolytic T cell clones in the PBMC probably involves existing large clones that recognize pathogens, of which some may be cross reactive to tumor antigens[89]. Meanwhile, the progenitor exhausted T cells in L3 only showed clonal overlaps with those in intratumoral cytolytic T cells in L5 but not with any of the clusters in the PBMC. This implies that the T cell clones in L3 were present at much lower clonal frequencies in the PBMC (below the detection level of TRUST4) and that they subsequently became activated and then clonally expanded only after their encounter with tumor antigens.

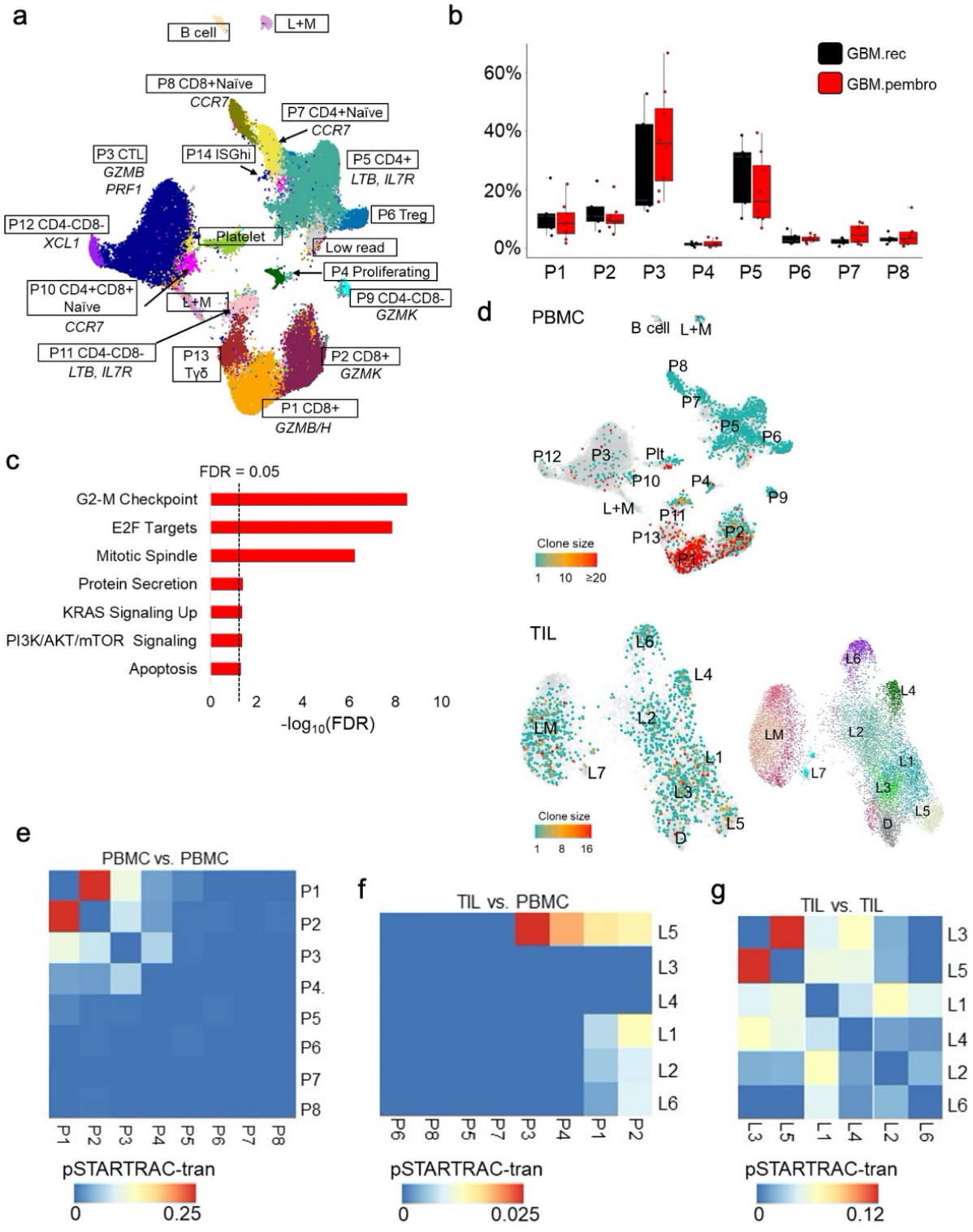

Figure 3: The phenotype and clonal distribution of intratumoral vs. peripheral T cells in recurrent glioblastoma patients.

A) A UMAP projection of the lymphoid compartment of the peripheral blood of recurrent GBM patients analyzed using scRNAseq (n=56,444 cells from 5 GBM.rec and 8 GBM.pembro patients and from 2 healthy donor controls).

B) The proportions of each lymphoid clusters in (a) in GBM.rec (black) and GBM.pembro (red) samples.

C) MSigDB Hallmark genesets showing significant overlap with the union of genes upregulated in the GBM.pembro group's PBMC (FDR values, two-sided fisher exact test).

D) T cell clone sizes as estimated by the TCRβ clones detected in the PBMCs (top) and TILs (bottom) using TRUST4.

E, F, G) Heatmaps showing the STARTRAC analysis of the shared TCRs among the PBMC clusters (e), across the PBMC and TIL clusters (f) and among the TIL clusters (g). Shared clones across two clusters indicates potential transition from one cluster to the other (non-directional). The higher the fraction of the shared TCR, the more likely that the T cells in the two clusters transition from one to the other.

In all boxplots, the median is indicated by the line within the box and the 25th and 75th percentiles indicated by the lower and upper bounds of the box. The upper and lower lines above and below the boxes represent the whiskers. The gene set enrichment P values were calculated using two-sided Fisher exact test with FDR adjustment for multiple comparisons.

Neo-aPD1 changes the composition and transcriptional profile of myelo-monocytic cells, leading to increased T cell trafficking and immunosuppressive activity.

Because our previous published work indicated that neo-aPD1 led to an increased T cell and interferon signature, we interrogated whether this interferon signature may affect the proportion or function of other non-lymphoid immune populations.

Our scRNAseq sub-clustering of the myeloid cells (n=72,492 cells) revealed 11 clusters that included: six macrophage clusters (Mϕ1: *IL1B, CCL3/4*; Mϕ2: *CXCR4, MHC II*; Mϕ3: *CXCL10, MHC II*; Mϕ4: HSP high, Mϕ5: *TMEM119*, *ADORA3*, microglia-enriched, Mϕ6: *GPNMB, CSTB*; and Mϕ7: *MRC1, ANGPTL4*), one monocyte cluster (M: *FCN1,VCAN, S100A8/9*), one DC cluster (DC: *FCER1A, MHC II*), one cluster with both lymphoid and myeloid signatures (L+M: *CD3D*), and one proliferating myeloid cell cluster (P: *MKI67*, *CDK1*) (**Fig 4a, b, Supp. Data 6**).

Mϕ1-5 populations were very similar where Mϕ1 showed a higher expression of macrophage and monocyte inflammatory factors *CCL3*, *CCL4, IL1B,* and *CXCL8*, Mϕ2 showed higher expression of *CXCR4* and *MHCII* transcripts, Mϕ3 had increased interferon stimulated genes (ISGs), Mϕ4 showed higher proportion of heat shock proteins (HSPs) and Mϕ5 showed higher expression of microglial marker *TMEM119*, *GPR34,* and *CX3CR1*[90] (**Fig 4b, Supp. Data 6**). In fact, Mϕ1-5 showed expression of *TMEM119* while clusters Mϕ6-7 and the proliferating myeloid cells did not. This is in line with recent reports highlighting two potential lineages of TAMs in glioblastoma, one that is microglia-derived and one from bone marrow-derived monocytic TAMs[76].

The largest microglia-derived TAM population is Mϕ1, which was marked by higher expression of macrophage inflammatory cytokine *IL1B,* whose high expression were related to worsened survival in recurrent GBM[76]. The fraction of this cluster did not significantly change with neo-aPD1 therapy, which suggests that this population could be targeted to improve recurrent GBM patient survival. On the other hand, the proportions of the *CXCR4*+ Mϕ2 and ISG-high Mϕ3, both of which were *MRC1*- and *MHC II*+*,* were significantly increased in proportion in GBM.pembro compared to GBM.rec (**Fig 4c**). When we analyzed the myeloid cells from our CyTOF analysis of the expanded 34 marker set (n=334,530 myeloid cells), we also observed an increased proportion of clusters c2, which is CD14+ CD11b/c+ HLA-DR+ macrophage/monocytic population (**Supp. Figure 4a-c**). Of note, the ablation of *CXCR4*+ myeloid population was reported to suppress melanoma and glioblastoma growth in preclinical models[91,92], which implies that Mϕ2 is an immunosuppressive population induced by neo-aPD1.

The observation of increased Mϕ2 and ISG-high Mϕ3 was confirmed by the general upregulation of genes associated with the IFN-γ pathway, such as *STAT1*, *IRF1*, *GBP4*, *TAP1, HLA-DQA1,* and *CXCL9/10* (**Fig 4d, e, Supp. Data 6**). These changes were most pronounced in the ISG-high Mϕ3 cluster. We noted that the expression of *CXCL9* and *CXCL10* has been previously found to be involved in increasing T cell trafficking into solid tumors and involved with immunotherapy efficacy[93]. The cells in the GBM.pembro group also showed increased expression of several macrophage inflammatory genes such as: *NLRP3*, *CH25H*, *CCL3/4,* and, *CXCR4*.

In the CyTOF data analysis, we found a significant increase of CD274 (PD-L1) median expression and a concomitant increase in the percentage of PD-L1+ myeloid cells in the GBM.pembro group (**Supp. Figure 4d, e, Supp. Data 7**); the increased PD-L1 expression may

be induced by the increased IFN-γ associated with neo-aPD1. Of note, we observed that CD274 was most significantly increased by neo-aPD1 in the CD206+ monocytic/macrophage cluster 1, which is likely a mature macrophage population with immunosuppressive properties (**Supp. Figure 4d**). The same trend of increased C*D274* transcript was observed in the scRNAseq data both in the whole myeloid fraction and in the *CD206*/*MRC1*+ Mϕ7 cluster (**Supp. Figure 4f**).

Looking at the monocyte and proliferating myeloid populations, we noted a similar increase of *STAT1*, *IRF1*, *MHC II*, *CXCL9/10* as a result of neo-aPD1 treatment (**Supp. Fig 5a**). We further analyzed the monocyte population (cluster M) by increasing the clustering resolution. Two subclusters of monocytes were identified: one classical monocyte cluster (Mono 1: *FCN1*, *SELL*, *S100A8/9*) and one non-classical monocyte (Mono 2: *LILRB2*, *CD48*, *ITGAL*)[64]. We noted a number of subclusters that nicely overlapped the macrophage populations, indicating that they arose from the differentiation of the monocytes (**Supp. Fig 5b, Supp. Data 8**).

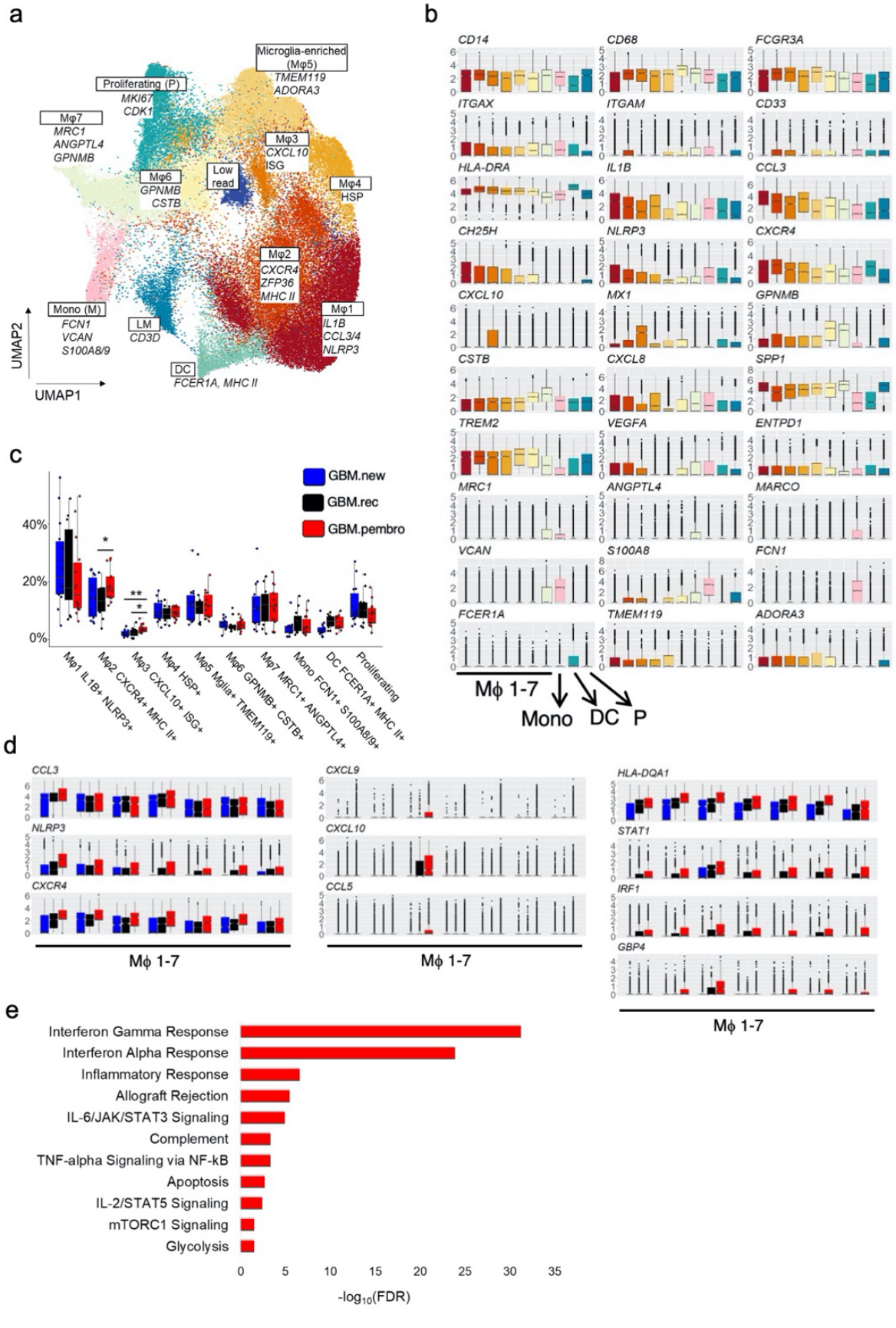
a
Microglia-enriched (Mφ5)
TMEM119
ADORA3
Proliferating (P)
MKI67
CDK1
Mφ7
MRC1
ANGPTL4
GPNMB
Mφ3
CXCL10
ISG
Low read
Mφ6
GPNMB
CSTB
Mφ4
HSP
Mφ2
CXCR4
ZFP36
MHC II
Mono (M)
FCN1
VCAN
S100A8/9
LM
CD3D
Mφ1
IL1B
CCL3/4
NLRP3
DC
FCER1A, MHC II
UMAP2
UMAP1
b
CD14
CD68
FCGR3A
ITGAX
ITGAM
CD33
HLA-DRA
IL1B
CCL3
CH25H
NLRP3
CXCR4
CXCL10
MX1
GPNMB
CSTB
CXCL8
SPP1
TREM2
VEGFA
ENTPD1
MRC1
ANGPTL4
MARCO
VCAN
S100A8
FCN1
FCER1A
TMEM119
ADORA3
Mφ 1-7
Mono
DC
P
c
GBM.new
GBM.rec
GBM.pembro
40%
20%
0%
Mφ1 IL1B+ NLRP3+
Mφ2 CXCR4+ MHC II+
Mφ3 CXCL10+ ISG+
Mφ4 HSP+
Mφ5 Mglia+ TMEM119+
Mφ6 GPNMB+ CSTB+
Mφ7 MRC1+ ANGPTL4+
Mono FCN1+ S100A8/9+
DC FCER1A+ MHC II+
Proliferating
d
CCL3
NLRP3
CXCR4
CXCL9
CXCL10
CCL5
HLA-DQA1
STAT1
IRF1
GBP4
Mφ 1-7
Mφ 1-7
Mφ 1-7
e
Interferon Gamma Response
Interferon Alpha Response
Inflammatory Response
Allograft Rejection
IL-6/JAK/STAT3 Signaling
Complement
TNF-alpha Signaling via NF-kB
Apoptosis
IL-2/STAT5 Signaling
mTORC1 Signaling
Glycolysis
0
5
10
15
20
25
30
35
-log10(FDR)

Figure 4: Neo-aPD1 induces multiple immunosuppressive TAMs and monocyte populations

A) A UMAP projection of the myeloid compartment of the 40 patient samples analyzed using scRNAseq (n=72,492 cells from 40 total patients: 14 GBM.new, 12 GBM.rec, and 14 GBM.pembro).

B) The expression levels of various marker genes of each cluster in (a)

C) The proportion of the myeloid cells in each cluster across multiple tumor groups (blue: GBM.new, black: GBM.rec, red: GBM.pembro).

D) Differentially upregulated genes in GBM.pembro samples across the macrophage clusters. Colors the same as (c).

E) MSigDB Hallmark genesets showing significant overlap with the union of the genes upregulated in the GBM.pembro group across all myeloid clusters (FDR values, two-sided fisher exact test).

P values were calculated using a two-sided Wilcoxon rank sum test unless otherwise noted. In all boxplots, the median is indicated by the line within the box and the 25th and 75th percentiles indicated by the lower and upper bounds of the box. The upper and lower lines above and below the boxes represent the whiskers. The gene set enrichment P values were calculated using two-sided Fisher exact test with FDR adjustment for multiple comparisons.

Neo-aPD1 therapy increases the proportion of interferon activated DC populations and the proportion of CCR7+ LAMP3+ XCR1+ DCs in the tumor

From our myeloid subclustering analysis, we noticed that there was a DC cluster; thus, we looked at the composition of the cDC populations in more detail. We further clustered our DC population (n=2,960) from our scRNAseq analysis and generated 9 subclusters (**Fig 5a, b, Supp. Data 9**): 1 cDC2 cluster (cDC2: *CD1C, FCER1A, CLEC10A*), 1 cDC1 cluster (*XCR1, CLEC9A, BATF3, IRF8*), 1 activated and/or migratory DC cluster (mDC: *CCR7, LAMP3, CD80*; similar to a population recently described[76]), and 4 clusters that were monocyte-like (mo-DC1: *CD14, CD1c, FCER1A, CLEC10a*; mo-DC2: *CD14*, *C1QA, CD141*; mo-DC3: *CD14, C1QA, IL1B* ; mo-DC4: *CD14*, *C1QA*, *CLEC10A*), 1 cluster with cells with low reads, and 1 cluster with cells that had high expression HSP transcripts.

There were no significant differences in the proportion of cells between the different conditions in any of the DC sub-clusters (**Supp. Figure 6a**). However, when we examined the gene expression changes in the different DC subclusters, we noticed several significant and immunologically relevant alterations. Neo-aPD1 was associated with an overall induction of ISGs such as *STAT1, IRF1, GBP4,* and *TAP1* in multiple DC subsets (**Fig 5c**). In the cDC1 population, neo-aPD1 was associated with increased expression of *XCR1*. We posit that these cDC1 cells may be attracted by the *CCL5* and *XCL1* expressing CD8+ T cells (**Fig 2a, Fig 2g**). In mDC cells, neo-aPD1 was associated with increased expression of the DC activation and T cell trafficking chemokine genes: *CD40*, *CXCL9/10*, and *IL-32*. At the same time, neo-aPD1 also induced the expression of activation-induced, negative feedback DC genes such as *IDO1* and *PD-L1/L2.*

Importantly, we also observed a significantly increased DC expression of *XCL1/2*, *CXCL9/10, CXCR3,* and *CCL5* with neo-aPD1 (**Supp. Figure 6b**). Because these genes are associated with DC and T cell trafficking, this may indicate that neo-aPD1 results in additional recruitment of T cells and DCs by the intratumoral DCs. On the other hand, the DCs in the GBM.new samples showed higher expression of monocytic genes (*CD14, CXCL8*) and GBM.rec cells showed upregulation of genes related to the type I IFN (*IFI6, IFI27*) and NFκB (*NFKB1*) pathways (**Supp. Figure 6c**), indicating a generally less activated DC population[94].

To examine the different transcriptional states in the DC populations, we further analyzed the DC cells using Monocle 2. Our pseudotime trajectory analysis yielded 9 distinct DC fates (**Fig 5d, e**). Interestingly, we observed three separate *CCR7*+ mDC populations: mDC with cDC1 characteristics (Migratory cDC1: *XCR1, CLEC9A*, *BATF3, XCR1, LAMP3*), one with a mixed moDC and/or cDC2 characteristics (Migratory cDC-2/moDC: *CD1C, CLEC10A, FCER1A, TREM1*, *S100A4/6/9*) and one *VEGFA*+ cDC2-like mDC (Migratory cDC2-2: *CLEC10A*, *FCER1A, VEGFA, NLRP3, CD39/ENTPD1*). Notably, only the first two migratory DC populations (Migratory cDC1 and Migratory cDC-2/moDC) were induced (≥ 1.5-fold) by neo-aPD1 treatment. Conversely, neo-aPD1 also reduced the fractions of monocyte- and macrophage-like DC populations that were enriched in the GBM.new and GBM.rec tumors. These populations expressed high levels of known immunosuppressive myeloid markers like *MRC1*, *TREM2,* and *GPNMB* and T cell suppressive genes such as *VEGFA*, *IL10,* and *ENTPD1*.

Despite these increases in proportion of IFN-γ activated, migratory DCs with neo-aPD1, the overall proportion of the neo-aPD1 activated DCs among all cells remained relatively small (the total number of DC were 2,960 out of 72,492 analyzed myeloid cells). Such limited number of activated DC likely leads to suboptimal antigen presentation within the tumor which results in

inadequate antitumor activities by T cells. This implies that one potential way to achieve a longer lasting response to neo-aPD1 may be to further boost intratumoral DC activation or trafficking.

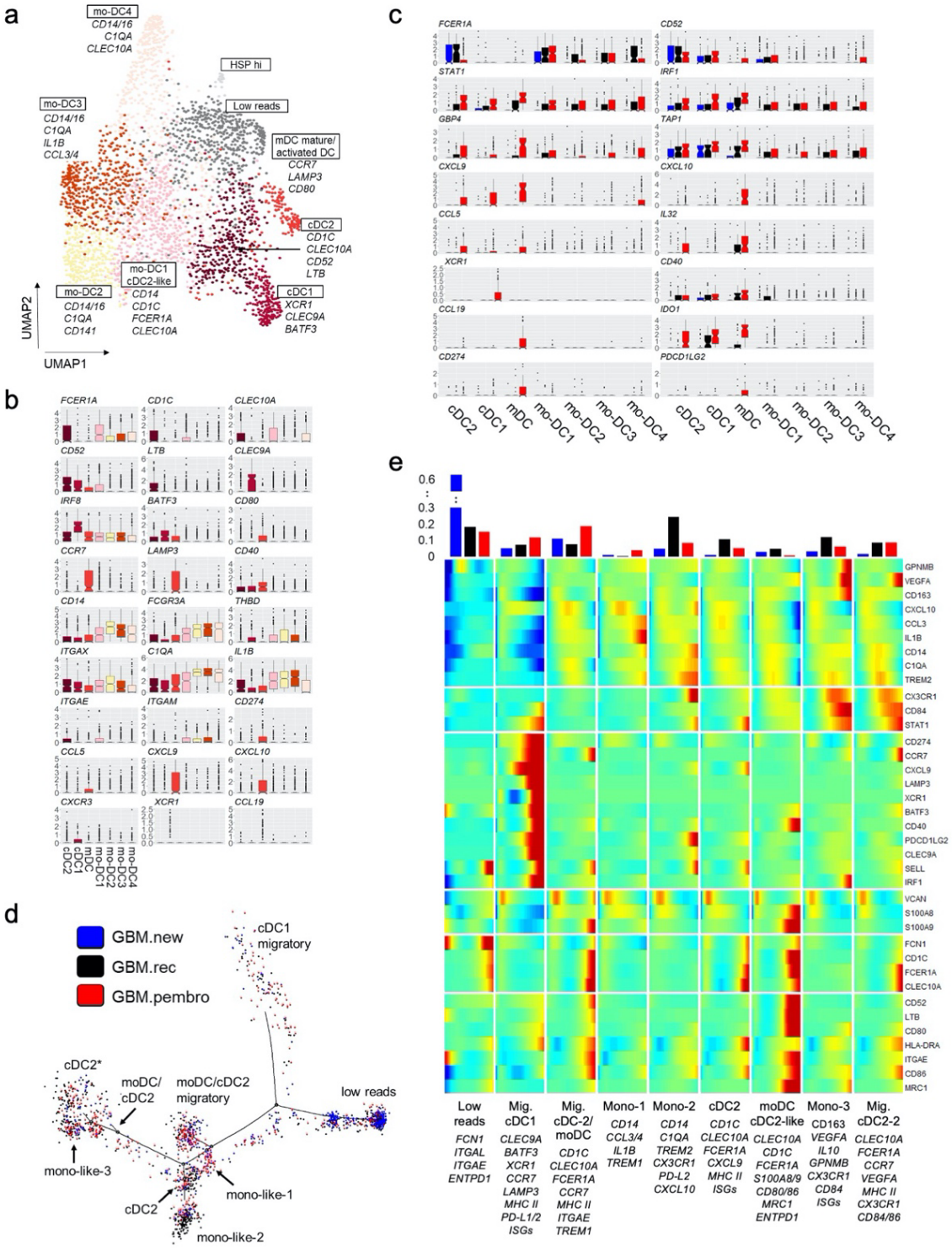

Figure 5: Neo-aPD1 therapy increases the proportion of intratumoral migratory DCs

A) A UMAP projection of the DC compartment analyzed using scRNAseq (n=2,960 cells from 40 total patients: 14 GBM.new, 12 GBM.rec, and 14 GBM.pembro).

B) The normalized expression of the marker genes of different DC clusters.

C) Differentially upregulated genes in GBM.pembro samples in one or more DC clusters (blue: GBM.new, black: GBM.rec, red: GBM.pembro).

D) Pseudotime projection of all DCs as analyzed by Monocle 2. Colors are as in (c).

E) Heatmap showing the expression of DC/monocyte marker genes in each DC fate as defined in (d). (top) The proportion of DCs from each tumor groups in each fate.

In all boxplots, the median is indicated by the line within the box and the 25th and 75th percentiles indicated by the lower and upper bounds of the box. The upper and lower lines above and below the boxes represent the whiskers.

Neo-aPD1 therapy potentiates the engagement of additional immune checkpoints.

Given the transcriptomic changes in genes encoding receptor-ligand pairs in response to neo-aPD1, we performed an unbiased cell-cell interaction inference analysis across all immune cell types using CellChat[95]. We included all annotated populations we had in the lymphoid (L1-L7), macrophage (Mϕ1-7 and P), DC (cDC1-2, mDC, moDC1-4), and the monocyte populations (Mono1-2, Mϕ-like1-4).

Immune cells from GBM.pembro patients had the greatest number of all possible inferred interactions. Both GBM.rec and GBM.pembro showed a similar average interaction strength, which assesses the probability of observing an interaction given the expression levels of the receptor and its ligand (**Fig 6a**). Next, we calculated the signaling pathways with the highest combined interaction strength ratio between GBM.pembro and GBM.rec. The pathways enriched in GBM.pembro included: TIGIT:CD226:NECTIN2, CD86:CTLA4, PDCD1:PD-L1/L2, Type II IFN (IFN-γ), CXCL:CXCR, XCR:XCL, and CCR:CCL (**Fig 6b**). Notably, these were genes that we had previously seen relative increases in transcriptional levels following neo-aPD1. On the other hand, neo-aPD1 decreased the signaling pathways *VEGF* and *ANGPTL*, which are known wound healing and angiogenic processes correlated with worse survival in GBM[96,97].

We next examined the signaling probability of all receptor-ligand interactions found in our previously identified cell clusters (**Fig 6c**). The majority of cellular interactions were dominated by the macrophage populations and tended to remain stable across GBM.new, GBM.rec and GBM.pembro patient samples. Of note, the number of possible pathway interactions involving the T/NK clusters were higher in GBM.pembro compared to GBM.rec. We also noted increased

interaction strength between *CXCL9/10/11* and *CXCR3*+ T/NK cells in the GBM.pembro compared to only *CXCL10-CXCR3* in GBM.rec (**Fig 6d**). Furthermore, neo-aPD1 induced the recruitment of *CCR5*+ T cells potentially by the overexpression of *CCL3/4* (Mϕ1-4) and/or *CCL5* (L1, 3, 5) (**Supp. Figure 7a**). *CCR5* expression by both CD4+ and CD8+ T cells was reported to be crucial in boosting anti-tumor responses by optimizing helper-dependent CD8+ T cell priming at immunological synapse[98,99]. CellChat also highlighted GBM.pembro specific chemokine receptor-ligand interactions between *XCR1* (cDC1) and *XCL1/2* (mainly expressed by the cytotoxic L5) which were not observed at all by immune cells from the other patients (**Fig 6e, f**). The interaction hints at the recruitment of cDC1 by the intratumoral cytotoxic T cells.

We noted the possible engagement of two different immune checkpoint pathways: the CTLA-4 and TIGIT pathways. Specifically, GBM.pembro samples showed increased potential interactions between *CD86/CD80* and *CTLA4* and *CD28*. *CD86* was expressed by all myeloid cell clusters where the larger clusters contributed to higher interaction strength (thicker lines, **Fig 6g**). At the same time, the other binding partner of *CD28* and *CTLA4*, *CD80*, was also expressed higher in recurrent GBM samples regardless of neo-aPD1 (**Supp. Figure 7b**). In GBM.new and GBM.rec, myeloid-expressed *CD86* and *CD80* were expected to mostly interact with the constitutively expressed *CTLA4* on T_{reg} (L4) (**Fig 6g, Supp. Figure 7b**). However, in GBM.pembro, both *CTLA4* and *CD28* were induced also on the progenitor exhausted-enriched CD8+ T cell cluster (L3) and proliferating T cell cluster (L6) (**Supp. Figure 7b**). The new induction of *CTLA4* in GBM.pembro likely suppresses T cell activity, implying that the potential use of anti-CTLA-4 antibody blockade may enhance the co-stimulatory signaling through *CD80/86*'s engagement of T cells' *CD28*[100], which was also overexpressed in GBM.pembro patients.

Another immune checkpoint interaction that was higher in the GBM.pembro group was between the ligands *CD226* and *TIGIT* and their receptor *Nectin2*[101,102] (**Fig 6h, Supp. Figure 7c**). In both GBM.rec and GBM.pembro, *CD226* and *TIGIT* also interacted with the poliovirus receptor (PVR) (**Supp. Figure 7c**). Just like *CTLA4* and *CD28*, *TIGIT* and *CD226* are T cell co-inhibitory and co-stimulatory receptors, respectively[103,104]. In all three conditions, interactions between *TIGIT* and *Nectin2* remained intact, but GBM.pembro showed new interactions involving *TIGIT*+ L1 and L2 clusters. Moreover, neo-aPD1 significantly increased interactions between *Nectin2*+ myeloid clusters with *CD226*+ L2, L3, and L6 lymphoid clusters whereas this interaction was absent in GBM.new and GBM.rec (**Fig 6h, Supp. Figure 7c**). Importantly, the presence of *CD226*+ CD8+ T cells has been shown to be a pre-requisite for response to anti-TIGIT immunotherapy[105].

Together, the interactome analysis shows that neoadjuvant anti-PD-1 therapy increases the number of new immune-relevant receptor-ligand pairs and that these new interactions represent potential therapeutic axes to inhibit or augment in addition to the PD-1/PD-L1 axis.

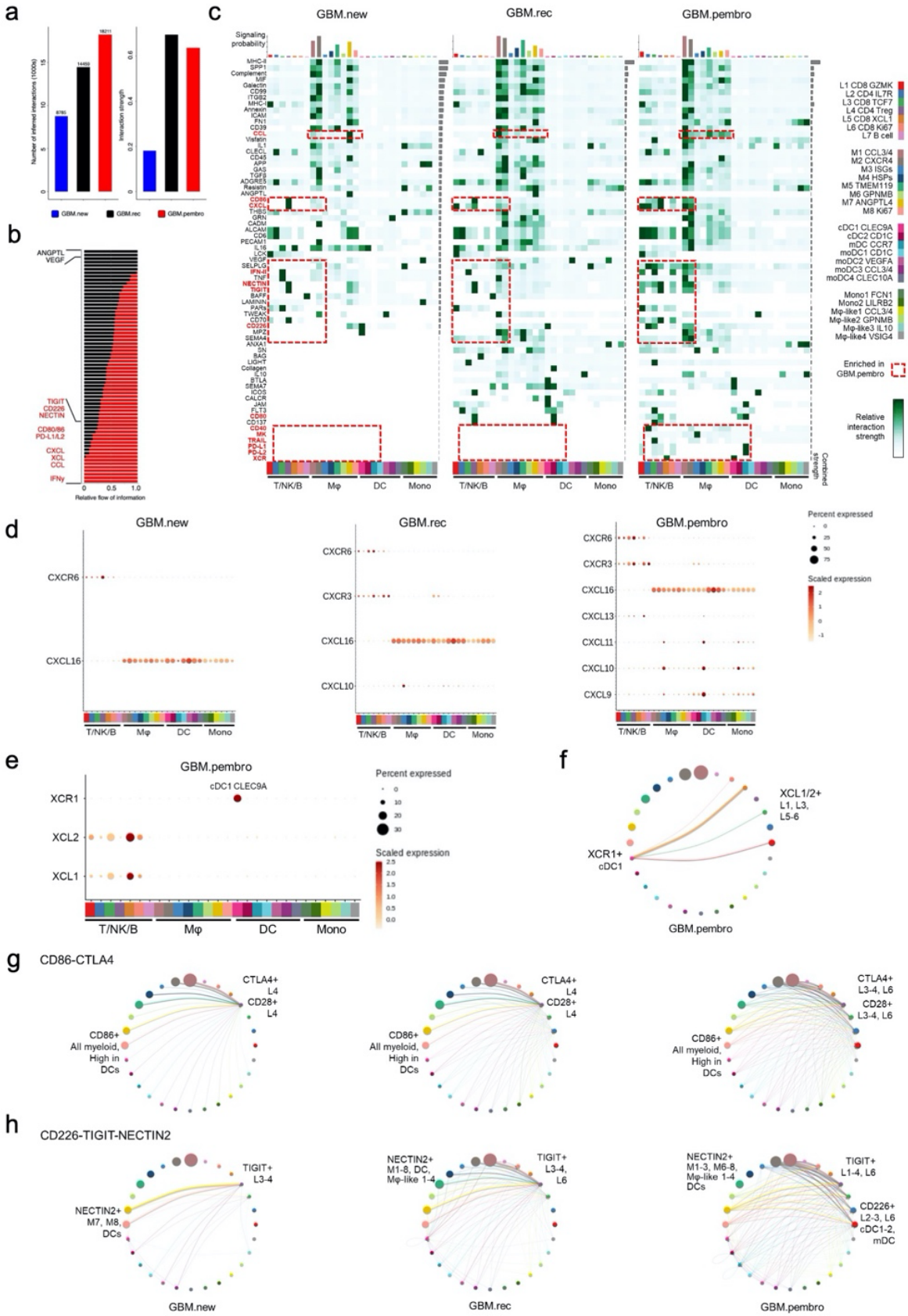
a
Number of interact ions (1000s)
Interaction strength
8786
14459
16211
GBM.new
GBM.rec
GBM.pembro
b
ANGPTL
VEGF
TIGIT
CD226
NECTIN
CD80/86
PD-L1/L2
CXCL
XCL
CCL
IFNγ
Relative flow of information
c
GBM.new
GBM.rec
GBM.pembro
Signaling probability
T/NK/B
Mφ
DC
Mono
Combined strength
L1 CD8 GZMK
L2 CD4 IL7R
L3 CD8 TCF7
L4 CD4 Treg
L5 CD8 XCL1
L6 CD8 Ki67
L7 B cell
M1 CCL3/4
M2 CXCR4
M3 ISGs
M4 HSPs
M5 TMEM119
M6 GPNMB
M7 ANGPTL4
M8 Ki67
cDC1 CLEC9A
cDC2 CD1C
mDC CCR7
moDC1 CD1C
moDC2 VEGFA
moDC3 CCL3/4
moDC4 CLEC10A
Mono1 FCN1
Mono2 LILRB2
Mφ-like1 CCL3/4
Mφ-like2 GPNMB
Mφ-like3 IL10
Mφ-like4 VSIG4
Enriched in GBM.pembro
Relative interaction strength
d
GBM.new
GBM.rec
GBM.pembro
CXCR6
CXCL16
CXCR3
CXCL10
CXCL13
CXCL11
CXCL9
Percent expressed
Scaled expression
e
GBM.pembro
cDC1 CLEC9A
XCR1
XCL2
XCL1
Percent expressed
Scaled expression
f
XCL1/2+
L1, L3,
L5-6
XCR1+
cDC1
GBM.pembro
g
CD86-CTLA4
CTLA4+
L4
CD28+
L4
CD86+
All myeloid,
High in
DCs
CTLA4+
L3-4, L6
CD28+
L3-4, L6
h
CD226-TIGIT-NECTIN2
TIGIT+
L3-4
NECTIN2+
M7, M8,
DCs
NECTIN2+
M1-8, DC,
Mφ-like 1-4
TIGIT+
L3-4,
L6
NECTIN2+
M1-3, M6-8,
Mφ-like 1-4
DCs
TIGIT+
L1-4, L6
CD226+
L2-3, L6
cDC1-2,
mDC
GBM.new
GBM.rec
GBM.pembro

Figure 6: Increased engagement of additional immune checkpoints may limit neoadjuvant anti-PD1-driven T cell activation.

A) The total absolute (left) or normalized (right) number of CellChat-inferred interactions among the population in each tumor group (blue: GBM.new, black: GBM.rec, red: GBM.pembro, n=156,766 cells from 40 total patients: 14 GBM.new, 12 GBM.rec, and 14 GBM.pembro).

B) Signaling pathways with significant differences in the overall information flow (sum of all normalized interaction) between GBM.rec and GBM.pembro.

C) The overall signaling patterns between CellChat curated pathways and our defined cell clusters. The interaction strength reflects the sum of all normalized interaction in each pathway. The top bar graph compares the sum of total interaction strength per cell type while the bar graph on the right summarize the interaction strength per pathway. Of note, myeloid cell interactions dominate the bulk of the interaction across all tumor groups.

D,E) The normalized expression of CXCL (d) and XCL pathway genes with significant expression in indicated tumor groups. The genes shown are known ligand receptor pairs (CXCL16-CXCR6, CXCL9/10/11-CXCR3 and XCL1/2-XCR1).

F) The inferred XCL1/2-XCR1 signaling network among the cell populations represented by the nodes. Color code as in (e), size of node represents the size of the population, edge width represents the pathway specific interaction strength.

G, H) Same as (f) for CD86-CTLA4-CD28 signaling (g) or CD226-TIGIT-NECTIN (h) pathways. Both T cell checkpoints were inferred to be significantly engaged after neo-aPD1.

Discussion

In this study, we utilized high-dimensional single-cell analyses coupled with unsupervised clustering and pseudotime trajectory analyses to understand the cellular characteristics and transcriptomic features of tumor-associated myeloid cells and lymphoid cells in patients with glioblastoma treated with or without neoadjuvant anti-PD-1 checkpoint blockade immunotherapy. We found that the tumor microenvironment was heavily dominated by myeloid cells, but in patients treated with neo-aPD1, there was an increase in the density of T cells within the tumor microenvironment. Single-cell RNAseq analysis showed that neo-aPD1 increased the proportion of cytotoxic T cells (P3) in peripheral blood, implying systemic T cell activation. Single-cell TCR analysis of the PBMC and TILs showed TCR overlap between tumors' and PBMC's activated/cytotoxic T cell clusters (L1 and P1-2, L5 and P1-4), which suggests that these T cells migrate from the systemic circulation to the tumor microenvironment and may underlie clonal replacement observed after neo-aPD1[106,107]. Moreover, within the tumor, we observed TCR overlap between cytotoxic T cells (L5) and a population of progenitor exhausted T cells (L3). This indicates a transition of cytotoxic effector T cells into progenitor exhausted T cells, resulting in a fractional increase of the L3/Exh-progenitor population. We are aware of the inherent limitations in TRUST4's sensitivity for TCR detection to our 3', poly-A enrichment-based RNA-seq analysis. It is likely that most of the TCR clones we detected would be from larger TCR clones. Nevertheless, the overlaps of these major clones can still suggest the direction of phenotypic transition across different T cell clusters in the periphery and TILs. Many of these tumor-infiltrating T cells highly expressed chemotactic genes, such as *CCL5* and *XCL1*, that can attract additional T cells and professional antigen presenting cells (e.g., dendritic cells) into the tumor microenvironment.

In our dendritic cell analysis, we found that neo-aPD1 was associated with increases in expression of genes related to DC trafficking and also proportions of IFN-γ activated, cross-presenting DC subsets (DC pseudotime Migratory cDC1 and Migratory cDC-2/moDC). Our interactome results also indicated that chemotactic factors produced by intratumoral T cells may be responsible for DC trafficking along the *XCL1/XCR1* axis. However, despite the increase in proportion of these migratory DC subsets, these cells remained a relatively small percentage of the whole APC populations. As such, the use of CD40 agonists to expand these activated, cross-presenting DC populations may be warranted as it was reported to result in more effective T cell priming by the DCs in a murine colorectal cancer setting[93].

In the TAM and monocyte populations, neo-aPD1 was associated with elevated expression of genes related to IFN-γ stimulation, including those related to T cell trafficking, such as *CXCL9/10*. Importantly, the receptor for *CXCL9/10, CXCR3,* is expressed by the multiple CD8+ T cell populations and our interactome analysis confirmed likely increased interactions along this axis. Importantly, neo-aPD1 also specifically increased potential interactions along the immunosuppressive *CTLA4:CD86/CD80* and *TIGIT:Nectin2/PVR* axes between myeloid and the activated T cell populations (L1, L3 and proliferating L6). The upregulation of *CTLA4* and *TIGIT* were both accompanied by the upregulation of their respective co-stimulatory molecules *CD28* and *CD226*, which strongly suggests that these T cells are primed to be activated further by blocking CTLA-4[108] and/or TIGIT[101,104]. In fact, CTLA-4 blockade was shown to elicit a stronger intracranial response in melanoma brain metastasis[109], suggesting the feasibility of testing this combination in a neoadjuvant setting for recurrent GBM. As such, we have recently started a Phase I clinical trial examining the dual treatment of neoadjuvant CTLA-4 and anti-PD-1 in the recurrent GBM setting (NCT04606316). Additionally, targeting the other neo-aPD1-induced

immune checkpoint molecule, *TIGIT*, could also be beneficial to further boost the intratumoral T cell activity.

Putting all of our findings together, we proposed the following model for how neo-aPD1 affects the immune landscape of recurrent GBM (**Supp. Figure 8**). (1) Neo-aPD1 systemically activates T cells in the periphery (P1-4) and some of these T cells migrate into the GBM tumor microenvironment. (2) The activated T cells (L1, L5) produce cytotoxic granules like Granzyme B and K and perforin, which promote tumor death, chemotactic factors like CCL5 and XCL1/2, which signal to cDCs and/or T cells in the blood to enter the tumor microenvironment, and IFN-γ, which activates these incoming cDCs. (3) The IFN-γ activated cDCs produce CXCL9/10/11 to promote additional DC and T cell trafficking into the tumor and then cross-present and activate T cells. Increased T cell activation produces more IFN-γ in the microenvironment that results in a positive loop that promotes additional immune cell infiltration. In the process, a population of tumor antigen specific T cells started to transition into a progenitor exhausted phenotype (L3, CD8+ pseudotime, Exh-progenitor). (4) The increased levels of IFN-γ also recircuits the more numerous myeloid populations resulting in some myeloid populations that produce factors, like CXCL9/10, that increase intratumoral T cell trafficking (Mϕ3). However, the majority of the myeloid populations produce IFN-γ stimulated inflammatory molecules such as IL-1ß (Mϕ1), express immunosuppressive surface markers like CXCR4 (Mϕ2) and PD-L1 (Mϕ7). Importantly, all of the TAM and monocyte populations maintained a high expression of *CD86* and *NECTIN2*, which potentially engage neo-aPD1-induced CTLA-4 and TIGIT T cell checkpoints on the activated T cell populations. This enhanced inhibitory interaction may drive the increase of the progenitor exhausted T cells and limit the magnitude and persistence of the antitumor T cell activities.

In this paper, we set out to characterize tumor infiltrating immune populations in patients with glioblastoma. Our integrated analyses have detailed the immune landscape in these malignant brain tumors at the single cell level and how this immune landscape changes with neo-aPD1 therapy. As our study did not include comparison of patient-matched pre- and post-treatment samples, we are unable to conclusively state that the anti-tumor immune effects as a direct result of neoadjuvant anti-PD-1 in each patient. However, we evaluated equally sized groups of patients at a single timepoint, which can shed light into the early effects of PD-1 blockade on the systemic and intratumoral microenvironment. Future work studying the timing of neoadjuvant anti-PD-1 administration both in the pre-clinical and clinical settings would be needed to confirm these findings. Nevertheless, for now, our data would suggest that although neo-aPD1 improves survival outcomes by increasing anti-tumor T cell responses, it is not completely curative as this T cell response is curtailed by the engagement of additional T cell checkpoints and other immunosuppressive pathways by the myeloid populations. We postulate that further efforts to increase effector T cell and DC recruitment, in combination with blocking the immunosuppressive signaling engaged by the myeloid cells, will be necessary to achieve clinically relevant effects in recurrent glioblastoma. As neoadjuvant studies progress, we hope that others will be able to contribute to this trove of information to hone our understanding of this uniformly fatal tumor.

Methods

Ethical compliance: Research conducted in this study complied with all relevant ethical regulations.

The UCLA Medical Institutional Review Board 2 (IRB#10-000655-AM-00059) approved all protocols related to patient specimen collection.

Patient tissue collection and single-cell isolation: Tumor tissue was obtained from tumors of patients who underwent surgery at the University of California, Los Angeles. All patients provided written informed consent. This study was conducted in accordance with the Declaration of Helsinki and under an institutional review board approved protocol. All GBM patients (newly diagnosed and recurrent) were treated with standard of care therapies. Patients with surgically accessible recurrent GBMs, regardless of recurrence number and who did not show response to standard of care treatment and had tumor progression, were treated with off-label, off- trial pembrolizumab 200 mg by intravenous infusion 14 ± 5 days before surgery, similar to our previously published study. Peripheral blood was drawn from patients prior to surgical resection of their tumors. Tumor tissue not needed for diagnosis was digested using the Miltenyi Brain Tumor Dissociation kit (Miltenyi Biotec, cat. 130-095-42) and gentleMACS dissociator (Miltenyi Biotec, cat. 130- 093-235) and labeled with CD45+ microbeads (Miltenyi Biotec, cat. 130-045-801). CD45+ cells were positively selected for with Miltenyi LS columns (Miltenyi Biotec, cat. 130-042-401) and MidiMACS separator (Miltenyi Biotec, cat. 130-042-302). Collected CD45+ cells were then placed in Bambanker (Fisher Scientific, cat. 302-14681) and stored in liquid nitrogen. Peripheral blood mononuclear cells were collected in CPT tubes (BD Biosciences, cat: 362753), isolated according to the manufacturer's protocol, placed in freezing media made of 90% human AB serum (Fisher Scientific, cat. MT35060CI) and 10% dimethyl sulfoxide (Sigma, cat. C6295-50ML) and stored in liquid nitrogen. Most of the patient

samples used in this study were exhausted to gather sufficient amount of data for analysis. Any remaining sample will be available from the corresponding author upon reasonable request, though the quantity may or may not be sufficient to complete all the corresponding experiments.

Time-of-flight CyTOF mass cytometry: Peripheral blood mononuclear cells and tumor-associated CD45+ cells were collected at the time of surgery as described above. On the day of data acquisition, samples were briefly thawed in a 37 °C water bath and washed in RPMI-1640 media (Gennesse Scientific, cat: 25-506) supplemented with FBS and penicillin and streptomycin. Cells were then prepared for mass cytometry analysis according to the Maxpar cell surface staining protocol. Briefly, 0.5–3 × 106 cells were washed with PBS and treated with 0.1 mg/mL of DNAse-1 Solution (StemCell Technologies, cat: 07900) for 15 minutes at room temperature. Cells were then resuspended in 5 μM Cell-ID cisplatin (Fluidigm, cat: 201064) as a live/dead marker for 5 min at room temperature. After quenching with the Maxpar cell staining buffer (Fluidigm, cat: 201068), the cells were incubated with a 24- to 34-marker panel for 30 min at room temperature (Supp. Data 1, all antibodies were stained at a 1:50 dilution). After washing with cell staining buffer, cells were incubated overnight in 125 nM iridium intercalation solution (1000X dilution of 125 μM Cell-ID Intercalator-Ir; Fluidigm, cat: 201192A) in Maxpar Fix and Perm Buffer (Fluidigm, cat: 201067) to label intracellular DNA. Cells were then washed with cell staining buffer and distilled water. Due to likely enzymatic degradation of the CD8 co-receptor (the same CD8 antibody worked on control PBMCs, data not shown), we only performed general CD3+ T cell analysis. CD68 also showed significant batch effects (data not shown) that could not be corrected and was removed from downstream analyses. Finally, we also noted that the magnitude of PD-1 (CD279) protein expression in GBM.pembro patients was specifically lower than GBM.new and GBM.rec, which likely indicates competition between the CyTOF antibody targeting CD279 and the humanized pembrolizumab antibody (data not shown).

Events were subsequently acquired on a Helios mass cytometer (Fluidigm) in the University of California, Los Angeles Jonsson Comprehensive Cancer Center Flow Cytometry core. After acquisition, all fcs files were normalized together using the R package premessa version 0.2.4 with the four element calibration beads (Fluidigm, cat: 201078). After normalization, live singlets were gated. Each markers' intensities were capped at 1st and 99th percentile, normalized from 0 to 1 and centered at the mean. Up to 20,000 cells were randomly subsampled from each sample. Dimensional reduction was performed using the Python implementation of UMAP using the reticulate R package version 1.18. Unsupervised clustering was carried out by PhenoGraph or ClusterX algorithm using R package cytofkit version 1.4.10. The median expression of each marker in each cluster was visualized by R package pheatmap version 1.0.12 and immune cell populations were identified based on the expression of specific markers.

Multiplex fluorescent immunohistochemistry: Formalin-fixed paraffin-embed- ded tissue sections of six recurrent GBM patients were stained for multiplex immunohistochemistry (mIF) to spatially visualize and quantify the tumor microenvironment. The following marker panel was used for staining by the Translational Pathology Core Laboratory (UCLA) using the Bond RX Fully Automated Research Stainer (Leica Biosystems, cat: 21.2821) and Opal Polaris 7 Color Automation IHC Detection Kit protocol (Leica Biosystems, cat: NEL871001KTIHC): CD14, CD206, HLA-DR, CD4, CD45, and CD8. Prior to antibody application, slides underwent a thirty-minute epitope retrieval process for CD14, HLA-DR, CD4, and CD8 using pH9 BOND epitope retrieval solution 2 (Leica Biosystems, cat: ER2). CD206 and CD45 used a pH6 BOND epitope retrieval solution 1 (Leica Biosystems, cat: ER1). Antibody clones and dilutions were per-formed in the following order conjugated to an Opal tyramide signal amplification reagent: CD14 (1:3500, Abcam, clone: EPR3653, cat: ab133335) with Opal 480, CD206 (1:300, Sigma-Aldrich, clone: CL0387, cat: AMAB90746-25UL) with Opal 520, HLA-DR (1:300, Abcam, clone: EPR3692, cat: ab92511) with Opal 570, CD4 (1:50, Dako, clone: 4B12, cat: M731029-2) with

Opal 620, CD45 (1:200, Dako, clone: 2B11 + PD7/26, cat: IR75161-2) with Opal 690, and CD8 (1:200, Dako, clone: C8/144B, cat: IR62361-2) with Opal 780. All slides were counter-stained with spectral DAPI (Akoya Biosciences) for nuclear detection. Multispectral whole tis- sue imaging of all slides was performed at a 40x magnification (0.25 μm/pixel) using the Vectra Polaris Automated Quantitative Pathology Imaging System (Akoya Biosciences, cat: CLS143455) by UCLA's Translational Pathology Core Laboratory. Whole tissue scanned images were then exported as a MOTiF Digital Slide format (.qptiff) file to allow for further viewing and ROI selection on Phenochart v1.0.12 (Akoya Biosciences). All images were spectrally unmixed using inForm image analysis software to identify and separate overlapping background autofluorescence per Opal and to provide a more accurate in situ visual for quantification.

All slides were spatially examined and quantified using HALO Image Analysis Software v3.0.311.398 (Indica Labs). Multilayered TIFF files from Inform were stitched together using HALO to reconstruct the unmixed whole tissue image. Appropriate nuclear segmentation and positive dye threshold intensities were determined for an overall whole tissue marker analysis. Tissue regions of interest were selected while autofluorescent, non-specific background was excluded. Multiplex IF raw data will be freely available to interested researchers.

Single-cell RNA sequencing: CD45+ cells were isolated using a Miltenyi bead pulldown and immediately frozen for batched analysis, as described above. Cell preparation, library preparation, and sequencing were carried out according to Chromium product-based manufacturer protocols (10X Genomics). Sequencing was carried out on a Novaseq6000 S2 2x50bp flow cell (Illumina) utilizing the Chromium single-cell 3′ gene expression library preparation (10X Genomics), per manufacturer's protocol at the Technology Center for Genomics and Bioinformatics Core, UCLA. Data were demultiplexed and aligned with Cell Ranger version 3.0.0 or higher (10X Genomics) and aligned to the Genome Reference

Consortium Human Build 38 (GRCh38). Data were then imported and analyzed with the Seurat package for R[110] version 3.1.5. For quality assurance, we examined the number of features per cell and percent mitochondrial RNA in each sample. Cells with >20% mitochondrial features were excluded from further analysis. The raw transcript count for each sample was individually normalized using the NormalizeData function. The Seurat data object from each sample were then integrated into one large Seurat object. Integrated expression values were further scaled by regressing out the percent mitochondrial features, cell cycle score[111], and the number of detected genes. For dimension reduction, we ran principal component analysis, uniform manifold approximation and projection (UMAP). Different cell cluster populations were defined using the FindNeighbors function and the genes that were differentially expressed in each cluster or treatment was computed using the FindMarkers or FindAllMarkers function.

Single-cell pseudotime trajectories: From all CD45+ cells analyzed by Seurat, we selected T cell and dendritic cell populations to separately do pseudotime trajectory analysis using Monocle 2.12.0[82]. First, we excluded lymphoid-myeloid doublets from this analysis. In particular, from the T cell clusters identified by Seurat, we removed any cells with expression of CD14 or CD68. Secondly, we separated CD4 and CD8 T cells by choosing cells with either at least one CD4 transcript and no CD8 transcript or the other way around. DC cells were selected from the Seurat's DC cluster, from which we removed cells with any expression of CD3D/E/G or CD8A/B. After selecting the "pure" CD4, CD8 T cell, and dendritic cell populations, we extracted the normalized gene-cell expression matrix of each population to construct the CDS object in Monocle2. We also used Seurat's FindVariableFeatures function to choose the top 1000 most variable genes as the ordering features for trajectory construction. Dimension reduction was performed using Discriminative Dimensionality Reduction with Trees (DDRTree) algorithm. The pseudotime trajectory was then learned by orderCell function in Monocle2. The expression of selected genes was visualized using Monocle2's plot multiple_branches_heatmap function.

T cell receptor analysis. We inferred CDR3 sequences of T cell receptors from the single-cell RNAseq bam files using the TRUST4 software version 1.0.2. Cells with at least one productive TCRβ chain were kept for subsequent analysis. Cells with the same TCRβ sequence were considered to be one TCR clone. A clone with at least two cells in a given population was defined as an expanded clone. The likelihood of two cell populations to share clones was defined by the transition index computed using TCR TRACking (STARTRAC) method version 0.1.0. We noted that the number of TCR clone detected per patient is generally low and, as such, we were only able to perform a group-based analysis to describe the overall transition patterns of T cells from different TIL and PBMC clusters.

Interactome analysis: We analyzed our scRNAseq data for potential ligand receptor (LR) interaction using the CellChat R package version 1.1.1[95]. Specifically, we analyzed potential interactions among the cells from the 28 immune subpopulations that we defined in our lymphoid (L1-L7), macrophage (Mφ1-8), DC (cDC1-2, migratory DC/mDC, moDC1-4), and monocytes (classical monocyte 1-2, Mφ-like1-4); cells from the tumor-normal like clusters, doublets, and unknown clusters were excluded from this analysis. We first generated separate cellchat objects for the GBM.new, GBM.rec and GBM.pembro cells (following closely the analysis steps for single dataset at https://github.com/ sqjin/CellChat). Subsequently, we proceeded with comparison analysis in order to infer differentially enriched ligand receptor interaction among the tumor groups. The interaction comparisons were performed using the compareInteractions and RankNet functions. We visualized the significant pathway LR interactions across all tumor groups using the netAnalysis_signalingRole_heatmap function, setting the option pattern = “all” to aggregate the incoming and outcoming signaling strengths. Dot plots showing the normalized expression levels (color) and fraction cell expressing the genes (size of dot) in specific pathways were visualized using the plotGeneExpression function

with the option type = “dot”. The circle plots depicting interactions among different immune populations in each tumor group were done by applying netVisua- l_aggregate with the option layout = “circle”.

Statistics and reproducibility: The statistical tests used to calculate the P-values are indicated in respective figures. Other than the differentially expressed genes called by Seurat, all P-values calculated for the boxplots and violin plots were nominal (unadjusted) P-values. Statistical analysis of the data presented in the violin plots was done using GraphPad Prism version 8.4.0.

Data availability:

Single-cell RNA sequencing raw data files are available in the Gene Expression Omnibus under accession number GSE154795 and CyTOF raw data files are stored at the Flow Repository under the ID FR-FCM-Z4LX. These files supply the data for Figs. 1–6 and Supplementary figs. 1–7. The raw single-cell RNA sequencing was aligned to the Genome Reference Consortium Human Build 38 (GRCh38, GCA_000001405.15) prior to analysis. The remainder of data that support the findings of this study, including multiplex IHC images and data files and processed CyTOF fcs files ready for analysis, are available from the corresponding author upon reasonable request.

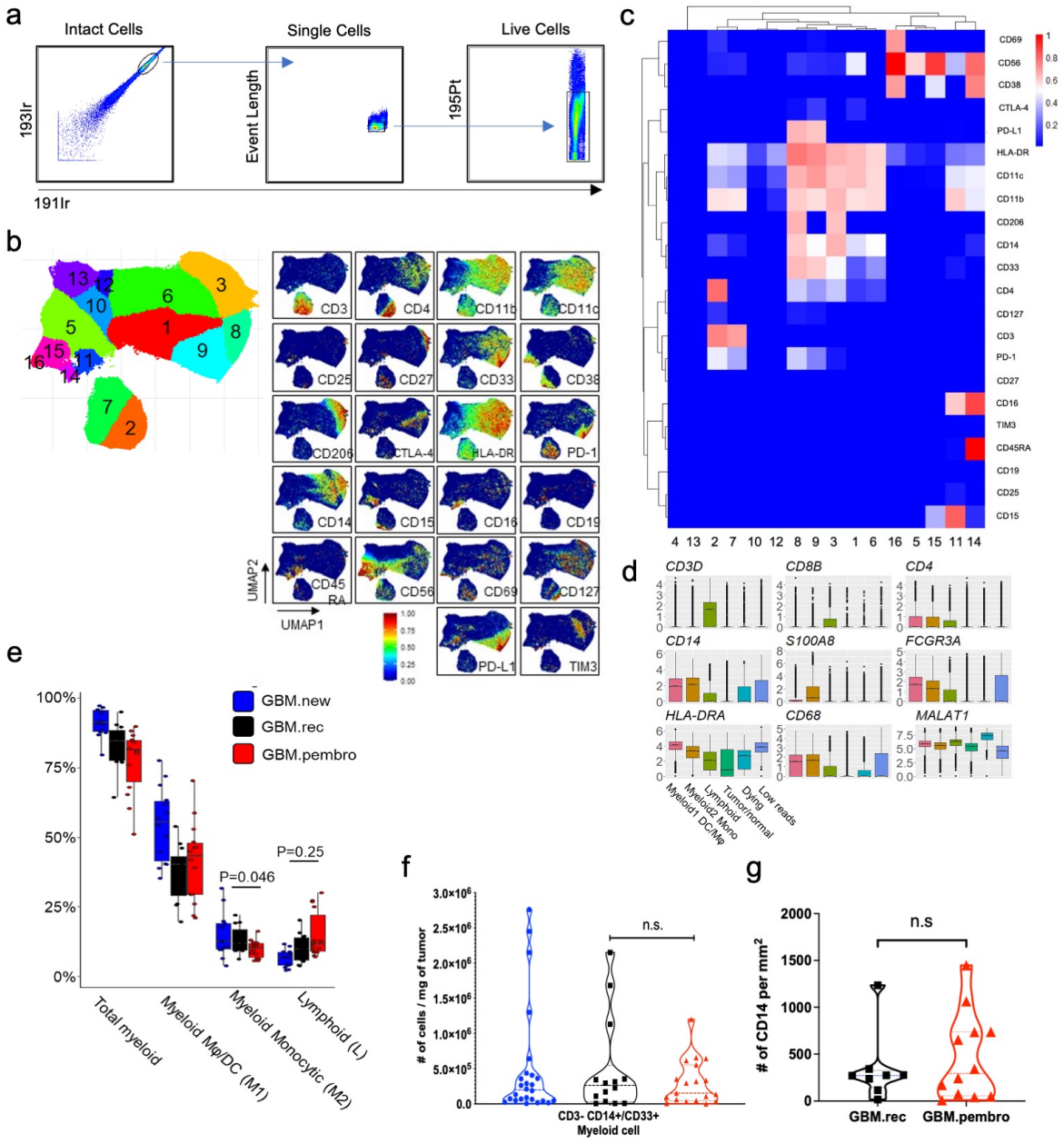

Supplementary Figure 1. Clustering of GBM-derived CD45+ cells based on the CyTOF and scRNAseq profiles.

A) Representative gating of raw fcs files to analyze the live intact single cells for subsequent CyTOF analysis.

B) (top) The clustering of tumor-infiltrating CD45+ cells analyzed on the 22 common marker CyTOF panel projected onto the UMAP space (n=1,067,057 cells from 63 total patients: 26 GBM.new, 17 GBM.rec, 20 GBM.pembro). The top large UMAP island is occupied by the

different myeloid clusters while the bottom smaller island comprises the different lymphoid clusters. (bottom) UMAP plots of marker intensities on the TILs on the 22 marker CyTOF antibody panel

C) *Heatmap of marker intensities on the CD45's on the 22 marker CyTOF antibody panel.*

D) *Expression of marker genes of distinct cell clusters derived from the scRNAseq data of GBM samples (n=156,766 cells from 40 total patients: 14 GBM.new, 12 GBM.rec, and 14 GBM.pembro).*

E) *The proportion of the cells in each cluster across the three groups of GBM samples (blue: GBM.new, black: GBM.rec, red: GBM.pembro).*

F) *The number of CD3- CD14/CD33 myeloid cells per mg of tumor across different tumor groups. Colors are the same as (e).*

G) *The number of CD14+ cells per mm^2 of tissue section for GBM.rec (black squares) and GBM.pembro (red triangles) samples. Images were collected and analyzed for 8 GBM.rec and 12 GBM.pembro patients.*

P values were calculated using a two-sided Wilcoxon rank sum test. In all boxplots, the median is indicated by the line within the box and the 25th and 75th percentiles indicated by the lower and upper bounds of the box. The upper and lower lines above and below the boxes represent the whiskers.

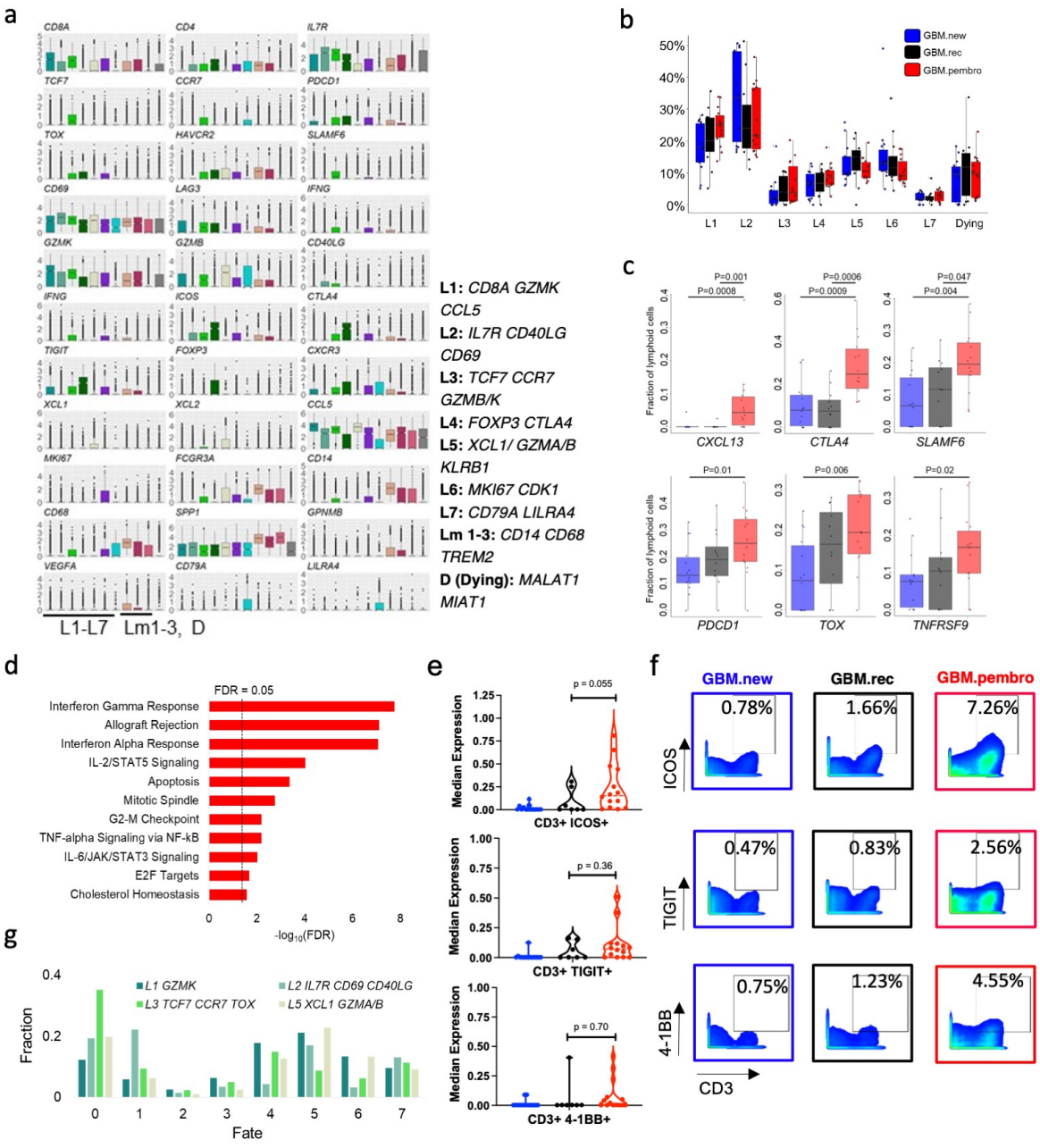

Supplementary Figure 2 – Identification of different lymphoid subpopulations from scRNAseq.

A) Expression of various genes across the different clusters used to identify the lymphoid populations in the TILs (n=14,322 cells from 40 total patients: 14 GBM.new, 12 GBM.rec, and 14 GBM.pembro).

B) The sample level proportions of each lymphoid cluster in (a) across GBM.new (blue), GBM.rec (black) and GBM.pembro (red).

C) The fraction of lymphoid cell expressing indicated transcripts in GBM.new, GBM.rec and GBM.pembro samples.

D) MSigDB Hallmark genesets showing significant overlap with the union of the genes upregulated in the GBM.pembro group across all lymphoid clusters (FDR values, two-sided fisher exact test).

E) Change in median expression of CD278 (ICOS), TIGIT, and 4-1BB (CD137) across all CD3+ clusters. Colors and statistical analysis are the same as (b) and (c).

F) Marker expression CD278 (ICOS), TIGIT, and 4-1BB (TNFRSF9) in the combined CyTOF data of the CD3+ T cells.

G) The fractions of CD8 T cells from the different Seurat clusters in (a) occupying the different T cell fates defined by the Monocle 2's pseudotime trajectory.

P values were calculated using a two-sided Wilcoxon rank sum test In all boxplots, the median is indicated by the line within the box and the 25th and 75th percentiles indicated by the lower and upper bounds of the box. The upper and lower lines above and below the boxes represent the whiskers. The gene set enrichment P values were calculated using two-sided Fisher exact test with FDR adjustment for multiple comparisons.

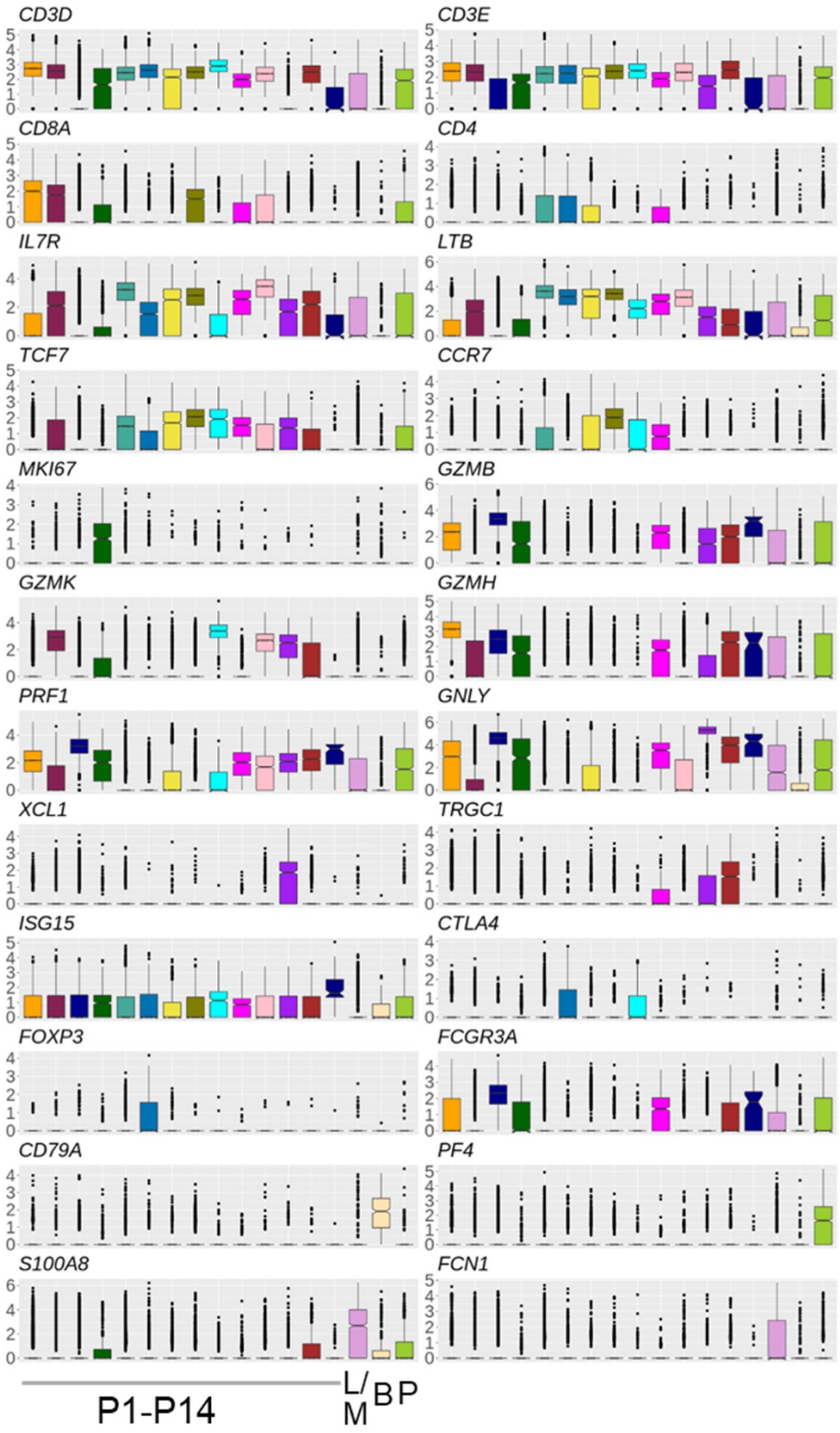
CD3D
CD3E
CD8A
CD4
IL7R
LTB
TCF7
CCR7
MKI67
GZMB
GZMK
GZMH
PRF1
GNLY
XCL1
TRGC1
ISG15
CTLA4
FOXP3
FCGR3A
CD79A
PF4
S100A8
FCN1
P1-P14
L/M
BP

Supplementary Figure 3 – Expression of lymphoid markers in the PBMC scRNAseq

Expression of various genes across the different clusters that were used to identify the T cell populations in the PBMC (n=56,444 cells from 5 GBM.rec and 8 GBM.pembro patients and from 2 healthy donor controls). In all boxplots, the median is indicated by the line within the box and the 25th and 75th percentiles indicated by the lower and upper bounds of the box. The upper and lower lines above and below the boxes represent the whiskers.

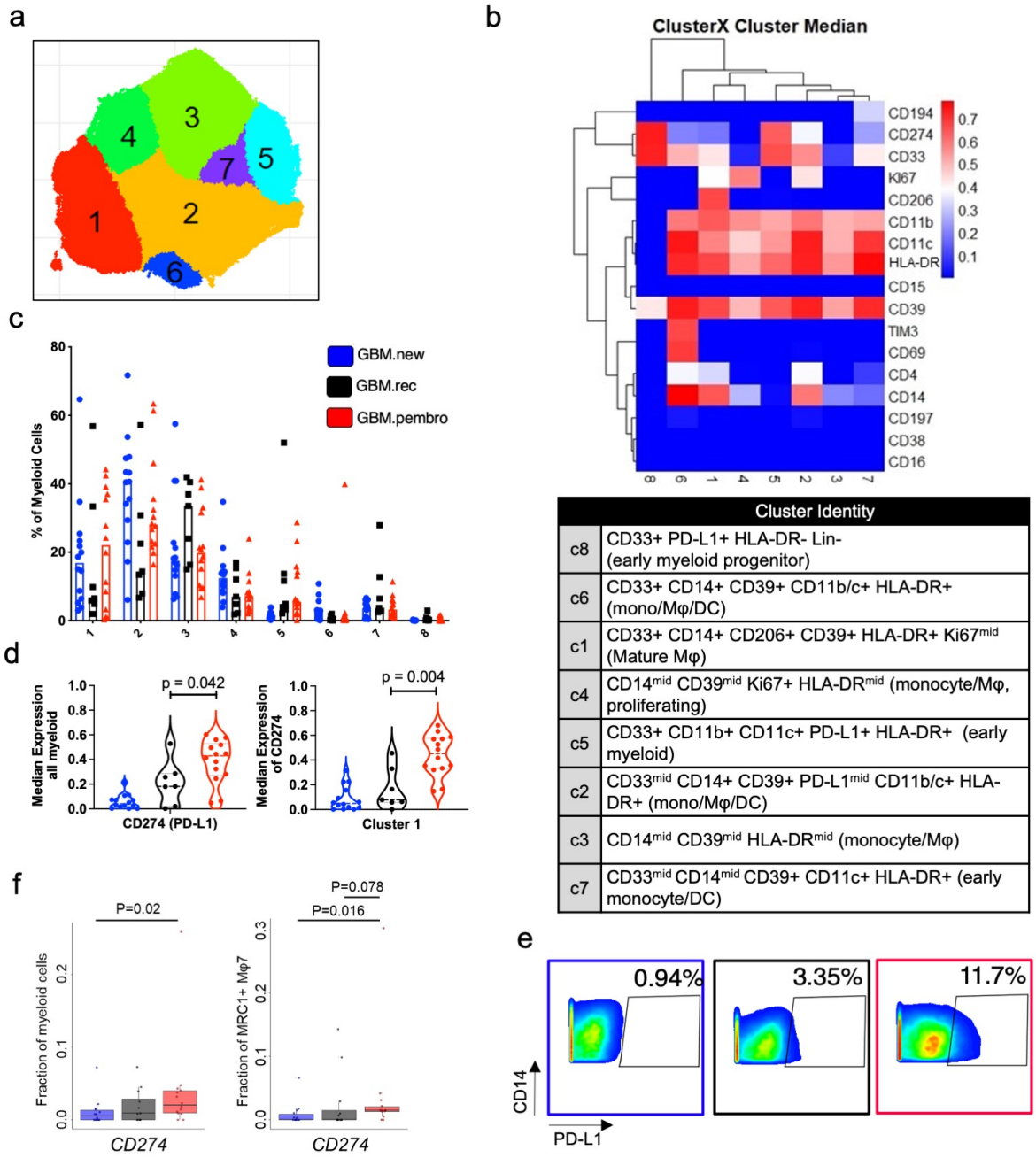

Cluster Identity	
c8	CD33+ PD-L1+ HLA-DR- Lin- (early myeloid progenitor)
c6	CD33+ CD14+ CD39+ CD11b/c+ HLA-DR+ (mono/Mφ/DC)
c1	CD33+ CD14+ CD206+ CD39+ HLA-DR+ Ki67^{mid} (Mature Mφ)
c4	CD14^{mid} CD39^{mid} Ki67+ HLA-DR^{mid} (monocyte/Mφ, proliferating)
c5	CD33+ CD11b+ CD11c+ PD-L1+ HLA-DR+ (early myeloid)
c2	CD33^{mid} CD14+ CD39+ PD-L1^{mid} CD11b/c+ HLA-DR+ (mono/Mφ/DC)
c3	CD14^{mid} CD39^{mid} HLA-DR^{mid} (monocyte/Mφ)
c7	CD33^{mid} CD14^{mid} CD39+ CD11c+ HLA-DR+ (early monocyte/DC)

Supplementary Figure 4 – CyTOF based clustering of the myeloid cells.

A) UMAP projections showing specific marker intensities of the markers in the 32 marker CyTOF antibody panel (Supplementary Table 2).

B) Heatmap of the marker expression intensities in each cluster. The combination of markers used to identify each cluster are listed in the table below the heatmap

C) *The percentage of tumor infiltrating CD45's within each cluster from (b) across different tumor conditions (blue circles: GBM.new, Black squares: GBM.rec, Red triangles: GBM.pembro). P values were calculated using the Wilcoxon rank sum test*

D) *Median CD274 (PD-L1) expression across all clusters (left) and in cluster 1(right) separated by tumor diagnoses. Colors the same as (c). P values were calculated using the Wilcoxon rank sum test (*: p≤0.05, **: p≤0.01)*

E) *Marker expression for CD14 and CD274 (PD-L1) in the combined, batch-corrected CYTOF data. Colors are the same as (c). Percentages represent the percent of CD14+ cells*

F) *Median CD274 (PD-L1) mRNA expression in all myeloid cells (left) or only in Mφ cluster 7. Colors the same as (c). P values were calculated using the Wilcoxon rank sum test (*: p≤0.05, **: p≤0.01)*

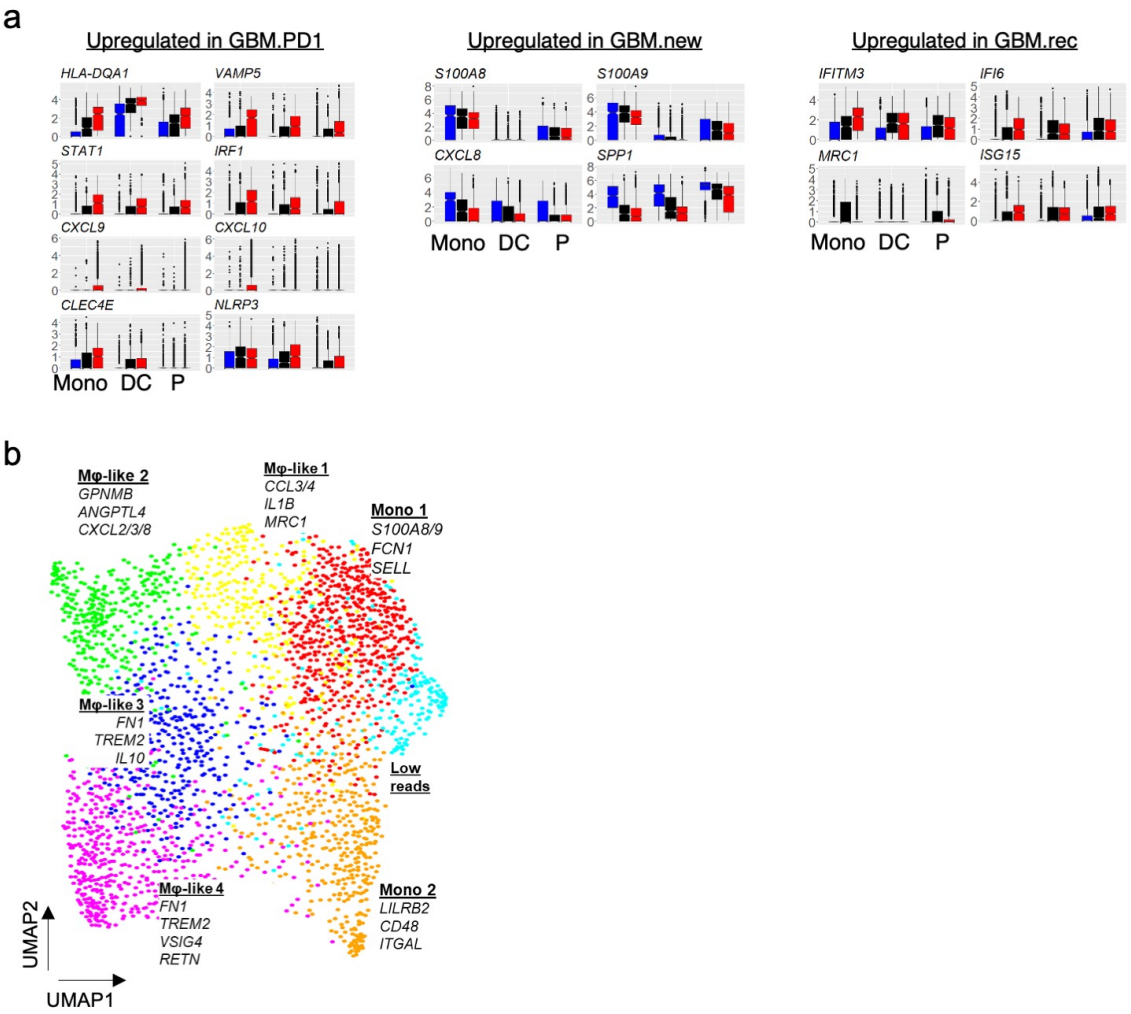

Supplementary Figure 5 – Increased activity of IL10+ immunosuppressive monocytic populations

A) Differentially expressed genes across the different conditions in the monocyte, DC, and proliferating myeloid clusters (blue: GBM.new, black: GBM.rec, red: GBM.pembro; n=2,677 cells from from 40 total patients: 14 GBM.new, 12 GBM.rec, and 14 GBM.pembro).

B) A UMAP projection of the monocytic compartment of the 40 patient samples that were analyzed using scRNAseq.

In all boxplots, the median is indicated by the line within the box and the 25th and 75th percentiles indicated by the lower and upper bounds of the box. The upper and lower lines above and below the boxes represent the whiskers.

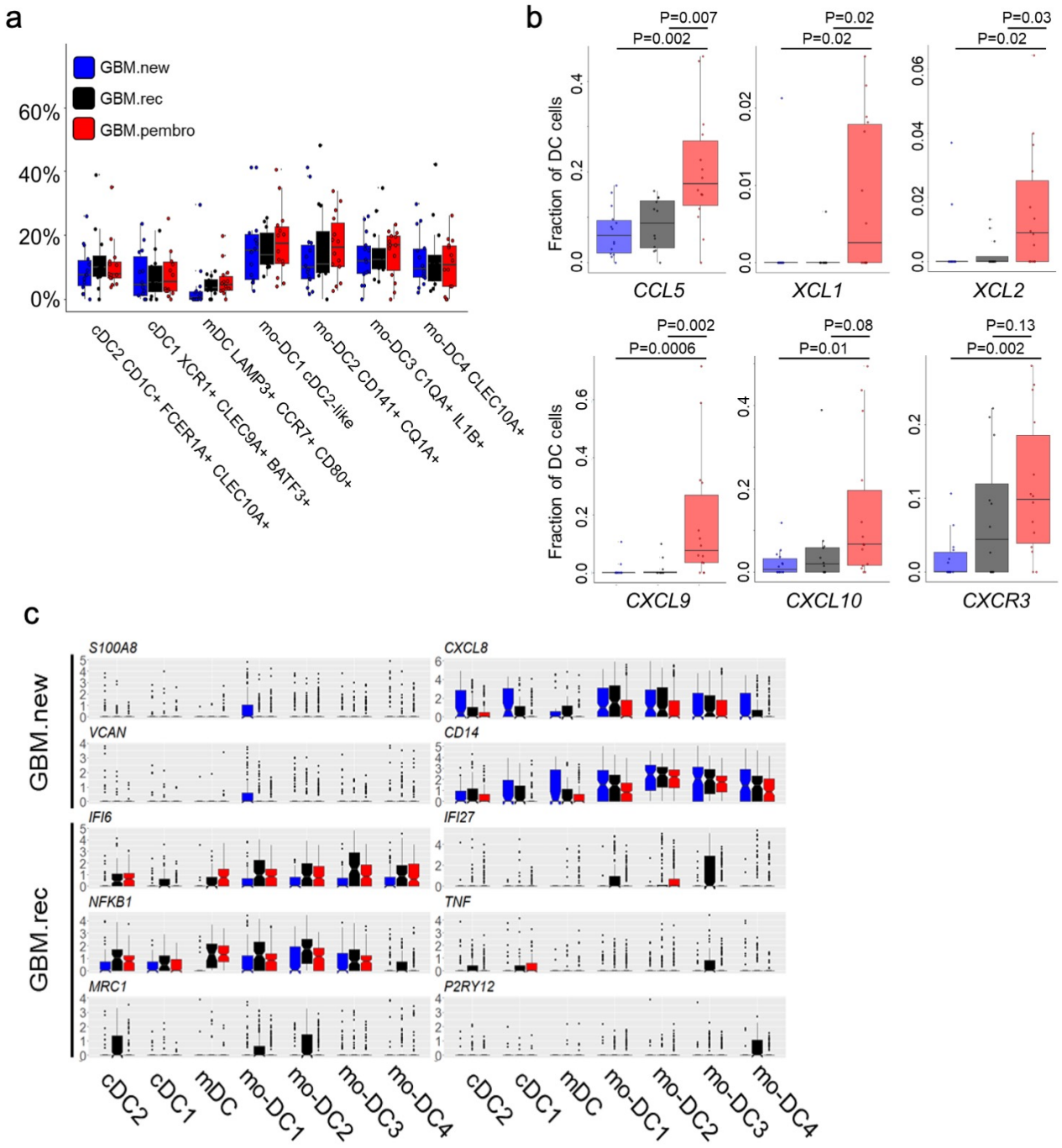

Supplementary Figure 6 – scRNAseq analysis of the dendritic cell populations.

A) The proportion of dendritic cells in each cluster across multiple tumor types (blue: GBM.new, black: GBM.rec, red: GBM.pembro; n=2,960 cells from 40 total patients: 14 GBM.new, 12 GBM.rec, and 14 GBM.pembro).

B) The fraction of dendritic cells with a transcript of indicated genes. Colors are the same as (a).

C) Differentially upregulated genes in GBM.new (top) or GBM.rec (bottom) samples in at least one of the dendritic cell clusters.

P values were calculated using a two-sided Wilcoxon rank sum test. In all boxplots, the median is indicated by the line within the box and the 25th and 75th percentiles indicated by the lower and upper bounds of the box. The upper and lower lines above and below the boxes represent the whiskers.

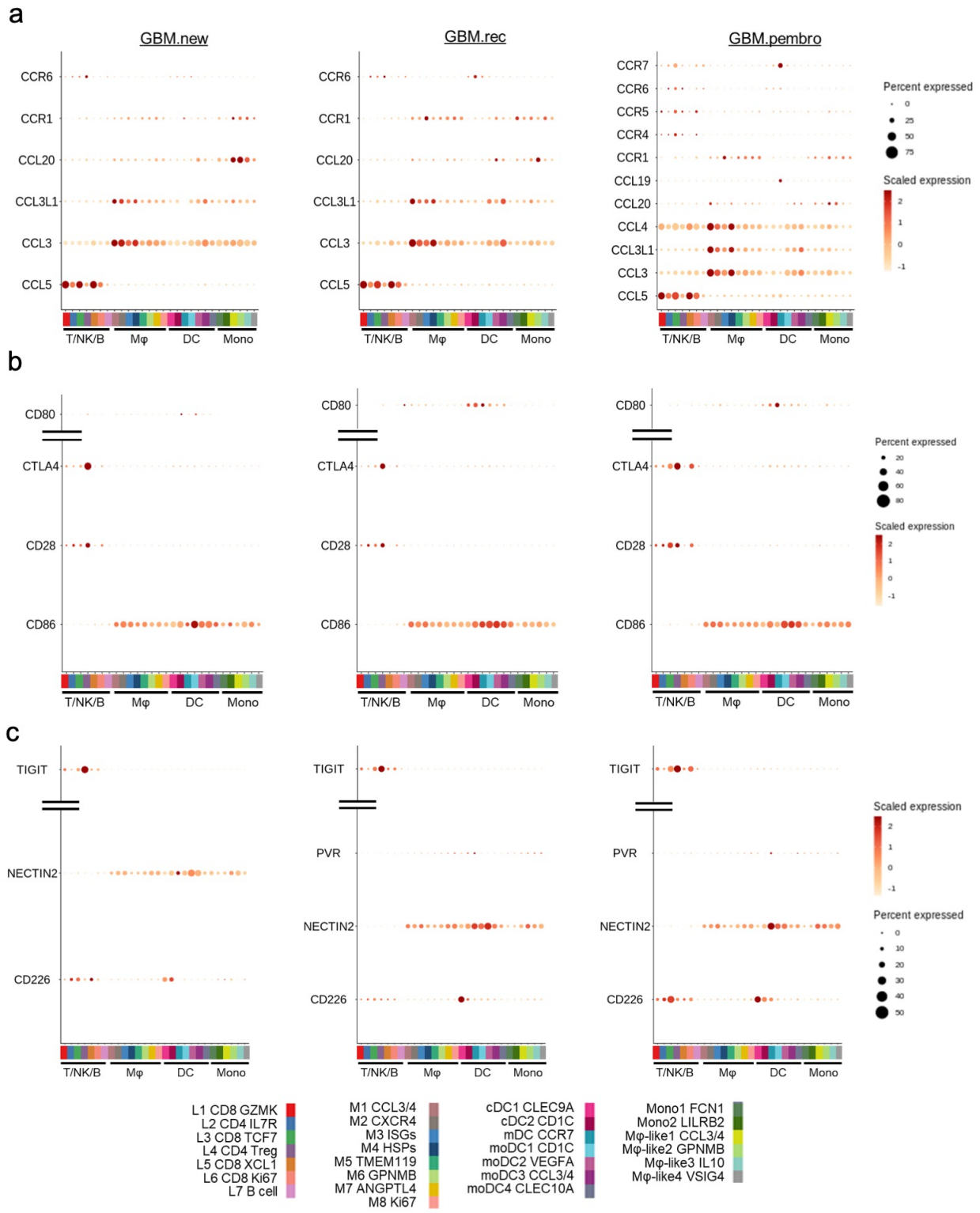

Supplementary Figure 7 – Significantly enriched receptor ligand interactions after neoadjuvant anti-PD1

A) The normalized expression of CCL pathway genes with significant expression in indicated tumor groups.

B) Same as (a) for CD28-CTLA4-CD86 pathway. The expression of CD80 is included from a separate graph including CD28, CTLA4, and CD80.

C) Same as (a) for CD226-PVR-NECTIN2 pathway. The expression of TIGIT is included from a separate graph including TIGIT, PVR, and NECTIN2.

Interactome analysis on the scRNAseq data was conducted using n=156,766 cells from 40 total patients: 14 GBM.new, 12 GBM.rec, and 14 GBM.pembro.

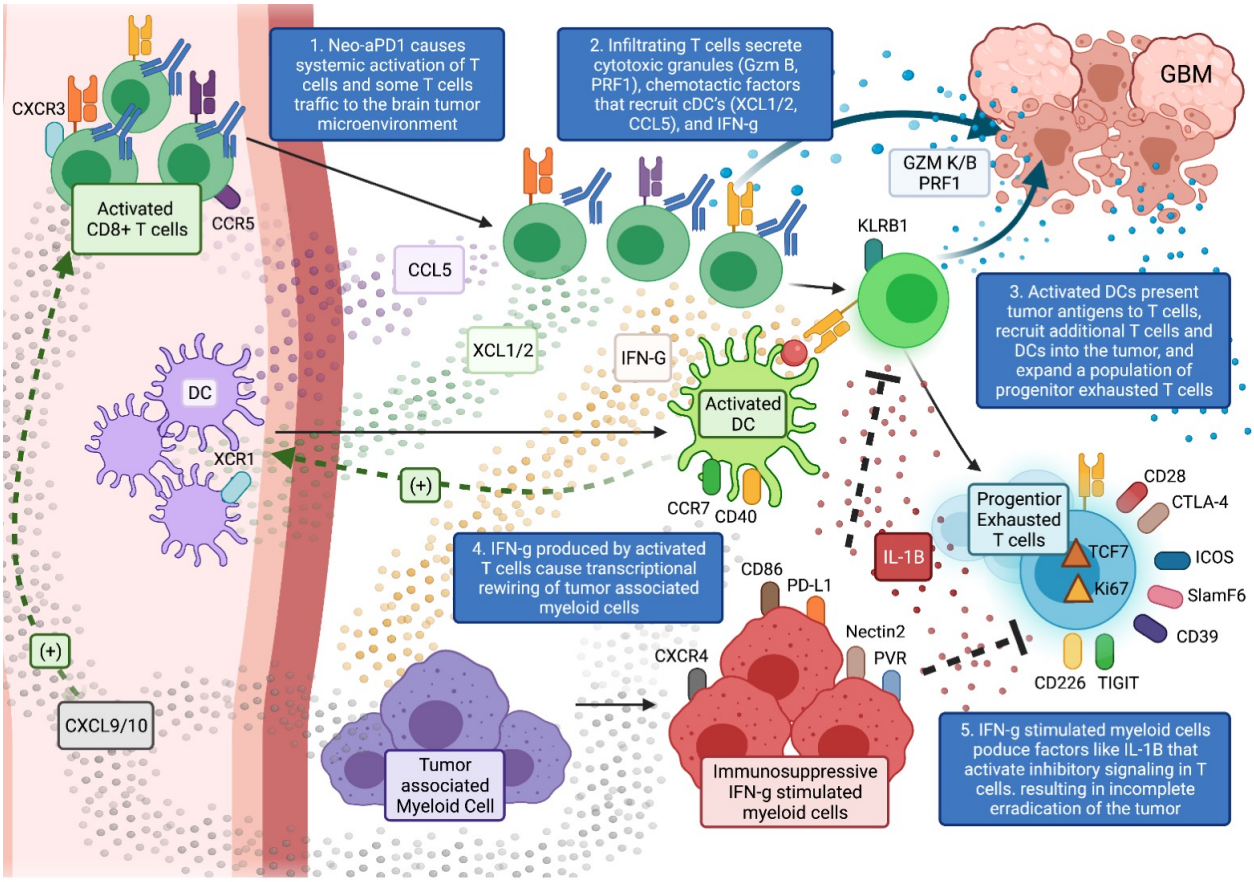

Supplementary Figure 8 - A schematic proposing how neo-aPD1 changes the immune landscape in the recurrent GBM tumor microenvironment. Biorender.com was used to create this schematic.

Chapter 3: Identification and Isolation of tumor-reactive TCR clonotypes based on in silico single-cell transcriptomic and TCR profiling in recurrent glioblastoma patients treated with neoadjuvant anti-PD-1 therapy

Abstract

Background: Glioblastoma (GBM) is the most severe form of primary brain cancer with no current cure. Despite the effectiveness of checkpoint blockade and adoptive T cell therapy in other cancer types, these therapies have shown limited efficacy in the glioblastoma setting due to an immunosuppressive tumor microenvironment and general lack of known tumor-associated T cell targets. Methods & Results: Using single-cell RNA sequencing technology, we investigated the transcriptomic signature of tumor-infiltrating T cell populations from 32 recurrent GBM patients, 18 of whom had received neoadjuvant anti-PD-1. On 14 patients within this 32 patient cohort, we also performed single-cell TCRsequencing to pair with the gene expression data. Based on the transcriptome, T cell clones with an activated and exhaustion T cell phenotype had the greatest clonal expansion and similarity to previously reported signatures of tumor-reactive infiltrating T cells. From one patient treated with neoadjuvant anti-PD-1 therapy and an EGFRvIII bispecific antibody therapy, we selected TCRs from the activated/exhausted and progenitor exhausted subpopulations and utilized the PathFinder DNA Assembly technology from Rootpath to rapidly generate TCR libraries. To isolate potential tumor-reactive TCRs within the libraries, we transduced these libraries into triple-reporter Jurkat cells and FACS sorted for T cells with an activated signature after co-culturing with a patient-matched gliomasphere cultures. We sequenced the sorted T cells and discovered that six TCRs within the sorted population were over-represented relative to control co-cultures, which indicates tumor reactivity. Conclusions: All in all, our study is a proof-of-concept for how in silico single-cell analysis of a T cell's transcriptome and TCR can be used to identity tumor-reactive T cells and be potentially applied in future adoptive T cell transfer therapies.

Introduction

Glioblastoma (GBM) is the most common malignant primary brain tumor in adults. Despite multimodal treatment, progression is nearly inevitable and salvage therapies provide nominal benefit with median overall survival up to 44 weeks[112]. For this reason, no universally held standard of care is available for recurrent glioblastoma.

Despite the successes of immunotherapy in other cancer types, thus far, attempts to treat recurrent GBMs with immunotherapy, such as sustaining intratumoral T cell activity using checkpoint blockade or pursuing adoptive T cell transfer, have been met with limited clinical success[5-7,113]. Nevertheless, a subset of patients respond to immunotherapy and have a sustained immune response against GBMs[59,114,115]. Additionally, in a separate study, we analyzed how the tumor microenvironment changes with neoadjuvant anti-PD-1 and showed that neoadjuvant anti-PD-1 therapy was associated with a clonal expansion in tumor-infiltrating activated and progenitor exhausted T cell subpopulations[11].

Studies such as the ones above show how the growing accessibility to single-cell RNA sequencing technologies allows deeper exploration into the transcriptomes of tumor-infiltrating immune populations and into the TCR repertoire of intratumoral T cells, of which only a small percentage are actually tumor reactive[116]. By utilizing the data generated from these technologies, transcriptomic signatures that distinguish intratumoral tumor-reactive T cells from bystander T cells have been discovered in other cancer types[52,117-120]. However, translating the growing wealth of data into clinical T cell based immunotherapies remain challenging for a couple of reasons: one, identifying the rare population of tumor-reactive T cells from the larger pool of tumor-infiltrating T cells, and two, isolating and validating TCRs from this rare population due to the effort required to create TCR libraries at a rapid and efficient scale.

In this study, we examined how pairing single-cell transcriptomic and TCR data of tumor-infiltrating T cells can guide the selection of potential tumor-reactive clonotypes and how utilizing such new technologies can rapidly and more efficiently validate these clonotypes. In this study, we performed single-cell RNA and on the tumor-infiltrating immune population from 32 recurrent GBM patients, 18 of whom had received neoadjuvant anti-PD-1 therapy, and performed paired single-cell TCR sequencing of the tumor-infiltrating T cells in 14 of the patients. In a patient who had been treated with neoadjuvant anti-PD-1 and a EGFRvIII bispecific antibody therapy, we identified TCRs from T cells with a late activated/exhausted or a progenitor exhausted T cell phenotype and utilized the PathFinder DNA Assembly platform developed by Rootpath to rapidly generate TCRs libraries containing the TCRs from these populations. We cloned these libraries into a triple-reporter Jurkat line[121], and FACS-sorted activated T cells after co-culturing with a gliomasphere line derived from the patient's tumor or a non-patient matched gliomasphere line. We sequenced the sorted T cells and discovered several clonotypes that were over-represented in the sorted population from that patient-matched gliomasphere co-culture compared to the non-patient matched gliomasphere co-culture.

Therefore, this study is a proof-of-concept for how in silico analysis of both the transcriptomic and TCR signature of intratumoral T cells can be utilized as a guide to find tumor-reactive TCRs for use in adoptive T cell therapies in the recurrent GBM context and how new technologies that allow for rapid TCR cloning may accelerate the discovery and/or confirmation of candidate tumor-reactive TCRs.

Patient Characteristics, Data Acquisition, and Initial Data Analysis of immune populations

We performed 5' scRNAseq and scTCRseq on tumor-infiltrating CD45+ immune cells from 14 recurrent GBM patients, 7 of whom had received neoadjuvant anti-PD-1 therapy (GBM.pembro) and 7 of whom had no prior immunotherapy treatment (GBM.rec). To aid with cell clustering, we also incorporated the 3' scRNAseq gene expression of our previously published cohort of GBM.rec and GBM.pembro patients (18 patients: 11 GBM.pembro and 7 GBM.rec)[11]. After the standard pre-processing steps on the Seurat platform[122], we analyzed the gene expression profiles from a total of 145,113 cells from these 32 patients and performed dimensional reduction using uniform manifold approximation and projection (UMAP)[123]. We observed 7 clusters with more than 5 cells (4 clusters of myeloid and/or dendritic cells, 1 cluster of lymphoid cells, 1 cluster of tumor cells, and 1 cluster of proliferating cells) (**Supp Fig 1A-C**).

To analyze the T cell compartment in finer detail and to more accurately parse out the T cell subsets, we performed an additional clustering step on CD3+ cells in the lymphoid cluster, selecting for patients with greater than 100 CD3+ lymphoid cells (n = 26 patients, 11 GBM.rec, and 15 GBM.pembro, 11,783 CD3+ lymphoid cells analyzed). We identified 14 lymphoid clusters that included (**Fig 1A**): 1 cluster of early activated progenitor exhausted T cells (*IL7R*, *CD40LG*, *KLRB1,TCF7*), 1 cluster of late activated and/or exhausted CD8 T cells (*GZMK*, *NKG7*, *CRTAM*, *PRF1*, *GZMB*, *PDCD1*, *TIGIT,* TOX), 1 cluster of intermediate activated T cells (*ICOS*, *GZMK*, *IL7R*), 1 cluster of intermediate activated progenitor exhausted T cells (*TCF7*, *SLAMF6*, *BACH2*, *TOX*, *PDCD1*, *TIGIT*), 1 cluster of T_{reg} cells (*FOXP3*, *TIGIT*, *CTLA4*), 1 cluster of interferon stimulated T cells (*ISG16*, *IFI6*, *IFIT1*, *LAG3*), 3 clusters of T cell/myeloid doublets (*CD14*, *CD68*, *APOE*), 1 cluster of B cell/T cell doublets (*CD79A*), 1 cluster of migratory NK-like T cells (*KLRD1*, *CD160*, *XCL1/2*, *KLRC1*), 1 cluster of activated NK-like T cells (*GZMB*, *KLRD1*, *PRF1*, *KLRC1*), 1 cluster of proliferating cells (*MIK67*), and 1 cluster of heat-shock/dying cells (*HSPA1A*, *HSPA1B*).

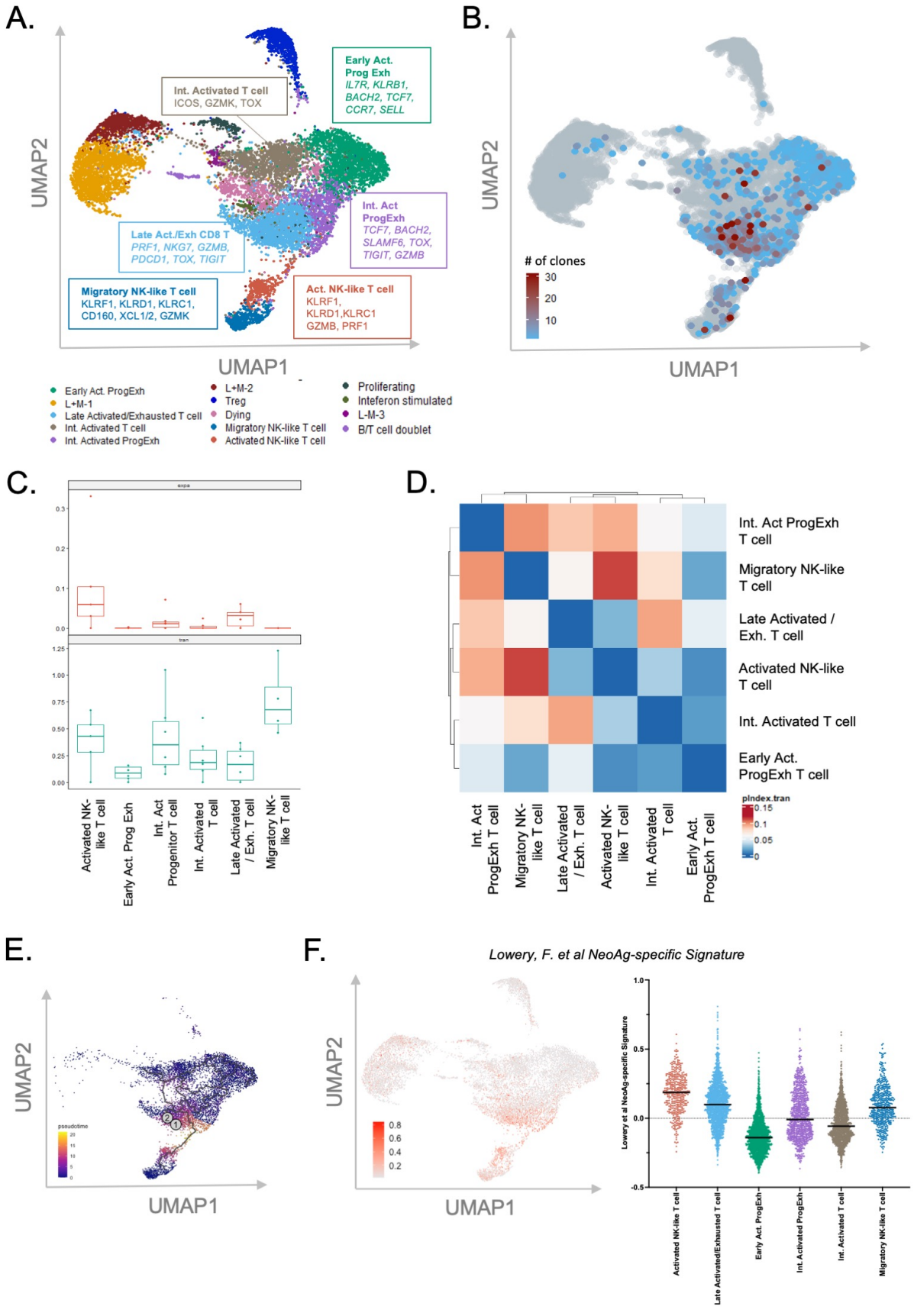
A.
Early Act. Prog Exh
IL7R, KLRB1, BACH2, TCF7, CCR7, SELL
Int. Activated T cell
ICOS, GZMK, TOX
Int. Act ProgExh
TCF7, BACH2, SLAMF6, TOX, TIGIT, GZMB
Late Act./Exh CD8 T
PRF1, NKG7, GZMB, PDCD1, TOX, TIGIT
Migratory NK-like T cell
KLRF1, KLRD1, KLRC1, CD160, XCL1/2, GZMK
Act. NK-like T cell
KLRF1, KLRD1,KLRC1 GZMB, PRF1
UMAP2
UMAP1
Early Act. ProgExh
L+M-1
Late Activated/Exhausted T cell
Int. Activated T cell
Int. Activated ProgExh
L+M-2
Treg
Dying
Migratory NK-like T cell
Activated NK-like T cell
Proliferating
Inteferon stimulated
L-M-3
B/T cell doublet
B.
UMAP2
UMAP1
# of clones
30
20
10
C.
Activated NK-like T cell
Early Act. Prog Exh
Int. Act Progenitor T cell
Int. Activated T cell
Late Activated / Exh. T cell
Migratory NK-like T cell
D.
Int. Act ProgExh T cell
Migratory NK-like T cell
Late Activated / Exh. T cell
Activated NK-like T cell
Int. Activated T cell
Early Act. ProgExh T cell
pIndex.tran
0.15
0.1
0.05
0
E.
UMAP2
UMAP1
pseudotime
F.
Lowery, F. et al NeoAg-specific Signature
UMAP2
UMAP1
Lowery et al NeoAg-specific Signature
Activated NK-like T cell
Late Activated/Exhausted T cell
Early Act. ProgExh
Int. Activated ProgExh
Int. Activated T cell
Migratory NK-like T cell

Figure 1: Single-cell RNA and TCRseq show T cell expansion, enrichment, and potential tumor-reactivity in the late activated and exhausted T cell cluster

A) UMAP projection of the CD3+ lymphoid cell subcluster. Relevant genes used to classify six T cell clusters are boxed and color-coded to match the cluster color displayed on the UMAP projection

B) UMAP projection showing T cell clone numbers in the CD3+ lymphoid population, calculated by the TRB CDR3 region

C) Graphs showing the STARTRAC-expa (top) and STARTRAC-tran (bottom) indices of cells in the six T cell clusters. Each dot represents a patient within the cohort

D) Heat map showing STARTRAC-tran indice, examining shared TCR clones across multiple clusters. The higher the value, the more likely that the T cells in the two clusters transition from one to the other

E) A UMAP projection of the six T cell clusters and displaying the Monocle 3 pseudotime progression. The Early Act. ProgExh population was used as the root. The numbered gray circles indicate a leaf, which corresponds to a different cell fate of the trajectory

F) *A UMAP projection displaying expression levels of a geneset associated with neoantigen-reactive TCRs reported by Lowery, F., et al (2021) calculated using the AddModuleScore function in the Seurat package (left). Quantified expression scores across the six T cell clusters (right). Each dot represents the score of an individual cell in the cluster and the median expression score level of all cells in the cluster is indicated by the black line*

We continued our analysis in the cohort of 14 patients for whom we had performed scTCRseq on (12 patients had enough CD3+ lymphoid cells to analyze: 7 GBM.rec and 5 GBM.pembro, n=4,130 CD3+ lymphoid cells) and examined cells from the following clusters: the 1 cluster late activated and/or exhausted CD8 T cells, 1 cluster of intermediate activated T cells, 1 cluster of early activated progenitor exhausted CD8 T cells , 1 cluster of activated progenitor exhausted CD8 T cells, 1 cluster of migratory NK-like T cells, and the 1 cluster of activated NK-like T cells (**Supp Fig 2A,B**). From these patients, 587 cells had at least one TCR beta chain captured.

When we overlayed the scTCR clonotype data onto our UMAP projection, we observed that many of the T cells with expanded clones (clone size >1) existed in the Late Activated and Exhausted T cell population (**Fig 1B**). Others have shown that tumor-reactive T cells frequently expand in the tumor[124] and have a similar exhausted/dysfunctional transcriptomic signatures as the cluster noted here[125]. Recently, several publications have reported *CXCL13* expression as a relevant marker for tumor-reactive TCRs in other cancer types[117,126]. In our dataset, *CXCL13* expression was not exclusively expressed in any of the 6 particular clusters (**Supp Fig 2A, B**). Other genes typically associated with tumor-reactive T cells, such as *TNFRS9*[127] and *ENTPD1*[117], were also broadly expressed across the clusters, though most expressed within the intermediate activated progenitor exhausted CD8 T cell cluster. This may indicate that these particular genes alone may not be informative enough to predict tumor-reactive TCRs within the recurrent GBM context and that a more robust gene signature needs to be characterized.

To determine in an unbiased manner which clusters contained T cells that had most likely expanded and which T cells were more likely to transition from one cluster to another, we utilized the STARTRAC[87] algorithm (**Fig 1C,D**). We found that the Late Activated and Exhausted T cell and Activated NK-like T cell clusters were the clusters with the highest T cell expansion score, a measure of clonality (**Fig 1C, top**). Utilizing STARTRAC's transition index,

which measures the likelihood of TCRs transitioning from or into a specific cluster, we observed that the clusters with the highest transitions scores were: Migratory NK-like T cell, Activated NK-like T cell, and Int. Act Progenitor Exhausted T cell clusters (**Fig 1C, bottom**).
Examining the clusters that had the highest likelihood of transition between one another using STARTRAC's Pairwise Transition index, we observed that overlap between: (1) the Migratory NK-like and Activated NK-like clusters, (2) the intermediate activated to late activated/exhausted clusters, (3) the Intermediate Activated Progenitor Exhausted clusters and the Migratory, Activated, and Late Activated/Exhausted clusters, indicating transition between these various clusters (**Fig 1D**).

To analyze cell progression to include all T cells, whether a TCR was detected or not, we utilized Monocle3[128] to perform a pseudotime analysis on our T cell populations. Using the Early Activated ProgExh T cell cluster as the root, we observed that cells transitioned into the Late Activated/Exhausted T cell population, indicating that this cluster of cells represented the most differentiated state and potentially explaining the high degree of clonal expansion within this cluster (**Fig 1E**).

Additionally, we used the *AddModuleScore* function in Seurat to examine whether a recently reported gene signature for neoantigen-reactive T cells in metastatic tumors across multiple solid tumor types[118] existed in our dataset and if it correlated with any of our defined populations. The clusters with a positive score based off the reported gene signature were the Late Activated and Exhausted CD8 T cells, migratory NK-like T cells, and the activated NK-like T cells (**Fig 1F**). The signature also appeared to overlap strongly with the most differentiated populations as determined by our Monocle3 analysis, indicating an increased likelihood of finding tumor-reactive T cells within these clusters.

Tumor-reactive T cells can be detected among Late Activated and Exhausted T cells

The tumor-infiltrating T cell population likely only contains a fraction of T cells that are tumor-antigen specific. Recent work has shown that tumor-antigen specific T cells can reside in the progenitor exhausted[129] and/or effector and exhausted T cell populations[117,118,126,130-132].

To evaluate whether tumor-specific TCRs can be found within the progenitor exhausted and late activated and exhausted T cell populations in our dataset, we analyzed T cells from these populations from one particular GBM patient (LB3914) who was treated with neoadjuvant anti-PD-1 (Pembrolizumab) and an EGFRvIII Bispecific T cell Engager (BiTE) therapy, and whose tumor we had generated a gliomasphere line from (**Supp Fig 3A**). Bispecific T-cell antibodies are a form of immunotherapy that promote T cell activity by crosslinking T cells with tumor-associated antigens using an engineered antibody that recognizes both the invariant CD3e chain of the TCR and the antigen[133]. In total, this patient had 495 cells in the six T cell clusters described above. Progenitor exhausted cells and Late Act./Exhausted cells represented 23.43% and 37.37% of the T cells, respectively (**Supp Fig 3B**). Again, we examined whether the above gene signature of neoantigen-reactive TCRs from metastatic solid tumors existed within the various T cell subpopulations in this patient. The same three subpopulations as above had a positive score (**Supp Fig 3C**). In addition, the intermediate activated progenitor exhausted CD8 T cells also had a positive score, whereas, previously, when considering all the patient samples in the cohort, that subpopulation did not. Notably, when comparing the signature in the late activated and/or exhausted CD8 T cells in patient LB3914 to the other samples, the neoantigen-reactive TCR signature was significantly higher in patient LB3914, suggesting greater likelihood of finding neoantigen-reactive T cells within that subpopulation in patient LB3914 (**Supp Fig 3D**).

Of these 495 cells, 305 (61.1%) cells had a sequenced TCR detected, representing 120 unique clonotypes, as measured by the CDR3 region on the beta chain. We also analyzed the TCR repertoire of the patient's PBMC collected at: baseline prior to any treatment, twice after a BiTE infusion but prior to anti-PD-1, and on the day of surgery after neoadjuvant anti-PD-1 therapy (**Supp Fig 3A**). Comparing the TCR repertoire of the PBMC at the various time points to the intratumoral clonotypes detected by scTCRseq, we observed overlap between all the time points, indicating some degree of infiltration from the periphery into the tumor (**Supp Fig 4A-D**). This may prove relevant as neoantigen-specific T cells have been detected within the periphery of glioblastoma patients[134].

To being looking for tumor-reactive TCRs based on the transcriptomic signature, we selected TCRs and broadly separated the TCRs into two sets: one set comprising of 26 TCRs containing mostly of TCRs in the late activated and exhausted cluster that were highly expanded in the tumor (Act-TCR) (**Fig 2A, B**) and another set of 17 TCRs containing mostly T cells from the progenitor exhausted cluster(s) (ProgExh-TCR) (**Supp Fig. 5A**).

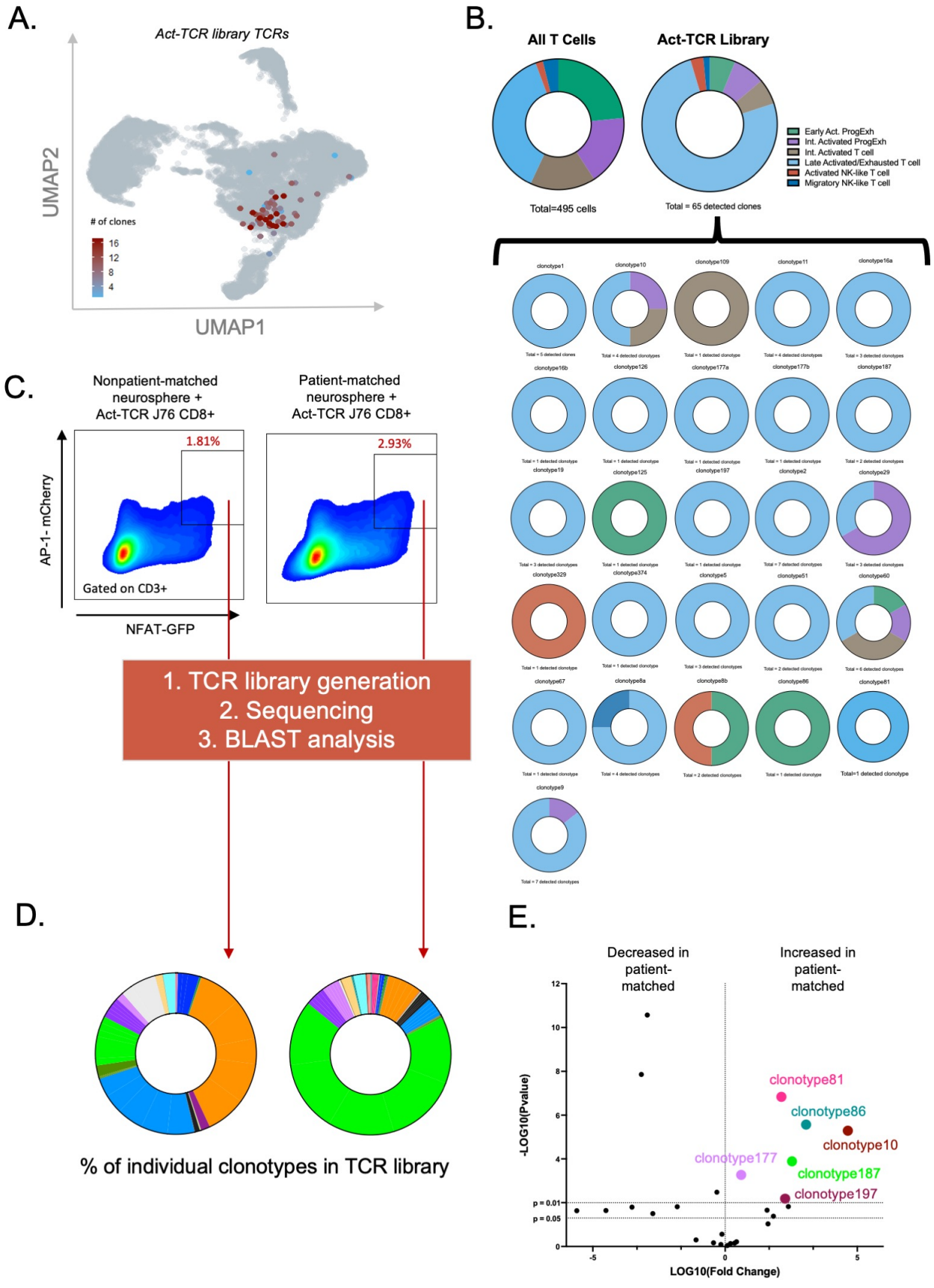
A.
Act-TCR library TCRs
UMAP2
UMAP1
# of clones
16
12
8
4
B.
All T Cells
Act-TCR Library
Early Act. ProgExh
Int. Activated ProgExh
Int. Activated T cell
Late Activated/Exhausted T cell
Activated NK-like T cell
Migratory NK-like T cell
Total=495 cells
Total = 65 detected clones
clonotype1
clonotype10
clonotype109
clonotype11
clonotype16a
clonotype16b
clonotype126
clonotype177a
clonotype177b
clonotype187
clonotype19
clonotype125
clonotype197
clonotype2
clonotype29
clonotype329
clonotype374
clonotype5
clonotype51
clonotype60
clonotype67
clonotype8a
clonotype8b
clonotype86
clonotype81
clonotype9
C.
Nonpatient-matched neurosphere + Act-TCR J76 CD8+
Patient-matched neurosphere + Act-TCR J76 CD8+
1.81%
2.93%
AP-1- mCherry
Gated on CD3+
NFAT-GFP
1. TCR library generation
2. Sequencing
3. BLAST analysis
D.
% of individual clonotypes in TCR library
E.
Decreased in patient-matched
Increased in patient-matched
-LOG10(Pvalue)
LOG10(Fold Change)
p = 0.01
p = 0.05
clonotype81
clonotype86
clonotype10
clonotype177
clonotype187
clonotype197

Figure 2: Identification of Tumor-reactive TCRs in a recurrent GBM patient treated with EGFRvIII Bispecific Antibody and neoadjuvant anti-PD-1 therapy using a triple-reported Jurkat line transduced with a TCR library primarily consisting of TCRs from the late activated / exhausted T cell population

A) UMAP projection showing T cell clone numbers of the TCRs selected in the Act-TCR library

B) Proportion of TCRs within early activated progenitor exhausted, intermediate activated progenitor exhausted, intermediate activated, late activated and/or exhausted CD8, migratory NK-like, and activated NK-like T cell clusters among those six T cell clusters in the 32 patient cohort (top left circle). Proportion of TCRs selected in the Act-TCR library within each of the six T cell clusters from patient LB3914 (top right circle). Each individual TCR selected for the Act-TCR library and the different phenotypes detected for that selected TCR (bottom circles)

C) Flow cytometry data after Act-TCR library transduced J76 Jurkat CD3+ cells were co-cultured with either a patient-matched or non-patient-matched gliomasphere line. Proportion of AP-1-mCherry and NFAT-GFP double positive cells gated on CD3+ cells (red) were used to determine tumor reactivity

D) Proportion of each TCR detected using nucleotide BLAST from sorted AP-1-mCherry and NFAT-GFP cells. Proportion of sorted cells from the non-patient-matched gliomasphere co-culture shown on the left and proportion of sorted cells from the patient-matched gliomasphere co-culture shown on the right

E) *Fold Change Analysis using EdgeR between the detected TCRs from the non-patient-matched co-culture vs. the patient-matched co-culture. TCR clonotypes that showed a significant increase fold change in the patient-matched co-culture (right) are bolded and color-coded to match the colors in (D)*

In order to rapidly clone all of these TCRs, we utilized the PathFinder DNA Assembly platform developed by Rootpath and created two TCR libraries that contained 5 different codon-optimized versions of each TCR in the above sets. We then transduced a triple-reporter CD8+ Jurkat line that expressed CD2, CD28, and CD226[121] with our two TCR libraries and FACs sorted out the transduced population. Next, we co-cultured these transduced cells for 24hrs with the patient-derived gliomasphere line and with an allogeneic, non-HLA-matched gliomasphere line generated from an unrelated patient's tumor. In the T cells transduced with Act-TCR, we detected that 2.93% of CD3+ cells were NFAT-GFP+ and AP-1-mCherry+ compared to 1.81% of NFAT-GFP+, AP-1-mCherry+ CD3+ from T cells co-cultured with the non-patient matched gliomasphere (**Fig 2C**). The signal arising from T cells co-cultured with the non-patient matched gliomasphere likely represents background and/or baseline signal of NFAT-GFP and/or AP-1-mCherry. However, the increase in percentage of this signal within the T cells populations co-cultured with the patient matched gliomasphere indicated the existence of TCRs within the subpool that recognized an antigen presented by the tumor cells. We did not observe an increase in the signal from Jurkat cells transduced with ProgExh-TCR when co-cultured with the patient-matched or non-HLA-matched gliomasphere lines, likely indicating that a tumor-reactive TCR was not present in this TCR library (**Supp Fig. 4B**).

To determine which TCRs from the activated TCR library were tumor-specific, we performed FACS sorting to sort out the NFAT-GFP and AP-1-mCherry positive transduced T cells after co-culture with the patient-matched or non-patient-matched gliomasphere (**Fig 2C**). We generated TCR libraries from the RNA of these sorted cells and performed next generation sequencing. Next, we ran BLAST using a custom database containing the nucleotide sequences of the 5 versions of the 26 clonotypes in Act-TCR. 25 of the 26 of the TCRs in the subpool were detected in varying percentages in the sorted population from patient-matched co-culture (**Fig 2D**) To calculate the fold change in TCR abundance represented in the TCR libraries generated

from the patient-matched co-culture versus the non-patient-matched co-culture, we utilized the differential expressional analysis package edgeR[135-137]. Six clonotypes showed a significant increased fold change in the patient-matched co-culture compared to the non-patient-matched co-culture: clonotypes 10, 81, 86, 177, 187, and 197 (**Fig 2E**).

Therefore, by utilizing a combinatory approach utilizing in silico gene expression and in vitro techniques, we could filter for candidate tumor-reactive TCRs out of all detected TCRs.

Discussion

Glioblastoma (GBM) remains a difficult to treat tumor and efforts to treat this malignancy using conventional therapies and immunotherapies have largely remained ineffective. One potential reason for the failure of immunotherapy in the glioblastoma setting is its immunologically "cold" state, characterized by a lack of tumor-infiltrating T cells. Our previous work has shown that using neoadjuvant anti-PD-1 therapy is able to increase T cell infiltration and/or expansion in the GBM tumor microenvironment. However, identifying and separating out tumor-reactive T cells from bystander T cells within the microenvironment introduces additional hurdles.

Advances and the increasing availability of single-cell technologies have made it possible to study the transcriptomics of cells, including tumor-infiltrating T cells in GBMs and other cancer types. In this study, we utilized single-cell RNA and TCRsequencing to narrow down all detected TCRs into a list of candidate TCRs that may be tumor-reactive based on the transcriptomic signature of these cells and their expansion within the tumor microenvironment. We utilized the PathFinder DNA Assembly platform developed by Rootpath to rapidly generate TCR libraries containing our candidate TCRs to transduce into a triple-reporter Jurkat system. We co-cultured the transduced Jurkats with a patient-matched gliomasphere line and TCRs

from the activated cells, representing potential tumor-reactive cells, were sorted out and sequenced. Using this methodology, we isolated a handful of higher confident candidate tumor-reactive TCRs from the much larger pool of tumor-infiltrating T cell population (**Fig 3**).

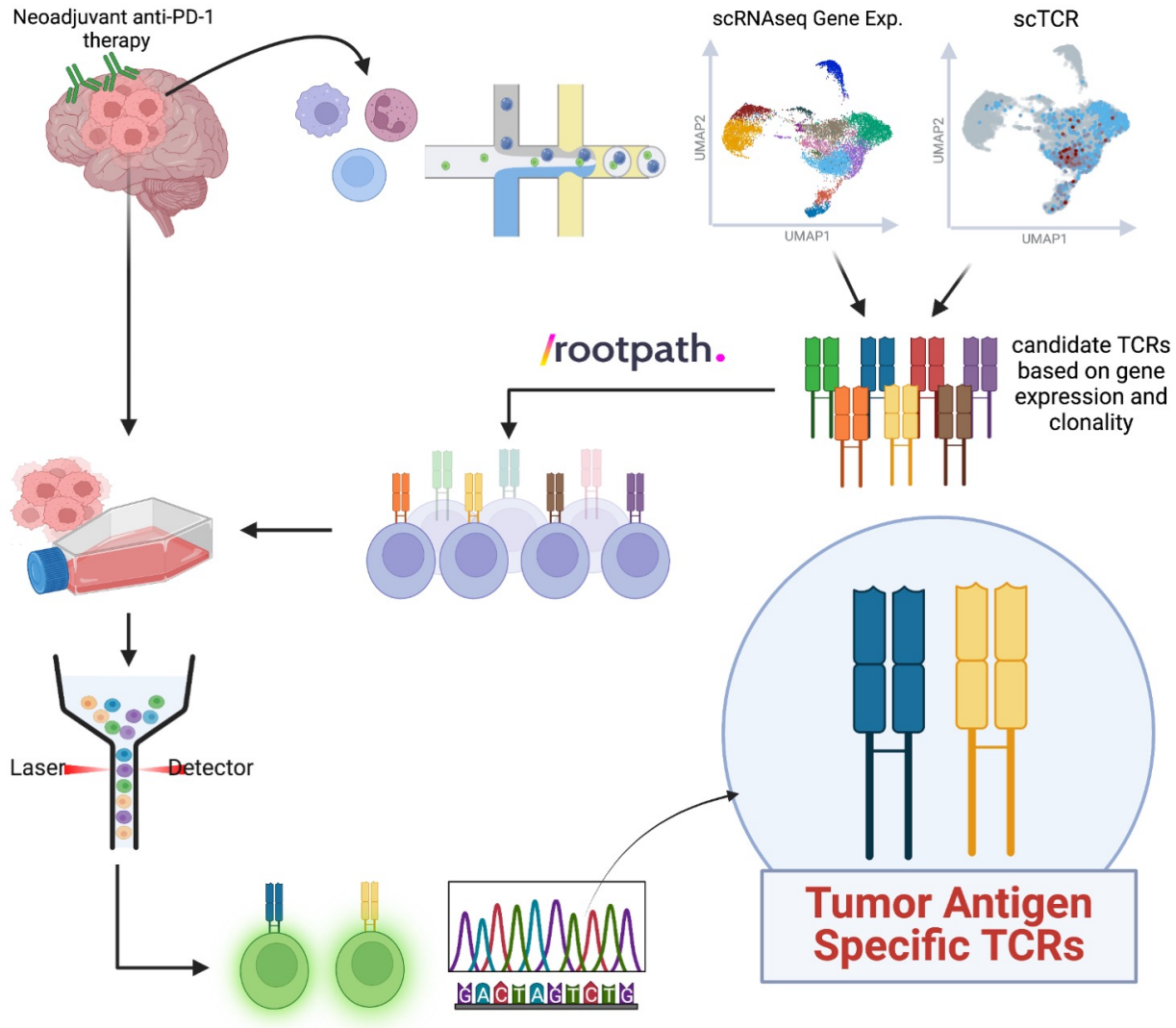

Figure 3: Schematic of a workflow for how tumor antigen specific TCRs may be detected using single-cell RNAseq and TCRseq in recurrent GBM patients treated with neoadjuvant anti-PD-1 therapy

Created with BioRender.com

Detecting neoantigen-reactive TCRs has typically involved sequencing tumors and looking for tumor-associated mutations that may give rise to targetable neoantigens. Candidate neoantigens can then be incorporated into minigenes or used in Class I MHC:tetramer technologies to discover and isolate neoantigen reactive TCR. This approach has worked to discover relevant tumor-reactive T cells, but hurdles to this approach include: the relative low number of non-synonymous mutations capable of generating quality neoantigens in the GBM setting[138,139], the need to improve the accuracy of variant calling pipelines[140], isolating insufficient number of T cell to interrogate candidate neoantigens due to GBM's being an immunologically cold tumor, and the length of time and financial cost needed to isolate neoantigen reactive TCRs. As such, pursuing additional strategies to this approach, may be necessary. Analyzing the paired transcriptomic and TCR signature of TILs, even while remaining agnostic towards which neoantigens these T cells may recognize, may be an additional approach to expand the potential pool of candidate tumor-reactive TCRs that can be tested and used for therapy and/or that can be used to more quickly interrogate candidate neoantigens discovered using various in silico techniques.

Adoptive T cell transfer using autologous TILs or TCR-engineered T cells has proven to be effective at treating other cancer types[141-143], though the results and effectiveness in gliomas remains more limited[144]. One reason for the relative lack of success compared to other cancer types may be due to the low density of TILs in glioblastoma setting. Additionally, the amount of time and resources needed to expand out ex vivo a significant number of T cells to deliver into the patient, many of which may not actually be tumor-reactive, may not be feasible in the recurrent setting. By using transcriptomic signatures of T cell populations that are more likely to contain tumor-reactive T cells, relevant TCRs may be more readily identified from low numbers of isolated TILs without needing to undergo the typical expansion and testing steps of autologous TIL therapy. These TCRs may then be transduced into more stem-like T cells and

delivered into the patient, as these “younger” cells have been seen to be more effective in adoptive cell transfer therapies[145]. By incorporating new arising technologies like the PathFinder DNA Assembly platform from Rootpath, the timeline from surgery to infusion of T cell products may be further decreased in GBMs, which is necessary due to the rapid progression of recurrent GBMs.

This study provides a proof-of-concept for how paired single-cell transcriptomic and TCR sequencing can be potentially used to treat patients with recurrent GBM. Although the findings of this study need to be expanded to include additional patients, we hope that this study may provide a framework for how to pursue these type of studies in the future and eventually lead to better treatment for patients with recurrent GBMs using immunotherapy.

Methods

Ethical Compliance

Research conducted in this study complied with all relevant ethical regulations.
The UCLA Medical Institutional Review Board 2 (IRB#10-000655-AM-00059) approved all protocols related to patient specimen collection.

Patient Tissue Collection and Single cell isolation

Tumor tissue was obtained from patients undergoing surgery at the University of California, Los Angeles. All patients provided written informed consent. This study was conducted in accordance with the Declaration of Helsinki and under an institutional review board approved protocol. All GBM patients were treated with standard of care therapies. Patients with surgically accessible recurrent GBMs, regardless of recurrence number and who did not show response to standard of care treatment and had tumor progression, were treated with off-label, off-trial pembrolizumab 200 mg by intravenous infusion 14 +/- 5 days before surgery, similar to our previously published study[59].
For the patient who received the EGFRvIII BiTE therapy, for cycle 1, week 1, the patient was administered an augmented dose of 1500ug/day. Cycle 2 was administered at a lower dose of 15ug/day due to an observed decrease in tumor burden via MRI. However, the post-cycle 2 MRI showed an increase in tumor size. On the basis that the observed drug exposure in the patient's serum during treatment at 1500ug/day matched the predicted potential efficacious exposure level and resulted in decrease in tumor burden, the patient resumed high dose treatment for Cycles 3 and 4 before being removed from the trial due to the emergence of new tumor lesions. Based on a survival benefit in the setting of neoadjuvant pembrolizumab, the patient was treated with one dose of neoadjuvant pembrolizumab 200mg IV, followed by cytoreductive

surgery of two foci of tumor—the initial site as well a deeper lesion along the white matter of the parietal lobe—and then continued adjuvant pembrolizumab every 3 weeks.

Tumor-infiltrating CD45+ cells were labeled with CD45+ microbeads (Miltenyi Biotec, cat. 130-045-801) and positively selected for from tumor tissue digested using the Miltenyi Brain Tumor Dissociation kit (Miltenyi Biotec, cat. 130-095-42) and gentleMACS dissociator (Miltenyi Biotec, cat. 130-093-235). After isolation, the collected CD45's were frozen and stored in liquid nitrogen.

Single-cell RNA sequencing

Single-cell sequencing was performed on a Novaseq6000 S2 2x50bp flow cell (Illumina) utilizing the Chromium single-cell 3' or 5′ gene expression library preparation (10X Genomics), per manufacturer's protocol at the Technology Center for Genomics and Bioinformatics Core, UCLA. Data was demultiplexed and aligned with Cell Ranger version 7.0.1 (10X Genomics) and aligned to the Genome Reference Consortium Human Build 38 (GRCh38).

Data was analyzed with the Seurat R package, version 4.2.0, and following a standard Seurat workflow. Briefly, for quality assurance, cells with >20% mitochondrial RNA and fewer than 200 number of features were excluded from further analysis. Raw transcript count for each sample was individually normalized using the NormalizeData function. After quality control, a Seurat data object for each patients' cells was generated and all cells were integrated into one large Seurat object. The expression values of this larger object was scaled by regressing out the percent mitochondrial features, cell cycle score[111], and the number of detected genes. For dimension reduction was performed using a principal component analysis and uniform manifold approximation and projection (UMAP). Different cell cluster populations were defined using the FindNeighbors function and the genes that were differentially expressed in each cluster or treatment was computed using the FindAllMarkers function.

T cell receptor analysis

For overlaying clonotype information on the UMAP project, cells with the same TCRβ sequence were considered as one TCR clone and an expanded clone were clones with at least two cells in the sample set. Single T-cell Analysis by Rna-seq and Tcr TRACking (STARTRAC) version 0.1.0 was used to estimate the amount of clonal expansion in each T cell cluster (STARTRAC-expa index) and to estimate the likelihood of two cell populations to share clones (STARTRAC-tran index).

For samples submitted to Adaptive Technologies for T-cell receptor (TCR) V-b CDR3 region using high-throughput sequencing, we extracted genomic DNA from the patient PBMCs collected at different time points using DNeasy Blood & Tissue Kit (Qiagen catalog no. 69504).

Transfection and Transduction with Rootpath generated TCR libraries

The alpha and beta chain sequences of the selected TCRs from the chosen clusters were given to Rootpath to be made into TCR libraries using their proprietary PathFinder DNA Assembly platform. Libraries were returned as Lentiviral plasmids and transfected into 293T cells

We received Lentiviral plasmids from Rootpath and transfected 293T cells using the TransIT-293 Transfection Reagent (Mirus, cat. Mir-2704) and the PAX2 (gag/pol) and MD2.G (VSVg) packaging plasmids in D10 media (DMEM plus 10% Heat-inactivated, endotoxin-free fetal bovine serum). After 16 hours, the cell media was replaced with D10 media containing 10mM Sodium Butyrate and 20mM HEPES for 6-8 hours before being replaced with D10 media containing only 20mM HEPES. After 16-20 hours, the resulting supernatant containing the viral particles was pooled together, filtered, and mixed with Lenti-X Concentrator (Takara, cat. 631231) at a 3:1 ratio for 24 hours at 4°C. The concentrated virus was spun down and the resulting pellet was resuspended in 1/10 to 1/100 of the original volume of media using D10 media and stored at -80°C

To transduce the triple reporter J76 Jurkat line, 100ul of concentrated virus and 2ug of polybrene were added to 400,000 Jurkat cells in a 48 well plate and spun at 37°C at 1000G for 90 minutes. Cells were cultured and expanded in IMDM media (ThermoFisher, cat. 12440053) at a concentration of 600,000 cells/mL. For sorting the transduced populations, since the libraries contained a truncated CD19 antigen, an anti-CD19 antibody conjugated to APC-Cy7 (1:40, Biolegend, cat. 302218) was used to stain the cells and cells were sorted using a FACSAria at the UCLA Flow Cytometry Core Facility.

Co-culture System

Gliomaspheres were generated and expanded following a published workflow[146]. Gliomaspheres were expanded in DMEM/F12 (ThermoFisher, cat. 11330057) supplemented with B27 Supplement without Vitamin A (50x) (ThermoFisher, cat. 12587010), 100x Glutamax (ThermoFisher, cat. 35050-061), and 100x Pen-Strep-Glut (ThermoFisher, cat 15140122) and with a 400x HEF mixture containing 50ng/mL Human EGF Recombinant Protein (ThermoFisher, cat. PHG0313), 20ng/mL Human FGFb (ThermoFisher, cat. PHG0263) and 5ug/mL Heparin. Cells were cultured at 100,000 cells/mL and split every 7-10 days and the HEF mixture was added every 5-7 days.

Prior to co-culturing, gliomasphere lines were disassociated using TrypLE (ThermoFisher, cat 12605028) and treated with 250IU/mL human IFN-γ (Sigma Aldrich, cat. 11040596001) for 24 hours. Gliomasphere and transduced J76 Jurkat cells were co-cultured at a 1:1 ratio in IMDM media for 24 hours. Additionally, a separate culture of transduced J76 Jurkat cells were treated with 50 ng/mL OKT3 anti-CD3 antibody (Biolegend, cat. 317304) and 1ug/mL anti-CD28 antibody (BD Biosciences, cat. 555725) as a positive control for gating purposes. Cells were stained with an anti-CD3 antibody conjugated to PE-Cy7 (1:40, BioLegend, cat. 317318) and

antibodies conjugated to FITC (BioLegend, cat. 344703), Brilliant Violet 510 (BioLegend, cat. 344731), and PE/Dazzle 594 (BioLegend, cat. 130213) were used for compensation for GFP, CFP, and mCherry, respectively.

CD3+ GFP+ mCherry+ cells were sorted out of the co-culture system using a FACSAria and RNA from these sorted populations was extracted using the PureLink RNA Mini Kit (ThermoFisher, cat. 12183018A).

DNA Library generation and next generation sequencing.

Extracted RNA from the sorted T cell populations was reversed transcribed into cDNA using the Invitrogen superscript IV Reverse Transcriptase (SSIV) Kit (ThermoFisher, cat. 18090200) and a primer recognizing the codon-optimized TCR-beta constant region and the following PCR protocol: (1) 50°C for 20min, (2) 80°C for 10min, (3) 4°C forever. Immediately after the completion of the reverse transcription step, second strand synthesis and UMI appending was performed using the Q5 Hot Start High-Fidelity DNA Polymerase (NEB, cat. M0493S) and using the following PCR protocol: (1) 98°C for 30 sec, (2) 98°C for 10 sec, (3) 62°C for 30 sec, (4) 72°C for 3min, and (5) 10°C forever. The resulting PCR product was purified using the AMPure XP Reagent (Beckman Coulter, cat. A63880). Next, qPCR was performed to determine the optimal cycle number for amplifying the PCR product and once the cycle number determined, the PCR product was appended with R2 and amplified with the following protocol: (1) 98°C for 30 sec, (2) 98°C for 10 sec, (3) 66°C for 30 sec, (4) 72°C for 30 sec, return to step 2 for the optimal number of cycles, (5) 72°C for 3 min, and (6) 10°C forever. Again, after this step, the resulting amplified PCR product was purified using the AMPure XP Reagent. Finally, the P5 and P7 indexes were added to the PCR product using the following protocol: (1) 98°C for 30 sec, (2) 98°C for 10 sec, (3) 61°C for 30 sec, (4) 72°C for 30 sec, return to step 2 for 12 cycles,

(5) 72°C for 3 min, and (6) 10°C forever. For a final time, the resulting indexed PCR product was purified using the AMPure XP Reagent.

Sequencing was performed on a Novaseq SP 2x150bp flow cell (Illumina). Fastq files were preprocessed using Trimmomatic[147], using sliding window trimming with a window size of 4. A local NCBI Blast[148] nucleotide search was conducted against a custom BLAST database of the supplied TCR sequences to Rootpath.

Statistics and Reproducibility

The statistical tests used to calculate the P-values are indicated in respective figures. Statistical analysis of the data presented in the violin plots was done using GraphPad Prism version 8.4.0.

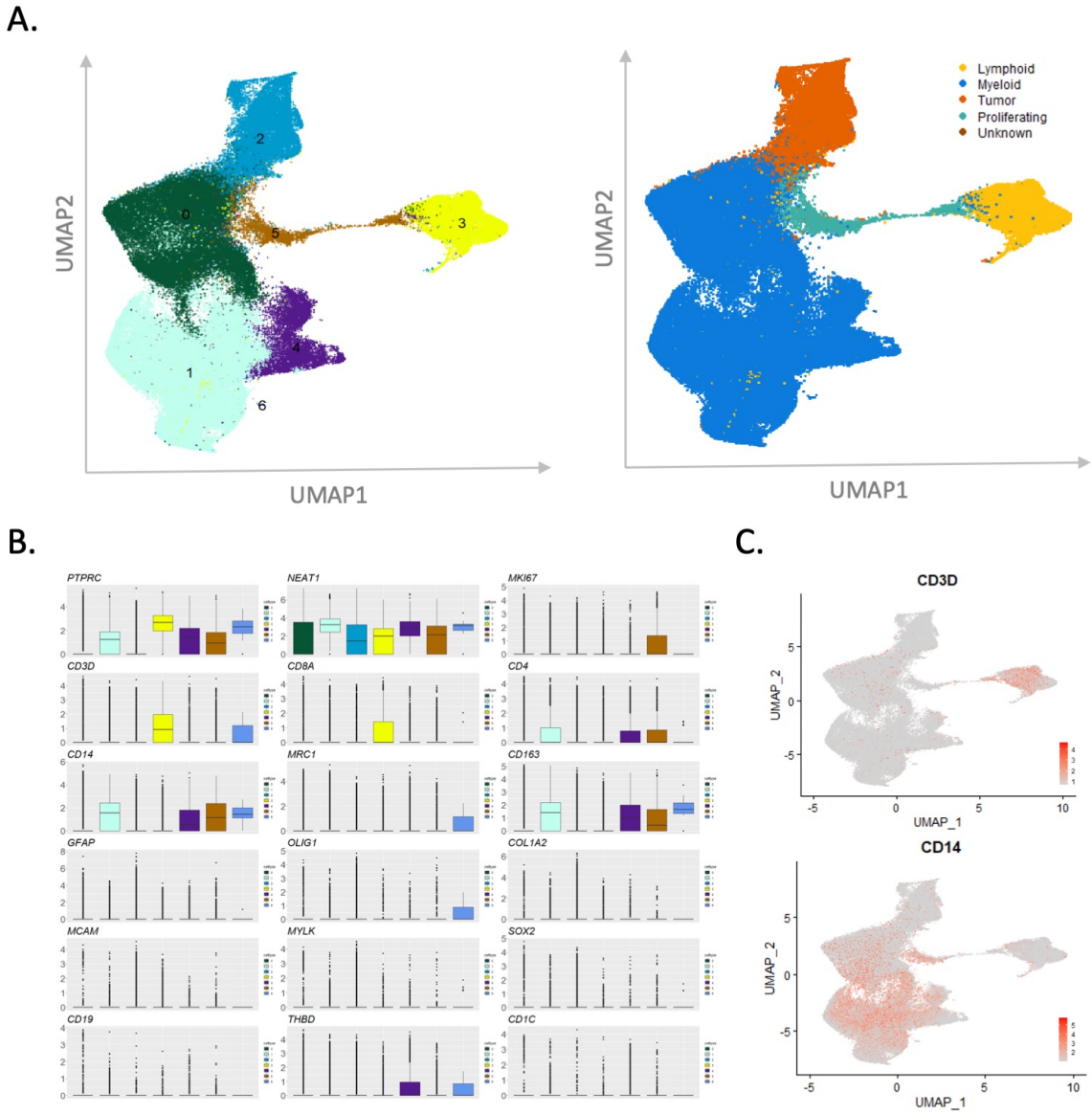

Supp Fig 1: Single-cell Gene Expression analysis on all tumor-infiltrating CD45+ cells in the cohort of 32 recurrent glioblastoma patients

A) A UMAP projection of CD45+ tumor-infiltrating cells analyzed with scRNAseq (n = 145,113 cells, 14 GBM.rec, 18 GBM.pembro). Left projection shows cluster information and the right projection shows cell type classification based transcriptomic data

B) Expression of selected genes in each classified cell clusters derived from the scRNAseq data

C) *UMAP plots of CD3D and CD14 expression on the CD45+ tumor-infiltrating cells*

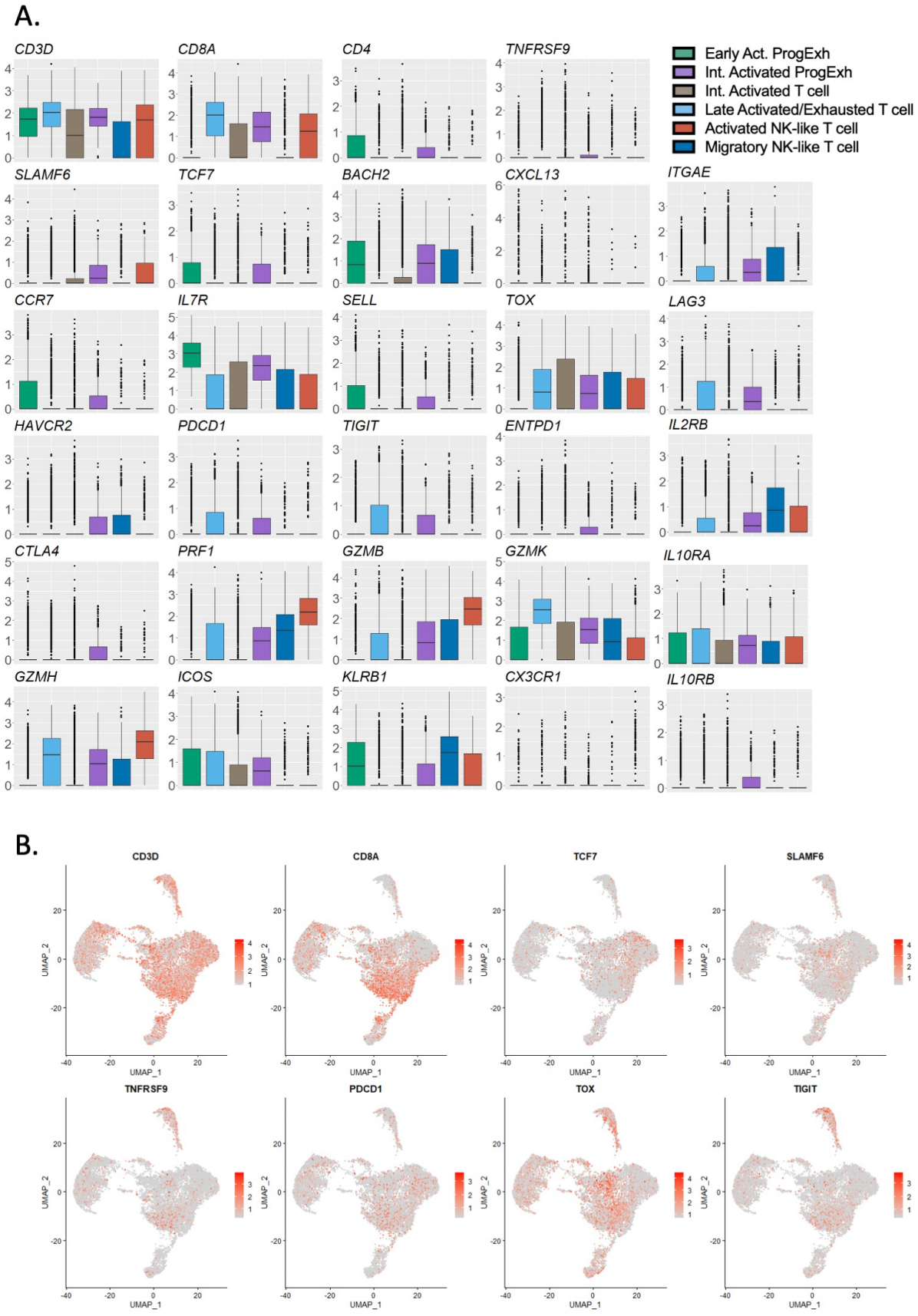
A.
CD3D
CD8A
CD4
TNFRSF9
Early Act. ProgExh
Int. Activated ProgExh
Int. Activated T cell
Late Activated/Exhausted T cell
Activated NK-like T cell
Migratory NK-like T cell
SLAMF6
TCF7
BACH2
CXCL13
ITGAE
CCR7
IL7R
SELL
TOX
LAG3
HAVCR2
PDCD1
TIGIT
ENTPD1
IL2RB
CTLA4
PRF1
GZMB
GZMK
IL10RA
GZMH
ICOS
KLRB1
CX3CR1
IL10RB
B.
CD3D
CD8A
TCF7
SLAMF6
TNFRSF9
PDCD1
TOX
TIGIT
UMAP_1
UMAP_2

Supp Fig 2: Single-cell RNAseq on CD3+ lymphoid cells

A) Expression of selected genes across early activated progenitor exhausted, intermediate activated progenitor exhausted, intermediate activated, late activated and/or exhausted CD8, migratory NK-like, and activated NK-like T cell clusters

B) UMAP plots of the expression of selected genes across CD3+ lymphoid cells

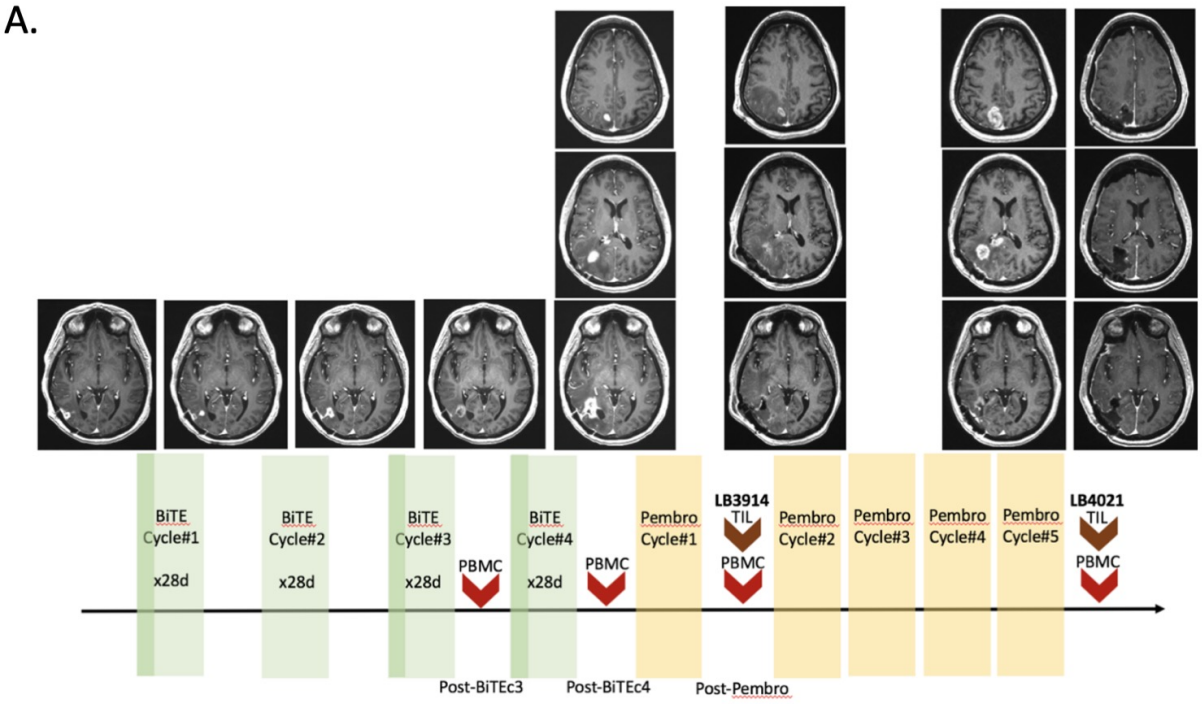
A.
BiTE Cycle#1 x28d
BiTE Cycle#2 x28d
BiTE Cycle#3 x28d
PBMC
BiTE Cycle#4 x28d
PBMC
Pembro Cycle#1
LB3914 TIL
PBMC
Pembro Cycle#2
Pembro Cycle#3
Pembro Cycle#4
Pembro Cycle#5
LB4021 TIL
PBMC
Post-BiTEc3
Post-BiTEc4
Post-Pembro

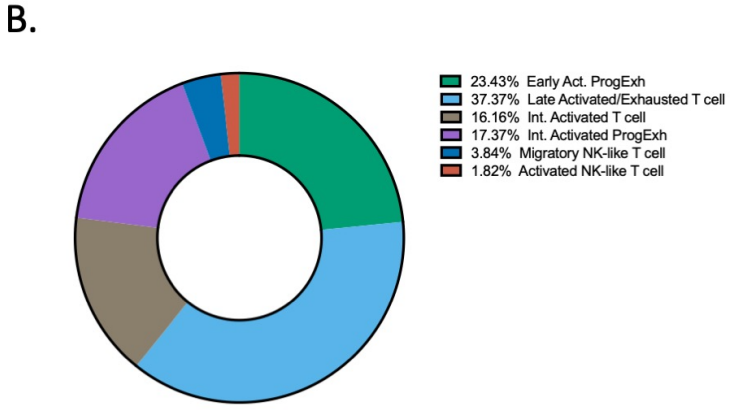
B.
23.43% Early Act. ProgExh
37.37% Late Activated/Exhausted T cell
16.16% Int. Activated T cell
17.37% Int. Activated ProgExh
3.84% Migratory NK-like T cell
1.82% Activated NK-like T cell

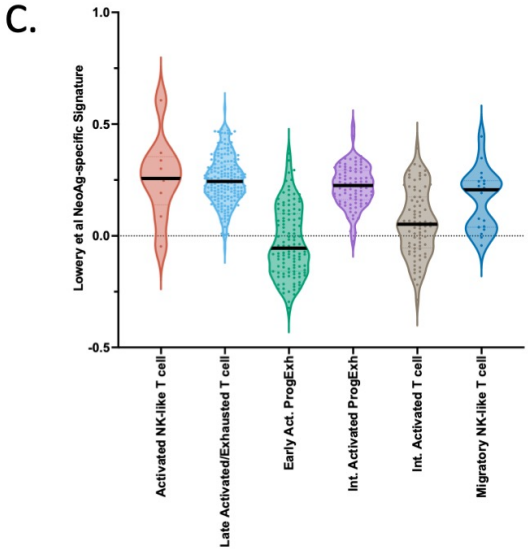
C.
Lowery et al NeoAg-specific Signature
1.0
0.5
0.0
-0.5
Activated NK-like T cell
Late Activated/Exhausted T cell
Early Act. ProgExh
Int. Activated ProgExh
Int. Activated T cell
Migratory NK-like T cell

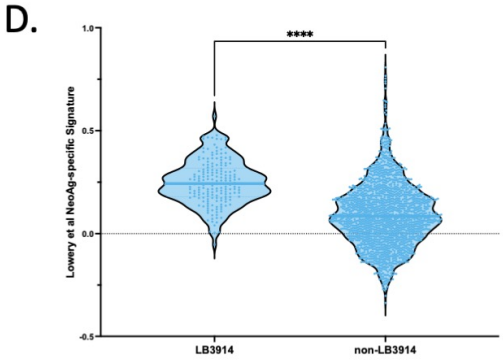
D.
****
Lowery et al NeoAg-specific Signature
1.0
0.5
0.0
-0.5
LB3914
non-LB3914

Supp Figure 3: Characteristics of a recurrent glioblastoma patient (LB3914) treated with EGFRvIII Bispecific T cell Engager (BiTE) and neoadjuvant anti-PD-1 therapies

A) Schematic of the treatment history for patient LB3914

B) Proportion of early activated progenitor exhausted, intermediate activated progenitor exhausted, intermediate activated, late activated and/or exhausted CD8, migratory NK-like, and activated NK-like T cell clusters among those six T cell clusters in patient LB3914

C) Neoantigen-reactive T cell score from Lowery F., et. al (2021) in the six T cell clusters from patient LB3914

D) Comparison of the Neoantigen-reactive T cell score from Lowery F., et. al (2021) in the Late Act. / Exhausted T cell cluster from patient LB3914 to the score of the same population in all the other patients in the cohort. P values were calculated using a two-sided Wilcoxon rank sum test

A.

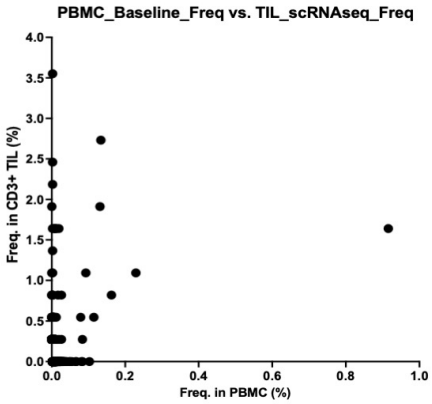
PBMC_Baseline_Freq vs. TIL_scRNAseq_Freq
Freq. in CD3+ TIL (%)
Freq. in PBMC (%)
0.0
0.5
1.0
1.5
2.0
2.5
3.0
3.5
4.0
0.0
0.2
0.4
0.6
0.8
1.0

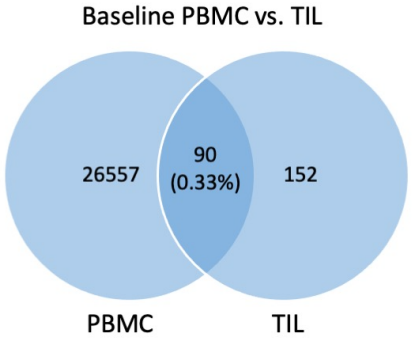
Baseline PBMC vs. TIL
26557
90
(0.33%)
152
PBMC
TIL

B.

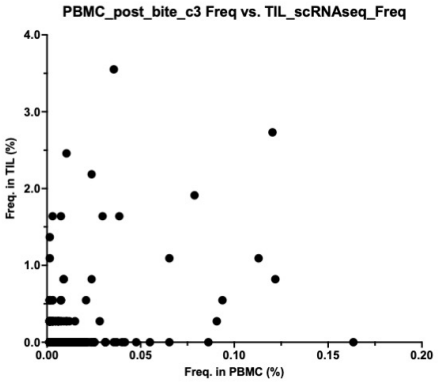
PBMC_post_bite_c3 Freq vs. TIL_scRNAseq_Freq
Freq. in TIL (%)
Freq. in PBMC (%)
0.0
1.0
2.0
3.0
4.0
0.00
0.05
0.10
0.15
0.20

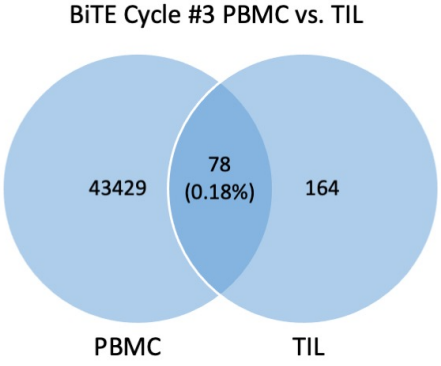
BiTE Cycle #3 PBMC vs. TIL
43429
78
(0.18%)
164
PBMC
TIL

C.

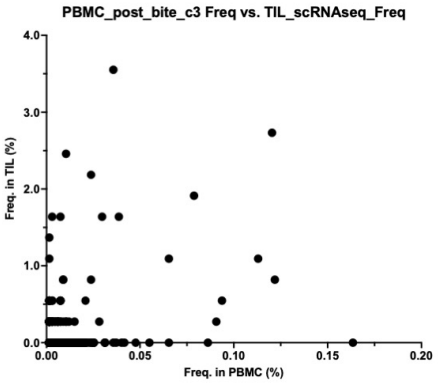
PBMC_post_bite_c3 Freq vs. TIL_scRNAseq_Freq
Freq. in TIL (%)
Freq. in PBMC (%)
0.0
1.0
2.0
3.0
4.0
0.00
0.05
0.10
0.15
0.20

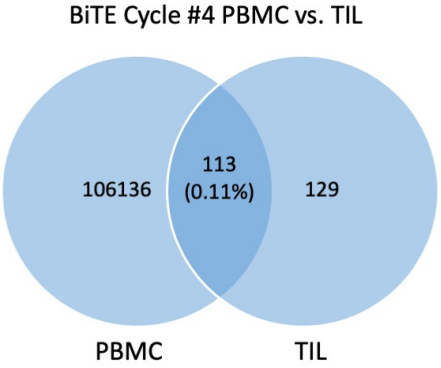
BiTE Cycle #4 PBMC vs. TIL
106136
113
(0.11%)
129
PBMC
TIL

D.

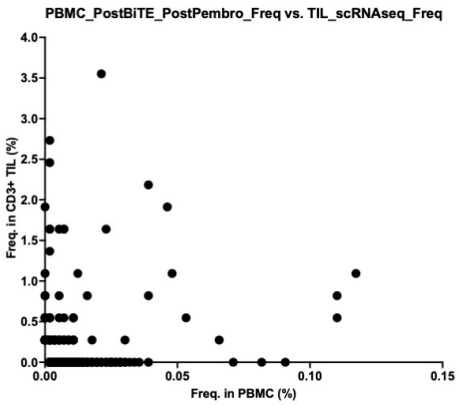
PBMC_PostBiTE_PostPembro_Freq vs. TIL_scRNAseq_Freq
Freq. in CD3+ TIL (%)
Freq. in PBMC (%)
0.0
0.5
1.0
1.5
2.0
2.5
3.0
3.5
4.0
0.00
0.05
0.10
0.15

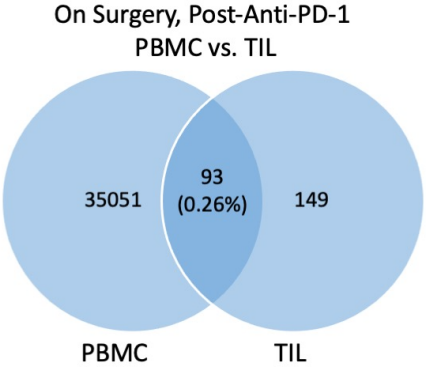
On Surgery, Post-Anti-PD-1
PBMC vs. TIL
35051
93
(0.26%)
149
PBMC
TIL

Supp Figure 4: The overlap of detected TCRs from tumor infiltrating T cells using scTCRseq and detected peripheral TCRs from PBMC collected at various time points using Adaptive Technologies ImmunoSeq platform

A) Baseline PBMC. Each dot represents a unique TCR clone. X-axis indicates the frequency among all detected TCRs in PBMCs. Y-axis indicates the frequency among all detected TCRs in from tumor infiltrating T cells

B) after BiTE cycle #3 PBMC

C) after BiTE cycle #4 PBMC

D) after anti-PD-1 therapy/on day of surgery PBMC

A.

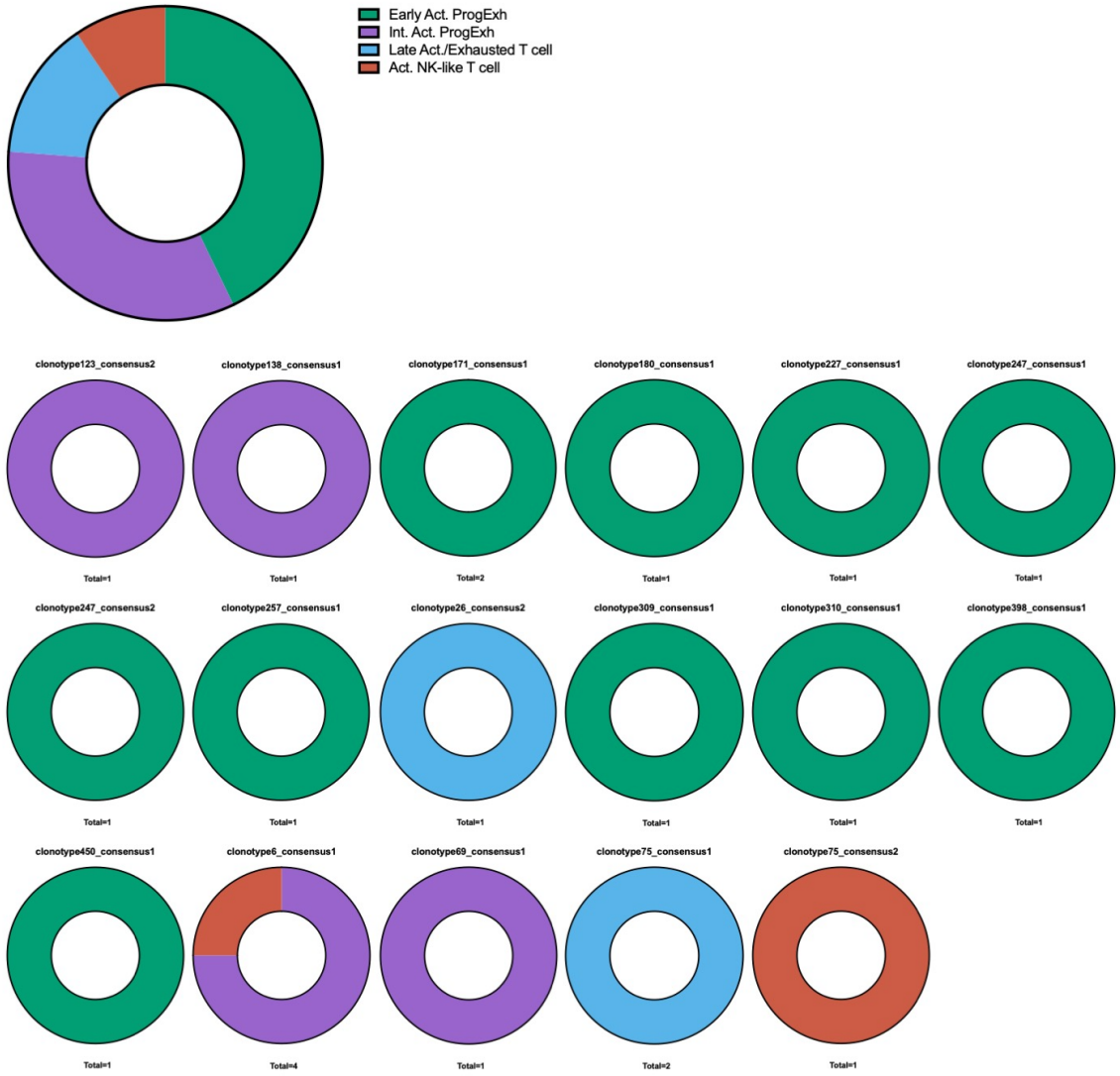
Early Act. ProgExh
Int. Act. ProgExh
Late Act./Exhausted T cell
Act. NK-like T cell
clonotype123_consensus2
clonotype138_consensus1
clonotype171_consensus1
clonotype180_consensus1
clonotype227_consensus1
clonotype247_consensus1
Total=1
Total=1
Total=2
Total=1
Total=1
Total=1
clonotype247_consensus2
clonotype257_consensus1
clonotype26_consensus2
clonotype309_consensus1
clonotype310_consensus1
clonotype398_consensus1
Total=1
Total=1
Total=1
Total=1
Total=1
Total=1
clonotype450_consensus1
clonotype6_consensus1
clonotype69_consensus1
clonotype75_consensus1
clonotype75_consensus2
Total=1
Total=4
Total=1
Total=2
Total=1

B.

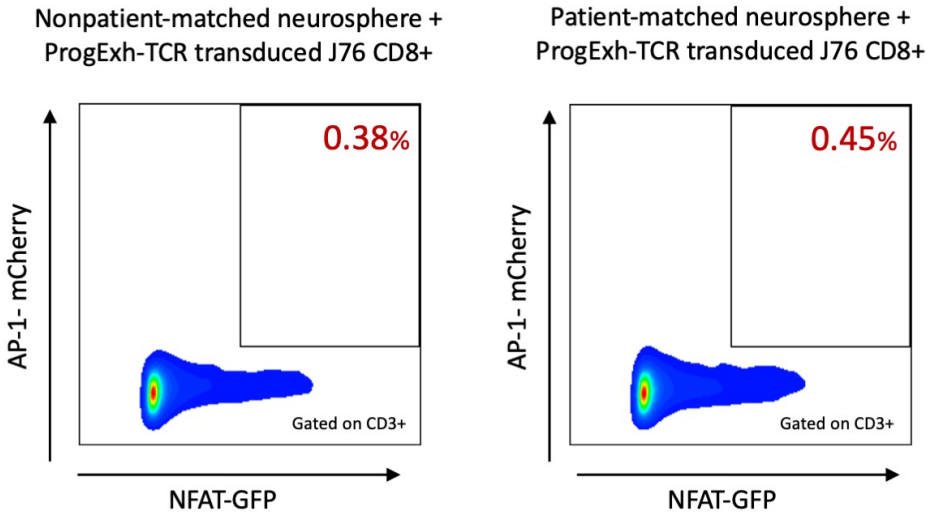
Nonpatient-matched neurosphere +
ProgExh-TCR transduced J76 CD8+
0.38%
AP-1- mCherry
Gated on CD3+
NFAT-GFP
Patient-matched neurosphere +
ProgExh-TCR transduced J76 CD8+
0.45%
AP-1- mCherry
Gated on CD3+
NFAT-GFP

Supp Figure 5: ProgExh-TCR library primarily consisting of TCRs detected in the progenitor exhausted T cell clusters

A) Proportion of TCRs in the ProgExh-TCR library across the six T cell clusters (top). Each individual TCR selected for the library and the different phenotypes detected for that selected TCR (bottom)

B) Flow cytometry data after ProgExh-TCR library transduced J76 Jurkat CD3+ cells were co-cultured with either a patient-matched or non-patient-matched gliomasphere line. Proportion of AP-1-mCherry and NFAT-GFP double positive cells (red) were used to determine tumor reactivity

CONCLUSION:

Glioblastomas remain an incurable disease with little improvement in patient outcomes in the past several decades. Therefore, new therapeutic options need to be identified and developed for this malignancy. Despite the successes enjoyed by other cancer types, immunotherapy, in particular checkpoint inhibition, against GBMs has proven mostly ineffective, thus highlighting a current knowledge gap for how to translate the successes found in other cancers into the GBM context.

In this work, we sought to understand the how one immunotherapeutic treatment strategy – neoadjuvant anti-PD-1 therapy – changes the immune composition within the GBM tumor microenvironment and affects the intratumoral and peripheral T cell compartments. By leveraging single-cell technologies, we characterized PD-1 expressing T cells within the periphery and within the tumor, and we found that neoadjuvant anti-PD-1 increases the infiltration and expansion of intratumoral T cells, some of which are tumor-reactive. However, changes to the myeloid compartment by this therapy dampens the effectiveness of neoadjuvant anti-PD-1 as a monotherapy.

Although neoadjuvant anti-PD-1 therapy is not curative in the GBM context, our published phase I clinical trial showed survival benefit[59] and the data from that trial, along with the findings presented in this study, indicate that the changes brought forth from this therapy may create new opportunities to improve patient outcomes with other forms of therapy when used in combination with neoadjuvant anti-PD-1 therapy. For instance, based on the findings from the above mentioned study, further improving the T cell infiltration and activity within the GBM tumor microenvironment can have a beneficial effect. As such our group initiated a Phase I clinical trial (NCT04201873) investigating the combination treatment of neoadjuvant anti-PD-1 therapy with Dendritic Cell Tumor Cell Lysate Vaccine, which has shown to improve patient survival[149] and increases T cell trafficking to the tumor[17]. Likewise, as mentioned in the discussion in

Chapter 2 of this work, our group is currently conducting a Phase 1b trial assessing the effectiveness of neoadjuvant anti-PD-1 therapy with or without anti-CTLA-4 therapy (NCT04606316).

As technologies develop and improve, we anticipate that using spatial transcriptomic platforms, such as the Visium Spatial Gene Expression (10X Genomics), Hyperion Imaging System for imaging mass cytometry[150] (Fluidigm), or the recently developed Slide-TCR-seq[151], or single cell sequencing platforms that simultaneously measure the proteome and transcriptomes of cells, such as the CITE-Seq (Illumina), can further augment the characterization of the tumor microenvironment and lead to the discovery of additional mechanisms for how GBMs negate the effects of neoadjuvant anti-PD-1 therapies. Additionally, translating the increasing wealth of data and the conclusions generated by high dimensional analysis into suitable therapeutic strategies that fit within the treatment window of GBMs and are tolerable for patients is of essential importance. As such, technologies such as the PathFinder DNA Assembly technology from Rootpath that can rapidly incorporate sequencing data into the development of biologics can potentially meet current demands for safe and quickly accessible therapies for these patients.

One present limitation of the study is the focus on the immune compartment within the glioblastoma microenvironment without deeper exploration for the transcriptional changes in tumors cells due to neoadjuvant anti-PD-1 therapies. Due to the paucity of infiltrating T cells and limits to the number of analyzable cells per sample using single-cell RNAseq, simultaneously studying the immune and tumor compartment would not have yielded as robust analysis into the tumor infiltrating immune compartment. Nevertheless, the effects of neoadjuvant anti-PD-1 inevitably changes tumors cells and leads to new resistance mechanisms that render anti-PD-1 therapies to be less effective, as has been seen in other cancer types[152]. Future studies that examine the dynamics in tumor cell to immune cell interactions and how these dynamics change mechanistically with neoadjuvant anti-PD-1

therapies will be needed to develop a more complete picture of the GBM tumor microenvironment.

Taken all together, while the challenges to treating GBMs with neoadjuvant anti-PD-1 and other immunotherapies remain, our understanding of how these therapies work in the GBM context is rapidly growing with the increased accessibility and improvement in various technologies. Therefore, neoadjuvant anti-PD-1 and other immunotherapies represent an exciting opportunity to improve our current strategies at treating GBMs and will hopefully lead to better patient outcomes.

BIBLIOGRAPHY

1. Tamimi, A.F. & Juweid, M. Epidemiology and Outcome of Glioblastoma. in *Glioblastoma* (ed. De Vleeschouwer, S.) (Brisbane (AU), 2017).
2. Noch, E.K., Ramakrishna, R. & Magge, R. Challenges in the Treatment of Glioblastoma: Multisystem Mechanisms of Therapeutic Resistance. *World Neurosurg* **116**, 505-517 (2018).
3. Ribas, A. & Wolchok, J.D. Cancer immunotherapy using checkpoint blockade. *Science* **359**, 1350-1355 (2018).
4. Gong, J., Chehrazi-Raffle, A., Reddi, S. & Salgia, R. Development of PD-1 and PD-L1 inhibitors as a form of cancer immunotherapy: a comprehensive review of registration trials and future considerations. *J Immunother Cancer* **6**, 8 (2018).
5. Reardon, D.A.*, et al.* Effect of Nivolumab vs Bevacizumab in Patients With Recurrent Glioblastoma: The CheckMate 143 Phase 3 Randomized Clinical Trial. *JAMA Oncol* **6**, 1003-1010 (2020).
6. Nayak, L.*, et al.* Randomized Phase II and Biomarker Study of Pembrolizumab plus Bevacizumab versus Pembrolizumab Alone for Patients with Recurrent Glioblastoma. *Clin Cancer Res* **27**, 1048-1057 (2021).
7. de Groot, J.*, et al.* Window-of-opportunity clinical trial of pembrolizumab in patients with recurrent glioblastoma reveals predominance of immune-suppressive macrophages. *Neuro Oncol* **22**, 539-549 (2020).
8. Chuntova, P.*, et al.* Unique challenges for glioblastoma immunotherapy-discussions across neuro-oncology and non-neuro-oncology experts in cancer immunology. Meeting

Report from the 2019 SNO Immuno-Oncology Think Tank. *Neuro Oncol* **23**, 356-375 (2021).

9. Brown, C.E.*, et al.* The future of cancer immunotherapy for brain tumors: a collaborative workshop. *J Transl Med* **20**, 236 (2022).
10. Davidson, T.B.*, et al.* Expression of PD-1 by T Cells in Malignant Glioma Patients Reflects Exhaustion and Activation. *Clin Cancer Res* **25**, 1913-1922 (2019).
11. Lee, A.H.*, et al.* Neoadjuvant PD-1 blockade induces T cell and cDC1 activation but fails to overcome the immunosuppressive tumor associated macrophages in recurrent glioblastoma. *Nat Commun* **12**, 6938 (2021).
12. Ostrom, Q.T.*, et al.* CBTRUS Statistical Report: Primary Brain and Other Central Nervous System Tumors Diagnosed in the United States in 2009-2013. *Neuro Oncol* **18**, v1-v75 (2016).
13. Preusser, M.*, et al.* Current concepts and management of glioblastoma. *Ann Neurol* **70**, 9-21 (2011).
14. Stupp, R.*, et al.* Radiotherapy plus concomitant and adjuvant temozolomide for glioblastoma. *N Engl J Med* **352**, 987-996 (2005).
15. Miranda, A., Blanco-Prieto, M., Sousa, J., Pais, A. & Vitorino, C. Breaching barriers in glioblastoma. Part II: Targeted drug delivery and lipid nanoparticles. *Int J Pharm* (2017).
16. Liau, L.M.*, et al.* Dendritic cell vaccination in glioblastoma patients induces systemic and intracranial T-cell responses modulated by the local central nervous system tumor microenvironment. *Clin Cancer Res* **11**, 5515-5525 (2005).

17. Prins, R.M.*, et al.* Gene expression profile correlates with T-cell infiltration and relative survival in glioblastoma patients vaccinated with dendritic cell immunotherapy. *Clin Cancer Res* **17**, 1603-1615 (2011).

18. Prins, R.M.*, et al.* Comparison of glioma-associated antigen peptide-loaded versus autologous tumor lysate-loaded dendritic cell vaccination in malignant glioma patients. *J Immunother* **36**, 152-157 (2013).

19. Heimberger, A.B.*, et al.* Epidermal growth factor receptor VIII peptide vaccination is efficacious against established intracerebral tumors. *Clin Cancer Res* **9**, 4247-4254 (2003).

20. Kanaly, C.W., Ding, D., Heimberger, A.B. & Sampson, J.H. Clinical applications of a peptide-based vaccine for glioblastoma. *Neurosurg Clin N Am* **21**, 95-109 (2010).

21. Antonios, J.P.*, et al.* PD-1 blockade enhances the vaccination-induced immune response in glioma. *JCI Insight* **1**(2016).

22. Tumeh, P.C.*, et al.* PD-1 blockade induces responses by inhibiting adaptive immune resistance. *Nature* **515**, 568-571 (2014).

23. Antonios, J.P.*, et al.* Immunosuppressive tumor-infiltrating myeloid cells mediate adaptive immune resistance via a PD-1/PD-L1 mechanism in glioblastoma. *Neuro Oncol* **19**, 796-807 (2017).

24. Berghoff, A.S.*, et al.* Programmed death ligand 1 expression and tumor-infiltrating lymphocytes in glioblastoma. *Neuro-oncology* **17**, 1064-1075 (2015).

25. McDermott, D.F. & Atkins, M.B. PD-1 as a potential target in cancer therapy. *Cancer Med* **2**, 662-673 (2013).

26. Maxwell, R., Jackson, C.M. & Lim, M. Clinical Trials Investigating Immune Checkpoint Blockade in Glioblastoma. *Curr Treat Options Oncol* **18**, 51 (2017).

27. Topalian, S.L., Taube, J.M., Anders, R.A. & Pardoll, D.M. Mechanism-driven biomarkers to guide immune checkpoint blockade in cancer therapy. *Nature reviews. Cancer* **16**, 275-287 (2016).

28. Speiser, D.E*., et al.* T cell differentiation in chronic infection and cancer: functional adaptation or exhaustion? *Nature reviews. Immunology* **14**, 768-774 (2014).

29. Yuzefpolskiy Y, B.F., Penny L, Kalia V, Sarkar S. PD-1 signals instruct a cfritical metabolic switch for maintenance of T cell memory. *the Journal of Immunology* **198**(2017).

30. Charlton, J.J*., et al.* Programmed death-1 shapes memory phenotype CD8 T cell subsets in a cell-intrinsic manner. *J Immunol* **190**, 6104-6114 (2013).

31. Hong, J.J., Amancha, P.K., Rogers, K., Ansari, A.A. & Villinger, F. Re-evaluation of PD-1 expression by T cells as a marker for immune exhaustion during SIV infection. *PLoS One* **8**, e60186 (2013).

32. Bendall, S.C*., et al.* Single-cell mass cytometry of differential immune and drug responses across a human hematopoietic continuum. *Science* **332**, 687-696 (2011).

33. Leipold, M.D. & Maecker, H.T. Mass cytometry: protocol for daily tuning and running cell samples on a CyTOF mass cytometer. *J Vis Exp*, e4398 (2012).

34. Nowicka, M*., et al.* CyTOF workflow: differential discovery in high-throughput high-dimensional cytometry datasets. *F1000Res* **6**, 748 (2017).

35. Van Gassen, S*., et al.* FlowSOM: Using self-organizing maps for visualization and interpretation of cytometry data. *Cytometry A* **87**, 636-645 (2015).

36. Geiss, G.K.*, et al.* Direct multiplexed measurement of gene expression with color-coded probe pairs. *Nature biotechnology* **26**, 317-325 (2008).

37. Thommen, D.S.*, et al.* A transcriptionally and functionally distinct PD-1(+) CD8(+) T cell pool with predictive potential in non-small-cell lung cancer treated with PD-1 blockade. *Nat Med* **24**, 994-1004 (2018).

38. Woroniecka, K.*, et al.* T-Cell Exhaustion Signatures Vary with Tumor Type and Are Severe in Glioblastoma. *Clin Cancer Res* (2018).

39. Waki, K.*, et al.* PD-1 expression on peripheral blood T-cell subsets correlates with prognosis in non-small cell lung cancer. *Cancer Sci* **105**, 1229-1235 (2014).

40. Zheng, H.*, et al.* Expression of PD-1 on CD4+ T cells in peripheral blood associates with poor clinical outcome in non-small cell lung cancer. *Oncotarget* **7**, 56233-56240 (2016).

41. Rutkowski, J.*, et al.* Evaluation of peripheral blood T lymphocyte surface activation markers and transcription factors in patients with early stage non-small cell lung cancer. *Cell Immunol* (2017).

42. Wang, W.*, et al.* PD-1 mRNA expression in peripheral blood cells and its modulation characteristics in cancer patients. *Oncotarget* **8**, 50782-50791 (2017).

43. MacFarlane, A.W.t.*, et al.* PD-1 expression on peripheral blood cells increases with stage in renal cell carcinoma patients and is rapidly reduced after surgical tumor resection. *Cancer Immunol Res* **2**, 320-331 (2014).

44. Wei, B.*, et al.* The upregulation of programmed death 1 on peripheral blood T cells of glioma is correlated with disease progression. *Tumour Biol* **35**, 2923-2929 (2014).

45. Barber, D.L.*, et al.* Restoring function in exhausted CD8 T cells during chronic viral infection. *Nature* **439**, 682-687 (2006).

46. Day, C.L.*, et al.* PD-1 expression on HIV-specific T cells is associated with T-cell exhaustion and disease progression. *Nature* **443**, 350-354 (2006).

47. Crawford, A.*, et al.* Molecular and transcriptional basis of CD4(+) T cell dysfunction during chronic infection. *Immunity* **40**, 289-302 (2014).

48. Wherry, E.J.*, et al.* Molecular signature of CD8+ T cell exhaustion during chronic viral infection. *Immunity* **27**, 670-684 (2007).

49. Duraiswamy, J.*, et al.* Phenotype, function, and gene expression profiles of programmed death-1(hi) CD8 T cells in healthy human adults. *J Immunol* **186**, 4200-4212 (2011).

50. Gupta, P.K.*, et al.* CD39 Expression Identifies Terminally Exhausted CD8+ T Cells. *PLoS Pathog* **11**, e1005177 (2015).

51. Duhen, T.*, et al.* Co-expression of CD39 and CD103 identifies tumor-reactive CD8 T cells in human solid tumors. *Nat Commun* **9**, 2724 (2018).

52. Simoni, Y.*, et al.* Bystander CD8(+) T cells are abundant and phenotypically distinct in human tumour infiltrates. *Nature* **557**, 575-579 (2018).

53. Pollack, S.M.*, et al.* T-cell infiltration and clonality correlate with programmed cell death protein 1 and programmed death-ligand 1 expression in patients with soft tissue sarcomas. *Cancer* **123**, 3291-3304 (2017).

54. Nowicka, M.*, et al.* CyTOF workflow: differential discovery in high-throughput high-dimensional cytometry datasets. *F1000Res* **6**, 748 (2017).

55. Hsu, M.*, et al.* TCR Sequencing Can Identify and Track Glioma-Infiltrating T Cells after DC Vaccination. *Cancer Immunol Res* **4**, 412-418 (2016).

56. Lamborn, K.R.*, et al.* Progression-free survival: an important end point in evaluating therapy for recurrent high-grade gliomas. *Neuro Oncol* **10**, 162-170 (2008).

57. Wu, W.*, et al.* Joint NCCTG and NABTC prognostic factors analysis for high-grade recurrent glioma. *Neuro Oncol* **12**, 164-172 (2010).

58. Clarke, J.L.*, et al.* Is surgery at progression a prognostic marker for improved 6-month progression-free survival or overall survival for patients with recurrent glioblastoma? *Neuro Oncol* **13**, 1118-1124 (2011).

59. Cloughesy, T.F.*, et al.* Neoadjuvant anti-PD-1 immunotherapy promotes a survival benefit with intratumoral and systemic immune responses in recurrent glioblastoma. *Nat Med* **25**, 477-486 (2019).

60. Friebel, E.*, et al.* Single-Cell Mapping of Human Brain Cancer Reveals Tumor-Specific Instruction of Tissue-Invading Leukocytes. *Cell* **181**, 1626-1642 e1620 (2020).

61. Gubin, M.M.*, et al.* High-Dimensional Analysis Delineates Myeloid and Lymphoid Compartment Remodeling during Successful Immune-Checkpoint Cancer Therapy. *Cell* **175**, 1443 (2018).

62. Zhang, Q.*, et al.* Landscape and Dynamics of Single Immune Cells in Hepatocellular Carcinoma. *Cell* **179**, 829-845 e820 (2019).

63. Zheng, C.*, et al.* Landscape of Infiltrating T Cells in Liver Cancer Revealed by Single-Cell Sequencing. *Cell* **169**, 1342-1356 e1316 (2017).

64. Zilionis, R.*, et al.* Single-Cell Transcriptomics of Human and Mouse Lung Cancers Reveals Conserved Myeloid Populations across Individuals and Species. *Immunity* **50**, 1317-1334 e1310 (2019).

65. Steele, N.G., Carpenter, E.S., Kemp, S.B. et al. Multimodal mapping of the tumor and peripheral blood immune landscape in human pancreatic cancer. *Nat Cancer* **1**, 1097–1112 (2020).

66. Ding, A.S., Routkevitch, D., Jackson, C. & Lim, M. Targeting myeloid cells in combination treatments for glioma and other tumors. *Front Immunol* **10**, 1715 (2019).

67. Hussain, S.F.*, et al.* The role of human glioma-infiltrating microglia/macrophages in mediating antitumor immune responses. *Neuro Oncol* **8**, 261-279 (2006).

68. Prosniak, M.*, et al.* Glioma grade is associated with the accumulation and activity of cells bearing M2 monocyte markers. *Clin Cancer Res* **19**, 3776-3786 (2013).

69. Raychaudhuri, B.*, et al.* Myeloid derived suppressor cell infiltration of murine and human gliomas is associated with reduction of tumor infiltrating lymphocytes. *J Neurooncol* **122**, 293-301 (2015).

70. Fu, W.*, et al.* Single-Cell Atlas Reveals Complexity of the Immunosuppressive Microenvironment of Initial and Recurrent Glioblastoma. *Front Immunol* **11**, 835 (2020).

71. Muller, S.*, et al.* Single-cell profiling of human gliomas reveals macrophage ontogeny as a basis for regional differences in macrophage activation in the tumor microenvironment. *Genome Biol* **18**, 234 (2017).

72. Klemm, F.*, et al.* Interrogation of the Microenvironmental Landscape in Brain Tumors Reveals Disease-Specific Alterations of Immune Cells. *Cell* **181**, 1643-1660 e1617 (2020).

73. Strauss, L.*, et al.* Targeted deletion of PD-1 in myeloid cells induces antitumor immunity. *Sci Immunol* **5**(2020).

74. Rao, G.*, et al.* Anti-PD-1 Induces M1 Polarization in the Glioma Microenvironment and Exerts Therapeutic Efficacy in the Absence of CD8 Cytotoxic T Cells. *Clin Cancer Res* **26**, 4699-4712 (2020).

75. Goswami, S.*, et al.* Immune profiling of human tumors identifies CD73 as a combinatorial target in glioblastoma. *Nat Med* (2019).

76. Pombo Antunes, A.R.*, et al.* Single-cell profiling of myeloid cells in glioblastoma across species and disease stage reveals macrophage competition and specialization. *Nat Neurosci* **24**, 595-610 (2021).

77. Utzschneider, D.T.*, et al.* Early precursor T cells establish and propagate T cell exhaustion in chronic infection. *Nat Immunol* **21**, 1256-1266 (2020).

78. Beltra, J.C.*, et al.* Developmental Relationships of Four Exhausted CD8(+) T Cell Subsets Reveals Underlying Transcriptional and Epigenetic Landscape Control Mechanisms. *Immunity* **52**, 825-841 e828 (2020).

79. Chen, Z.*, et al.* TCF-1-Centered Transcriptional Network Drives an Effector versus Exhausted CD8 T Cell-Fate Decision. *Immunity* **51**, 840-855 e845 (2019).

80. Miller, B.C.*, et al.* Subsets of exhausted CD8(+) T cells differentially mediate tumor control and respond to checkpoint blockade. *Nat Immunol* **20**, 326-336 (2019).

81. Rodriguez, A. & Laio, A. Machine learning. Clustering by fast search and find of density peaks. *Science* **344**, 1492-1496 (2014).

82. Qiu, X*., et al.* Reversed graph embedding resolves complex single-cell trajectories. *Nat Methods* **14**, 979-982 (2017).

83. Mathewson, N.D*., et al.* Inhibitory CD161 receptor identified in glioma-infiltrating T cells by single-cell analysis. *Cell* **184**, 1281-1298 e1226 (2021).

84. Bottcher, J.P*., et al.* NK Cells Stimulate Recruitment of cDC1 into the Tumor Microenvironment Promoting Cancer Immune Control. *Cell* **172**, 1022-1037 e1014 (2018).

85. Brewitz, A*., et al.* CD8(+) T Cells Orchestrate pDC-XCR1(+) Dendritic Cell Spatial and Functional Cooperativity to Optimize Priming. *Immunity* **46**, 205-219 (2017).

86. Li, B*., et al.* Ultrasensitive detection of TCR hypervariable-region sequences in solid-tissue RNA-seq data. *Nat Genet* **49**, 482-483 (2017).

87. Zhang, L*., et al.* Lineage tracking reveals dynamic relationships of T cells in colorectal cancer. *Nature* **564**, 268-272 (2018).

88. Wu, T.D*., et al.* Peripheral T cell expansion predicts tumour infiltration and clinical response. *Nature* **579**, 274-278 (2020).

89. Chiou, S.H*., et al.* Global analysis of shared T cell specificities in human non-small cell lung cancer enables HLA inference and antigen discovery. *Immunity* **54**, 586-602 e588 (2021).

90. Geirsdottir, L*., et al.* Cross-Species Single-Cell Analysis Reveals Divergence of the Primate Microglia Program. *Cell* **179**, 1609-1622 e1616 (2019).

91. Yang, J.*, et al.* Loss of CXCR4 in Myeloid Cells Enhances Antitumor Immunity and Reduces Melanoma Growth through NK Cell and FASL Mechanisms. *Cancer Immunol Res* **6**, 1186-1198 (2018).

92. Kioi, M.*, et al.* Inhibition of vasculogenesis, but not angiogenesis, prevents the recurrence of glioblastoma after irradiation in mice. *J Clin Invest* **120**, 694-705 (2010).

93. Zhang, L.*, et al.* Single-Cell Analyses Inform Mechanisms of Myeloid-Targeted Therapies in Colon Cancer. *Cell* **181**, 442-459 e429 (2020).

94. Dissanayake, D.*, et al.* Nuclear factor-kappaB1 controls the functional maturation of dendritic cells and prevents the activation of autoreactive T cells. *Nat Med* **17**, 1663-1667 (2011).

95. Jin, S.*, et al.* Inference and analysis of cell-cell communication using CellChat. *Nat Commun* **12**, 1088 (2021).

96. Zhou, Y.H., Tan, F., Hess, K.R. & Yung, W.K. The expression of PAX6, PTEN, vascular endothelial growth factor, and epidermal growth factor receptor in gliomas: relationship to tumor grade and survival. *Clin Cancer Res* **9**, 3369-3375 (2003).

97. Garner, J.M.*, et al.* Molecular heterogeneity in a patient-derived glioblastoma xenoline is regulated by different cancer stem cell populations. *PLoS One* **10**, e0125838 (2015).

98. Contento, R.L.*, et al.* CXCR4-CCR5: a couple modulating T cell functions. *Proc Natl Acad Sci U S A* **105**, 10101-10106 (2008).

99. Gonzalez-Martin, A., Mira, E. & Manes, S. CCR5 in cancer immunotherapy: More than an "attractive" receptor for T cells. *Oncoimmunology* **1**, 106-108 (2012).

100. Alegre, M.L., Frauwirth, K.A. & Thompson, C.B. T-cell regulation by CD28 and CTLA-4. *Nat Rev Immunol* **1**, 220-228 (2001).

101. Pauken, K.E. & Wherry, E.J. TIGIT and CD226: tipping the balance between costimulatory and coinhibitory molecules to augment the cancer immunotherapy toolkit. *Cancer Cell* **26**, 785-787 (2014).

102. Gorvel, L. & Olive, D. Targeting the "PVR-TIGIT axis" with immune checkpoint therapies. *F1000Res* **9**(2020).

103. Lozano, E., Dominguez-Villar, M., Kuchroo, V. & Hafler, D.A. The TIGIT/CD226 axis regulates human T cell function. *J Immunol* **188**, 3869-3875 (2012).

104. Johnston, R.J.*, et al.* The immunoreceptor TIGIT regulates antitumor and antiviral CD8(+) T cell effector function. *Cancer Cell* **26**, 923-937 (2014).

105. Jin, H.S.*, et al.* CD226(hi)CD8(+) T Cells Are a Prerequisite for Anti-TIGIT Immunotherapy. *Cancer Immunol Res* **8**, 912-925 (2020).

106. Yost, K.E.*, et al.* Clonal replacement of tumor-specific T cells following PD-1 blockade. *Nat Med* **25**, 1251-1259 (2019).

107. Zhang, J.*, et al.* Compartmental Analysis of T-cell Clonal Dynamics as a Function of Pathologic Response to Neoadjuvant PD-1 Blockade in Resectable Non-Small Cell Lung Cancer. *Clin Cancer Res* **26**, 1327-1337 (2020).

108. Wei, S.C., Duffy, C.R. & Allison, J.P. Fundamental Mechanisms of Immune Checkpoint Blockade Therapy. *Cancer Discov* **8**, 1069-1086 (2018).

109. Long, G.V.*, et al.* Combination nivolumab and ipilimumab or nivolumab alone in melanoma brain metastases: a multicentre randomised phase 2 study. *Lancet Oncol* **19**, 672-681 (2018).

110. Butler, A., Hoffman, P., Smibert, P., Papalexi, E. & Satija, R. Integrating single-cell transcriptomic data across different conditions, technologies, and species. *Nat Biotechnol* **36**, 411-420 (2018).

111. Tirosh, I.*, et al.* Dissecting the multicellular ecosystem of metastatic melanoma by single-cell RNA-seq. *Science* **352**, 189-196 (2016).

112. van Linde, M.E.*, et al.* Treatment outcome of patients with recurrent glioblastoma multiforme: a retrospective multicenter analysis. *J Neurooncol* **135**, 183-192 (2017).

113. O'Rourke, D.M.*, et al.* A single dose of peripherally infused EGFRvIII-directed CAR T cells mediates antigen loss and induces adaptive resistance in patients with recurrent glioblastoma. *Sci Transl Med* **9**(2017).

114. Zhao, J.*, et al.* Immune and genomic correlates of response to anti-PD-1 immunotherapy in glioblastoma. *Nat Med* **25**, 462-469 (2019).

115. Arrieta, V.A.*, et al.* ERK1/2 phosphorylation predicts survival following anti-PD-1 immunotherapy in recurrent glioblastoma. *Nat Cancer* **2**, 1372-1386 (2021).

116. Scheper, W.*, et al.* Low and variable tumor reactivity of the intratumoral TCR repertoire in human cancers. *Nat Med* **25**, 89-94 (2019).

117. Hanada, K.I.*, et al.* A phenotypic signature that identifies neoantigen-reactive T cells in fresh human lung cancers. *Cancer Cell* **40**, 479-493 e476 (2022).

118. Lowery, F.J.*, et al.* Molecular signatures of antitumor neoantigen-reactive T cells from metastatic human cancers. *Science* **375**, 877-884 (2022).

119. Oliveira, G.*, et al.* Phenotype, specificity and avidity of antitumour CD8(+) T cells in melanoma. *Nature* **596**, 119-125 (2021).

120. Zheng, L.*, et al.* Pan-cancer single-cell landscape of tumor-infiltrating T cells. *Science* **374**, abe6474 (2021).

121. Rosskopf, S.*, et al.* A Jurkat 76 based triple parameter reporter system to evaluate TCR functions and adoptive T cell strategies. *Oncotarget* **9**, 17608-17619 (2018).

122. Hao, Y.*, et al.* Integrated analysis of multimodal single-cell data. *Cell* **184**, 3573-3587 e3529 (2021).

123. Becht, E.*, et al.* Dimensionality reduction for visualizing single-cell data using UMAP. *Nat Biotechnol* (2018).

124. Pasetto, A.*, et al.* Tumor- and Neoantigen-Reactive T-cell Receptors Can Be Identified Based on Their Frequency in Fresh Tumor. *Cancer Immunol Res* **4**, 734-743 (2016).

125. Li, H.*, et al.* Dysfunctional CD8 T Cells Form a Proliferative, Dynamically Regulated Compartment within Human Melanoma. *Cell* **176**, 775-789 e718 (2019).

126. Liu, B., Zhang, Y., Wang, D., Hu, X. & Zhang, Z. Single-cell meta-analyses reveal responses of tumor-reactive CXCL13(+) T cells to immune-checkpoint blockade. *Nat Cancer* **3**, 1123-1136 (2022).

127. Ye, Q.*, et al.* CD137 accurately identifies and enriches for naturally occurring tumor-reactive T cells in tumor. *Clin Cancer Res* **20**, 44-55 (2014).

128. Cao, J.*, et al.* The single-cell transcriptional landscape of mammalian organogenesis. *Nature* **566**, 496-502 (2019).

129. Siddiqui, I.*, et al.* Intratumoral Tcf1(+)PD-1(+)CD8(+) T Cells with Stem-like Properties Promote Tumor Control in Response to Vaccination and Checkpoint Blockade Immunotherapy. *Immunity* **50**, 195-211 e110 (2019).

130. Chow, A.*, et al.* The ectonucleotidase CD39 identifies tumor-reactive CD8(+) T cells predictive of immune checkpoint blockade efficacy in human lung cancer. *Immunity* **56**, 93-106 e106 (2023).

131. Caushi, J.X.*, et al.* Transcriptional programs of neoantigen-specific TIL in anti-PD-1-treated lung cancers. *Nature* **596**, 126-132 (2021).

132. Zheng, C.*, et al.* Transcriptomic profiles of neoantigen-reactive T cells in human gastrointestinal cancers. *Cancer Cell* **40**, 410-423 e417 (2022).

133. Choi, B.D.*, et al.* Systemic administration of a bispecific antibody targeting EGFRvIII successfully treats intracerebral glioma. *Proc Natl Acad Sci U S A* **110**, 270-275 (2013).

134. Leko, V.*, et al.* Identification of neoantigen-reactive T lymphocytes in the peripheral blood of a patient with glioblastoma. *J Immunother Cancer* **9**(2021).

135. Robinson, M.D., McCarthy, D.J. & Smyth, G.K. edgeR: a Bioconductor package for differential expression analysis of digital gene expression data. *Bioinformatics* **26**, 139-140 (2010).

136. McCarthy, D.J., Chen, Y. & Smyth, G.K. Differential expression analysis of multifactor RNA-Seq experiments with respect to biological variation. *Nucleic Acids Res* **40**, 4288-4297 (2012).

137. Chen, Y., Lun, A.T. & Smyth, G.K. From reads to genes to pathways: differential expression analysis of RNA-Seq experiments using Rsubread and the edgeR quasi-likelihood pipeline. *F1000Res* **5**, 1438 (2016).

138. Colli, L.M.*, et al.* Burden of Nonsynonymous Mutations among TCGA Cancers and Candidate Immune Checkpoint Inhibitor Responses. *Cancer Res* **76**, 3767-3772 (2016).

139. Schumacher, T.N. & Schreiber, R.D. Neoantigens in cancer immunotherapy. *Science* **348**, 69-74 (2015).

140. Wells, D.K.*, et al.* Key Parameters of Tumor Epitope Immunogenicity Revealed Through a Consortium Approach Improve Neoantigen Prediction. *Cell* **183**, 818-834 e813 (2020).

141. Rosenberg, S.A.*, et al.* Durable complete responses in heavily pretreated patients with metastatic melanoma using T-cell transfer immunotherapy. *Clin Cancer Res* **17**, 4550-4557 (2011).

142. Tran, E.*, et al.* T-Cell Transfer Therapy Targeting Mutant KRAS in Cancer. *N Engl J Med* **375**, 2255-2262 (2016).

143. Zacharakis, N.*, et al.* Immune recognition of somatic mutations leading to complete durable regression in metastatic breast cancer. *Nat Med* **24**, 724-730 (2018).

144. Kruse, C.A.*, et al.* Treatment of recurrent glioma with intracavitary alloreactive cytotoxic T lymphocytes and interleukin-2. *Cancer Immunol Immunother* **45**, 77-87 (1997).

145. Krishna, S.*, et al.* Stem-like CD8 T cells mediate response of adoptive cell immunotherapy against human cancer. *Science* **370**, 1328-1334 (2020).

146. Gosa, L., Ta, L. & Nathanson, D.A. Processing of Primary Patient Tumors and Subsequent Generation of Primary Cell Lines. *Methods Mol Biol* **1897**, 425-431 (2019).

147. Bolger, A.M., Lohse, M. & Usadel, B. Trimmomatic: a flexible trimmer for Illumina sequence data. *Bioinformatics* **30**, 2114-2120 (2014).

148. Altschul, S.F., Gish, W., Miller, W., Myers, E.W. & Lipman, D.J. Basic local alignment search tool. *J Mol Biol* **215**, 403-410 (1990).

149. Liau, L.M.*, et al.* Association of Autologous Tumor Lysate-Loaded Dendritic Cell Vaccination With Extension of Survival Among Patients With Newly Diagnosed and Recurrent Glioblastoma: A Phase 3 Prospective Externally Controlled Cohort Trial. *JAMA Oncol* **9**, 112-121 (2023).

150. Karimi, E.*, et al.* Single-cell spatial immune landscapes of primary and metastatic brain tumours. *Nature* **614**, 555-563 (2023).

151. Liu, S.*, et al.* Spatial maps of T cell receptors and transcriptomes reveal distinct immune niches and interactions in the adaptive immune response. *Immunity* **55**, 1940-1952 e1945 (2022).

152. Zaretsky, J.M.*, et al.* Mutations Associated with Acquired Resistance to PD-1 Blockade in Melanoma. *N Engl J Med* **375**, 819-829 (2016).